University of Catania

Doctor of Philosophy (PhD) in Natural Hazard Risk Mitigation and Ecological Transition of the Built Environment Cycle XXXVIII

Nicola De Fazio

Ultrasonic wave dispersion and attenuation as tools for mechanical characterization of construction materials

PhD Thesis

Supervisors: Prof. Luca Placidi
Assoc. Prof. Bilen Emek Abali

Academic Year 2024–2025

Acknowledgments

I would like to express my deepest gratitude to my supervisors, Prof. Luca Placidi and Prof. Bilen Emek Abali, for their guidance, scientific rigor, and constant support throughout this research. Their insight, encouragement, and critical perspective have profoundly shaped both this reasearch and my academic growth.

I am also sincerely grateful to Prof. Luca Placidi and Prof. Bilen Emek Abali for their valuable discussions, constructive feedback, and thoughtful suggestions, which significantly improved the quality of this thesis.

My appreciation extends to the colleagues and members of the Salvati Laboratory at the Polytechnic University of Bari, whose collaborative spirit and stimulating scientific environment made this journey both enriching and inspiring. I would also like to thank the technical staff and laboratory personnel for their assistance during the experimental activities.

Finally, I am deeply thankful to my family for their patience, understanding, and unconditional support throughout these years.

Dedications

To my beloved Mihaela and Rita,
whose unwavering support made this work possible.

To my parents,
for teaching me perseverance and dedication.

Abstract

This PhD thesis investigates ultrasonic wave dispersion and attenuation as quantitative tools for the mechanical characterization of construction materials. While ultrasonic techniques are widely used in practice, their interpretation is often based on simplified plane-wave assumptions and empirical correlations, which limit their reliability for direct parameter identification. In order to address this gap, analytical one-dimensional models incorporating microstructural effects, strain-gradient contributions, and viscous dissipation are developed. Closed-form expressions for phase velocity and attenuation are derived, providing a controlled theoretical benchmark. The analytical framework is then rigorously validated and extended through finite element formulations and two-dimensional simulations, enabling a systematic comparison between analytical predictions, numerical results, and laboratory ultrasonic measurements. The proposed approach establishes a consistent theoretical and computational framework that accounts for geometrical spreading, numerical dispersion control, and frequency-dependent attenuation. By integrating analytical modeling with numerically calibrated simulations, the thesis advances ultrasonic testing toward a physics-based methodology capable of supporting the direct identification of intrinsic mechanical parameters of construction materials. The results contribute to strengthening the scientific foundations required for the standardization of ultrasonic methods as primary tools for non-destructive material characterization.

Contents

1 Introduction

1.1 Ultrasonic wave tests: an historical background

The research on the physical and mechanical properties of construction materials and foundation soils is a crucial aspect in the advancement of engineering design[1]. The collection and interpretation of data pose continuous challenges and represent a critical factor for the accurate implementation of engineering projects[2]. Ultrasonic and seismic investigation methods are therefore regarded as valuable tools for the characterization of natural and construction materials.

From a historical standpoint, the theoretical foundations of wave propagation in elastic solids date back to the 19th century, with the development of classical elastodynamics following the works of Navier, Cauchy, and Lamé. A comprehensive modern treatment of elastic wave propagation in solids is provided in[3;4]. The systematic use of elastic waves for material characterization, however, became widespread only in the 20th century, particularly after the advent of seismic prospecting techniques in geophysics during the 1920s and 1930s. These methods were initially developed for subsurface exploration in the oil industry but were soon adapted to civil engineering applications.

In the 1950s and 1960s, ultrasonic testing techniques began to be extensively applied to concrete and construction materials, enabling the non-destructive evaluation of stiffness, homogeneity, and defect presence. The ultrasonic pulse velocity (UPV) method progressively became a standard tool for quality control and structural assessment. Over the past decades, increasing attention has been devoted to the interpretation of dynamic measurements in terms of mechanical parameters[5;6].

Velocity data allow for the determination of the longitudinal elastic modulus of a material through well-established formulas based on isotropic linear elastodynamics, which correlate Young's modulus with wave velocity and material density[4]. Initially perceived as a revolutionary tool for research and engineering-owing to its speed, cost-effectiveness, non-invasiveness, and applicability under difficult working conditions-geophysical methods for determining the longitudinal elastic modulus, especially seismic methods, soon faced the challenge of developing suitable interpretation models capable of accounting for the numerous factors that may influence wave velocity measurements[7–9]. The specialized scientific community working in the fields of ultrasonic and seismic testing has not remained indifferent to these challenges. On the contrary, extensive research efforts have been devoted over the past decades to refining theoretical models, improving signal processing techniques, and developing more reliable interpretation frameworks capable of incorporating effects such as material heterogeneity, boundary conditions, geometrical spreading, damping, and frequency dependence. A substantial body of literature reflects this sustained commitment to transforming dynamic wave measurements into robust and physically meaningful mechanical characterizations.

The present work is positioned within this broader research effort. Its objective is to contribute to the ongoing process of methodological consolidation and, ultimately, to the standardization of ultrasonic testing as a primary and autonomous technique for the determination of intrinsic material parameters.

1.2 State of the models

Ultrasonic wave propagation in solids is inherently linked to the constitutive response of the material, and its behavior often departs from the predictions of classical linear elasticity[10–12]. For this reason, the present literature review deliberately focuses on three tightly connected aspects that are central to ultrasonic-based material characterization: dispersion, attenuation, and geometric effects associated with realistic wave propagation.

It has been observed in the literature that, even for the same material, different values of

the longitudinal elastic modulus may be obtained depending on whether the measurements are performed in the laboratory or in situ. This discrepancy, frequently observed in construction materials and also reported in geophysical studies, is primarily due to the dispersive behavior of certain materials. In such cases, the interaction between the propagating wave and the material microstructure, as well as viscous effects, causes the wave velocity to depend on the propagation frequency[13].

Consequently, dispersion leads to different estimates of the longitudinal elastic modulus depending on the type of test performed (in situ or laboratory), reflecting variations in wave propagation velocities under different boundary conditions and frequency ranges. In the literature, the modulus evaluated from wave velocity measurements is often referred to as the "dynamic elastic modulus,"[14] in contrast to the "static elastic modulus" obtained from uniaxial mechanical tests.

It is now well established that viscous, heterogeneous, and microstructured materials exhibit frequency-dependent phase velocity, amplitude attenuation, and waveform distortion-phenomena that cannot be captured by purely elastic models. Such effects naturally emerge in viscoelastic solids and heterogeneous waveguides, where material dissipation, internal length scales, and fluid–solid interactions play a decisive role[15–19]. Similar behaviors have been reported in continua endowed with microstructure or higher-order kinematics, including strain-gradient[20–22] and porous media formulations[23–28]. These studies collectively highlight that dispersion and attenuation are intrinsic features of wave propagation in real materials, rather than secondary corrections.

From an experimental perspective, ultrasonic investigations on composite laminates, fiber-reinforced media, and damaged concrete have further demonstrated the strong sensitivity of measured wave velocities and amplitudes to microstructural features and damage evolution[29–31]. Beyond material effects, several contributions have shown that geometry and boundary conditions exert a first-order influence on ultrasonic measurements. In particular, studies[32;33] on guided and bulk waves interacting with notches, voids, and geometric discontinuities have revealed that scattering, mode conversion, and wavefront curvature significantly modify both phase and amplitude information, even in nominally homogeneous solids. Investigations on shear and Rayleigh–Lamb waves in plate-like structures clearly indicate that non-planar wave propagation and boundary-induced effects must be explicitly accounted for when interpreting experimental data[34;35]. From the experimental point of view, researchers at the Polytechnic University of Bari developed and validated in recent years several approaches for ultrasonic wave propagation. Two notable papers, which represent a reference for the present research, are worth mentioning. The first[29] introduced an innovative experimental approach based on ultrasonic immersion tests to characterize the elastic response of multi-layered anisotropic GFRP composites; it is observed that fluid immersion improves the acoustic coupling between the transducer and the sample, reducing signal loss and providing more accurate results. In the second paper[30] explored stress-induced damage in concrete using ultrasonic techniques, aiming to experimentally identify previous overloads in concrete structures. For the latter ultrasonic investigations, cyclic compression tests were conducted on concrete specimens with coarse-grained aggregates, and the sideband peak count (SPC) technique was employed to characterize stress-induced damage. It is highlighted that internal microcracking of the material due to applied loads and related damage involves changes in the wave as the internal microstructure of the material changes. Theoretical analyses based on reciprocity principles have further clarified that the scattered fields generated by geometric discontinuities influence the global propagation behavior, rather than remaining confined to local perturbations. These results reinforce the idea that boundary effects and geometric dispersion are not merely experimental artifacts, but fundamental features of ultrasonic wave propagation in finite domains[36]. Such findings provide a strong motivation for moving beyond idealized one-dimensional descriptions and adopting two-dimensional formulations in which circular wavefronts and boundary interactions naturally

arise.

On the modeling side, a wide range of enriched continuum theories has been developed to address dispersion and attenuation mechanisms in a physically grounded manner. Strain-gradient[37–41], micromorphic[42–44], Cosserat[45], surface elasticity[46], material porosity[27;47], nonlocal[48], and peridynamic models offer refined descriptions of wave reflection, transmission, and dispersion in materials with microstructure, voids[49] or evolving internal variables[44;50–60]. Architected and hierarchical systems, such as tensegrity lattices and graphene-based media, further illustrate how dispersion can be engineered or amplified through geometry and internal structure[47;61;62]. Complementary developments in nonlocal and nanobeam theories, as well as in high-grade elasticity, have extended these concepts by incorporating additional energetic and kinematic descriptors[63–66].

At a more fundamental scale, micromechanical and granular models[67;68] have shown that dispersion and attenuation can emerge directly from micro-inertia and particle-scale interactions when the wavelength becomes comparable to the characteristic microstructural length[42;69;70]. These approaches provide an important physical interpretation of frequency-dependent ultrasonic behavior, linking macroscopic observables to underlying material structure.

Ultrasonic dispersion has also been extensively explored as a diagnostic and characterization tool for construction materials, where heterogeneity, damage, and frequency content strongly influence wave propagation[71;72]. In this context, wavefield-based and guided-wave imaging techniques have been proposed to extract structural information from complex propagation patterns in plates and solid components, further emphasizing the need for modeling strategies capable of capturing both material and geometric effects[73]. Nonlinear and nonsmooth modeling frameworks, including hemivariational approaches, offer additional tools for describing dissipative and damage-related phenomena[74].

Despite these advances, mathematical models for one-dimensional rods and waveguides remain a cornerstone for understanding the fundamental dispersion and attenuation mechanisms in viscoelastic media[15;16;75;76]. These solutions provide essential benchmarks for numerical aproximations such as the finite elemente methods and play a key role in the calibration and validation of computations. Progress in experimental and computational techniques has further improved the modeling of dissipative processes in solids and fluids[77], while ultrasonic-based identification procedures have strengthened the link between measured waveforms and constitutive parameters[78]. The numerical treatment of higher-order continua has also matured through dedicated finite element developments for strain-gradient elasticity[12;39;61;68;79].

Given the stringent accuracy requirements of ultrasonic analyses, stable and accurate time-integration schemes are essential. High-order implicit Runge–Kutta methods, combined with finite element discretization, provide a robust computational framework for simulating wave propagation in viscoelastic[80;81] and gradient-enhanced materials[47;82–84].

Within this framework, the present work builds upon analytical dispersion models, enriched continuum theories, and recent insights into geometric scattering and boundary effects to develop a calibrated FEM-based methodology that bridges one-dimensional analytical solutions and two-dimensional realistic wave propagation. This approach enables a physically grounded interpretation of ultrasonic measurements and lays the foundation for the direct identification of material properties from ultrasonic data.

1.3 State of the normative

Ultrasonic testing of concrete is regulated through national and international standards aimed at defining reliable and repeatable procedures for the measurement of wave transit time and pulse velocity, rather than establishing universal constitutive correlations. Early normative documents adopted a more explicit link between ultrasonic measurements and elastic properties, whereas more recent standards have progressively restricted their scope to measurement protocols only.

A notable example is the former British Standard BS 1881-203:1986, which explicitly addressed not only the measurement of ultrasonic pulse velocity but also its interpretation in terms of material stiffness. In particular, BS 1881-203 introduced empirical relationships between pulse velocity and both the dynamic and static moduli of elasticity, summarized in Table 4 of the standard. Within this framework, the ultrasonic velocity was directly related to the dynamic elastic modulus through classical elastic-wave relations, under the implicit assumption of homogeneous, weakly dispersive behavior. While the standard clearly acknowledged the empirical nature and limited validity of such correlations, it nonetheless represented an early attempt to formalize the link between ultrasonic measurements and mechanical properties of concrete.

A similar philosophy can be found in the American standard ASTM C597, which governs the determination of longitudinal pulse velocity in concrete. ASTM C597 explicitly reports the analytical relationship between pulse velocity, density, dynamic elastic modulus, and Poisson's ratio, thereby recognizing the theoretical connection between wave propagation and elastic stiffness. At the same time, the standard clearly states that ultrasonic pulse velocity measurements are not intended as a direct or reliable means for determining strength or elastic modulus in field concrete, unless project-specific correlations are established through calibration against destructive tests. Frequency effects are only addressed indirectly, through practical recommendations on transducer selection, path length, and signal attenuation, without introducing dispersion models or frequency-dependent corrections.

With the introduction of the European standard EN 12504-4, the normative procedure shifted toward a measurement-oriented framework. EN 12504-4 defines the experimental procedures for ultrasonic testing, including transducer arrangements, coupling conditions, and time-of-flight determination, while explicitly avoiding the standardization of any correlation between ultrasonic velocity and mechanical properties. The ultrasonic pulse velocity is treated as a conventional parameter derived from the first detectable arrival of a broadband pulse, and no distinction is made between phase velocity, group velocity, or frequency-dependent wave behavior. Although informative annexes discuss factors influencing pulse velocity, such as geometry, moisture content, and reinforcement, the physical mechanisms of dispersion and attenuation are intentionally excluded from the normative scope.

The interpretation of non-destructive test results in terms of compressive strength is instead addressed by EN 13791:2018, which establishes procedures for in-situ strength assessment based on a combination of destructive and non-destructive data. Within this standard, ultrasonic pulse velocity and rebound hammer measurements are admitted only as auxiliary indicators. No analytical or tabulated relationships between UPV and compressive strength or elastic modulus are provided, and any empirical correlation must be calibrated locally for the specific structure under investigation.

Then, in addition to formal standards, the practical application of ultrasonic testing has historically been supported by technical guidelines and national recommendations derived from normative frameworks and large experimental databases. Such documents are not standards in a strict sense, but rather interpretative guides intended to assist practitioners in the evaluation of in-situ concrete properties under controlled and well-defined conditions. An example is provided by national technical reports developed in support of EN 12504-4 and EN 13791, in which experimental datasets are collected and organized to propose indicative relationships between ultrasonic pulse velocity and mechanical parameters, such as the dynamic elastic modulus, for specific classes of concrete and testing configurations.

These guides typically present tabulated or graphical correlations obtained for restricted ranges of material composition (e.g., aggregate type, water–cement ratio, curing conditions), specimen geometry, and excitation frequency, such as combinate SonReb method (see Figure 1.1). As such, the resulting tables can be regarded as *semi-universal*: they are valid only within the experimental domain for which they were calibrated and implicitly assume weakly dispersive behavior, limited attenuation, and a dominant longitudinal wave mode. Outside

these controlled conditions-such as in the presence of strong material heterogeneity, frequency-dependent dispersion, or viscous and gradient-enhanced dissipation-the applicability of these correlations becomes uncertain.

Tabelul 8.7 Rezistențele betonului de referință ($f_{c,ref}$) [N/mm^2]

V	N																		
[m/s]	16	18	20	22	24	26	28	30	32	34	36	38	40	42	44	46	48	50	52
3000	4	4.7	5.3	5.9	6.5	7.2	7.9	8.6	-	-	-	-	-	-	-	-	-	-	-
3100	4.5	5.2	5.8	6.5	7.2	7.8	8.5	9.3	10	-	-	-	-	-	-	-	-	-	-
3200	5	5.7	6.5	7.2	7.8	8.4	9.3	9.9	10.6	11.4	-	-	-	-	-	-	-	-	-
3300	5.6	6.3	7.1	7.7	8.4	9.2	9.8	10.6	11.5	12.5	13.6	-	-	-	-	-	-	-	-
3400	6.2	6.9	7.6	8.3	9.2	9.8	10.6	11.5	12.5	13.6	14.6	15.6	-	-	-	-	-	-	-
3450	6.5	7.3	8	8.7	9.5	10.2	11	12	13.1	14.1	15.1	16.1	17.3	-	-	-	-	-	-
3500	6.8	7.6	8.3	9.1	9.8	10.5	11.4	12.4	13.6	14.6	15.6	16.7	17.9	19.7	-	-	-	-	-
3550	7.1	7.9	8.7	9.3	10.2	10.9	11.9	12.9	14.1	15.1	16.1	17.3	18.7	20.7	22.7	-	-	-	-
3600	7.4	8.2	9	9.7	10.5	11.3	12.3	13.4	14.6	15.6	16.7	18	19.7	21.7	23.9	-	-	-	-
3650	-	8.5	9.3	10	10.9	11.7	12.8	13.9	15.1	16.2	17.4	18.8	20.7	22.7	25.1	-	-	-	-
3700	-	8.7	9.6	10.3	11.2	12.1	13.2	14.4	15.6	16.7	18.1	19.6	21.6	23.8	26.3	28.2	-	-	-
3750	-	9.1	9.9	10.7	11.6	12.6	13.8	15	16.2	17.5	18.9	20.6	22.6	24.9	27.1	29.4	32	-	-
3800	-	9.4	10.2	11	12	13.1	14.3	15.5	16.8	18.2	19.7	21.5	23.7	26.1	28	30.7	33.1	35.3	-
3850	-	9.8	10.5	11.4	12.5	13.6	14.9	16.1	17.5	18.9	20.6	22.6	24.8	27	29.2	31.7	34.1	36.3	-
3900	-	10.1	10.7	11.7	12.9	14.1	15.4	16.7	18.2	19.6	21.4	23.7	25.8	28	30.4	32.8	35	37.3	39.7
3950	-	10.3	11.1	12.1	13.4	14.7	15.9	17.1	18.9	20.5	22.4	24.7	26.8	29	31.4	33.8	36	38.3	40.7
4000	-	10.6	11.5	12.5	13.8	15.2	16.4	17.8	19.6	21.4	23.4	25.7	27.7	30.1	32.5	34.7	37	39.4	41.8
4050	-	-	11.9	13	14.4	15.7	17	18.6	20.6	22.4	24.5	26.7	28.8	31.1	33.4	35.7	38	40.4	42.8
4100	-	-	12.2	13.5	14.9	16.2	17.6	19.3	21.4	23.3	25.5	27.7	29.8	32.2	34.4	36.7	39.1	41.5	43.8
4150	-	-	-	14	15.4	16.7	18.2	20.1	22.4	24.3	26.5	28.8	30.8	33.2	35.4	37.7	40.1	42.5	44.8
4200	-	-	-	14.5	15.9	17.2	18.8	20.9	23.3	25.3	27.4	29.8	31.8	34.1	36.4	38.8	41.2	43.5	45.7
4250	-	-	-	-	16.4	17.9	19.6	21.8	24.3	26.3	28.4	30.8	32.8	35.1	37.4	39.8	42.1	44.5	46.7
4300	-	-	-	-	16.9	18.5	20.5	22.7	25.3	27.3	29.4	31.7	33.8	36	38.4	40.8	43.1	45.3	47.8
4350	-	-	-	-	-	-	21.5	23.6	26.3	28.3	30.6	32.6	34.7	36.9	39.3	41.7	44	46.3	48.8
4400	-	-	-	-	-	-	22.4	24.5	27.3	29.2	31.2	33.4	35.5	37.8	40.3	42.6	45	47.4	49.8
4450	-	-	-	-	-	-	-	-	28.2	30	32.1	34.3	36.4	38.6	41	43.5	46.1	48.5	-
4500	-	-	-	-	-	-	-	-	29	30.8	33	35.2	37.3	39.9	42.3	44.7	47.2	49.6	-
4550	-	-	-	-	-	-	-	-	-	31.8	33.9	36.2	38.4	40.9	43.4	45.8	48.2	50.7	-
4600	-	-	-	-	-	-	-	-	-	-	34.8	37.2	39.6	42	44.5	47	49.3	52	-
4650	-	-	-	-	-	-	-	-	-	-	35.8	38.2	40.6	43.1	45.6	48	50.5	53	-
4700	-	-	-	-	-	-	-	-	-	-	37	39.3	41.6	44	46.8	49	51.8	54.2	-
4750	-	-	-	-	-	-	-	-	-	-	-	-	42.5	45	47.7	50.1	52.8	55.4	-
4800	-	-	-	-	-	-	-	-	-	-	-	-	43.5	46	48.6	51.3	53.8	56.5	-
4850	-	-	-	-	-	-	-	-	-	-	-	-	-	47	49.7	52.2	54.9	57.5	-
4900	-	-	-	-	-	-	-	-	-	-	-	-	-	48	50.8	53.2	56	58.5	-
4950	-	-	-	-	-	-	-	-	-	-	-	-	-	-	51.8	54.3	56.9	59.6	-
5000	-	-	-	-	-	-	-	-	-	-	-	-	-	-	52.8	55.5	57.9	60.7	-

Figure 1.1: *Empirical correlation between ultrasonic pulse velocity (UPV), rebound index N, and reference compressive strength as reported in Table 8.7 of the Romanian national technical guideline derived from EN 12504-4 and EN 13791. The table provides discrete velocity phases, implicitly associated with standard ultrasonic testing conditions (low-frequency broadband excitation, weak dispersion, and conventional concrete compositions), and returns indicative mechanical properties (characteristic compressive strength of concrete) through empirical calibration with rebound index values by Schmidt hammer. Such correlations are valid only within the specific experimental domain for which they were derived and implicitly assume a frequency-independent ultrasonic velocity.*

While these semi-empirical tables have proven useful for engineering practice under standardized testing conditions, they do not constitute general constitutive laws, they are not regulated by a normative and they are not transferable across different frequencies, waveforms, or material classes without additional calibration. Consequently, their use does not eliminate the need for physically grounded models capable of explicitly accounting for frequency dependence, dispersion mechanisms, and waveform evolution. The present work addresses this gap by providing a numerical and analytical framework that operates beyond the assumptions underlying such semi-universal guidelines.

Overall, the evolution from BS 1881-203 and ASTM C597 to the current European standards reflects a progressive recognition of the complexity of ultrasonic wave propagation in concrete. Modern standards deliberately avoid encoding simplified constitutive interpretations, acknowledging that frequency-dependent dispersion, attenuation, and waveform distortion-especially in heterogeneous and dissipative materials-cannot be captured by universal empirical laws. These phenomena lie outside the assumptions underlying standardized UPV testing and require physically grounded analytical and numerical models, such as those developed in the present work.

1.4 Numerical strategy

Motivated by the limitations highlighted in the normative and state-of-the-art analysis, the present work develops a digital twin of the system and adopts a two-dimensional Finite Element Method (FEM) framework, in which wave propagation is described starting from the Lagrangian functional of the action $A(\mathbf{u})$:

$$A(\mathbf{u}) = \int_{t_0}^{t_1} \left\{ \int_\Omega (K - W)\, d\Omega + W^{\text{ext}} \right\} dt, \tag{1.1}$$

where K is the kinetic energy density, W is the internal energy density, and W^{ext} accounts for external actions. In this setting, the displacement field $\mathbf{u}(\mathbf{x}, t)$ is taken as the primary kinematic variable.

Dissipative effects are introduced by adopting the extended Rayleigh–Hamilton principle [71], in which the variation of the action is balanced by a dissipation functional. This can be written as

$$\delta A(\mathbf{u}) = \int_{t_0}^{t_1} \int_\Omega \left(\frac{\partial R}{\partial \dot{\mathbf{u}}} \cdot \delta \mathbf{u} + \frac{\partial R}{\partial \nabla \dot{\mathbf{u}}} : \nabla \delta \mathbf{u} \right) d\Omega\, dt, \tag{1.2}$$

where R is the Rayleigh dissipation functional, which introduces viscous contributions associated with both the velocity field and its spatial gradients, in order to capture the attenuation mechanisms observed in ultrasonic wave propagation.

The integration by part and simplification of the governing equations lead to a weak form, where inertia, elastic response, and attenuation mechanisms are consistently represented within a unified framework [72].

The two-dimensional setting is essential to capture the actual physics of wave propagation in finite domains, where non-planar wavefronts, geometric spreading, and boundary interactions play a primary role in shaping the observed ultrasonic response.

A one-dimensional analytical model [71;72] is used to calibrate the spatial and temporal discretization of the FEM. Once convergence is achieved, the same discretization is adopted in the two-dimensional FEM simulations.

While a fully three-dimensional framework would provide the most complete representation of ultrasonic wave propagation, its computational cost remains prohibitive for systematic analyses. The two-dimensional model therefore represents an effective compromise, capturing the essential features of realistic wave propagation while maintaining numerical efficiency, and providing a solid basis for future extensions toward three-dimensional configurations.

1.5 Target of this doctoral research

This doctoral research has been developed within the framework of the National PhD Program *Natural Hazard Risk Mitigation and Ecological Transition of the Built Environment*. The scientific objectives of the present work are fully aligned with the core mission of this program.

The innovation proposed in this research does not lie in the ultrasonic technique itself. As discussed in the previous subsections, ultrasonic and seismic-based methods have been widely used for decades in material characterization and non-destructive evaluation. Rather, the originality of this doctoral work resides in the interpretative and modeling framework adopted for the analysis of ultrasonic data.

Current standards and engineering practice generally treat ultrasonic testing as a complementary tool to destructive testing methods. Normative guidelines explicitly rely on empirical correlations calibrated through destructive tests, while ultrasonic measurements are mainly employed to densify datasets or support previously obtained mechanical characterizations. In this context, ultrasonic methods are not considered primary identification tools, but rather co-protagonists or, in some cases, simple supporting techniques.

This doctoral research suggests to a paradigm shift. The objective is to lay the scientific foundations for transforming ultrasonic techniques into primary and autonomous tools for material characterization. The true limitation preventing this transition is not the measurement technique itself, but the adequacy of the physical models and the reliability of the data interpretation procedures. The present work directly addresses this critical aspect by developing validated analytical models and calibrated finite element frameworks capable of linking measurable ultrasonic quantities-such as phase velocity and attenuation-to intrinsic mechanical parameters.

In doing so, this research fulfills the broader mission of the doctoral program. If material properties can be accurately determined through fully non-destructive ultrasonic methods, significant benefits follow in terms of ecological transition and risk mitigation. Ultrasonic techniques are essentially non-invasive, produce no structural damage, and generate negligible environmental impact. Their adoption as primary characterization tools would reduce the need for destructive testing, limit material waste, and preserve structural integrity.

Moreover, the accurate identification of mechanical parameters contributes directly to structural safety. A reliable determination of material properties allows for better assessment of structural performance, thereby reducing the risk of collapse and preventing unnecessary demolition or reconstruction. In addition, the economic advantages associated with non-destructive testing-such as reduced operational costs, shorter investigation times, and preservation of existing structures-translate into a more efficient use of resources.

For these reasons, the proposed research not only advances the scientific understanding of ultrasonic wave propagation in complex media, but also supports the ecological and risk-mitigation objectives that define the Doctor of Philosophy (PhD) in Natural Hazard Risk Mitigation and Ecological Transition of the Built Environment.

1.6 Structure of the thesis

The underlying thesis is organized into six sections (including the present introduction as Section 1) and develops a process aimed at transforming ultrasonic testing into a fully quantitative tool for material parameter identification. The structure reflects the conceptual evolution of the work: from fundamental theoretical modeling, to rigorous numerical validation, to multidimensional wave propagation analysis, and finally to the formulation of an inverse identification strategy.

Section 2 introduces the physical and methodological context of the study. The fundamental principles of ultrasonic wave propagation in elastic, second-gradient, and viscoelastic media are recalled, with particular attention to real dispersive effects. This section provides mathematical

models, hereafter referred to analytical models, since they admit a closed-form solution for plane-wave propagation, useful for material characterization through UPV techniques and motivates the need for a higher-dimensional and numerically controlled framework capable of bridging the gap between simplified theory and practical ultrasonic inspection.

Section 3 further develops the analytical models introduced in the previous section and investigates in greater detail the simultaneous presence of second-gradient parameters and viscosity. In addition to dispersion, attenuation phenomena are systematically analyzed, thereby completing the analytical framework proposed in Section 2 and providing additional validation strategies. The theoretical approach adopted for the construction of the analytical model in both Sections 2 and 3 is consistent: starting from the balance laws and constitutive assumptions, the governing equations of motion are derived for a viscoelastic continuum including viscous contributions. The complex wavenumber is obtained in closed form, allowing the explicit derivation of phase velocity and attenuation as functions of frequency.

Sections 2 and 3 establish the theoretical reference solution that serves as the benchmark for all subsequent numerical analyses. The analytical model provides a controlled environment in which dispersion and attenuation can be clearly separated from numerical artefacts.

Section 4 is devoted to the construction, implementation, and rigorous validation of the one-dimensional Finite Element Method (FEM) based model. The discrete formulation is introduced, and the influence of spatial and temporal discretization on numerical dispersion and numerical dissipation is systematically investigated. A comprehensive space-time convergence study is performed over a broad range of frequencies, highlighting the increasing sensitivity of attenuation to discretization refinement. In order to obtain an objective and frequency-dependent accuracy criterion, the relative errors on phase velocity and amplitude are combined into a root-mean-square error indicator. The resulting Root Mean Square Error (RMSE) surfaces in the space reveal a non-trivial coupling between spatial and temporal resolution. Hyperbolic convergence laws are identified, defining the boundary between admissible and non-admissible discretizations. This section establishes the numerical robustness of the FEM framework and provides a rigorous foundation for its extension to higher dimensions. In addition, peak-detection strategies at the sensor location are analyzed, the influence of sensor position is investigated, and the weak form for the FEM through the variational formulation have been formally established.

Section 5 extends the formulation to two-dimensional domains in order to incorporate geometrical spreading effects associated with localized ultrasonic excitation. The transition from scalar to vector kinematics is developed, and the weak form is generalized to account for transverse deformation and Poisson coupling. Two excitation configurations are investigated: plane waves and circular waves. The influence of specimen geometry and wavelength-to-thickness ratio on wavefront evolution is analyzed in detail. Particular attention is devoted to the transition occurring when the wavelength becomes comparable to the specimen height, a regime in which multiple propagation paths and boundary reflections alter the apparent phase and amplitude response. The previously established RMSE-based convergence methodology is extended to the two-dimensional case, ensuring that all simulations are performed within a rigorously controlled accuracy domain. This section demonstrates that geometrical effects introduce additional attenuation and subtle phase shifts that cannot be captured by one-dimensional plane-wave models.

Furthermore, phase velocity and attenuation extracted from two-dimensional simulations are systematically compiled as reference tables correlating measurable ultrasonic quantities with intrinsic material parameters, including Young's modulus and viscous coefficients. A bilinear interpolation strategy combined with a least-squares minimization procedure is formulated to enable inverse parameter identification from experimental data. The methodology is validated for different material systems, demonstrating that the framework is not restricted to a single reference material but can be generalized. This section represents the practical culmination of the thesis, translating the analytical and numerical developments into an operational identification tool. The numerical simulations are primarily developed for a metallic material; however,

at the end of this section the entire procedure is repeated for a concrete specimen in order to demonstrate the adaptability and generality of the proposed approach.

Finally, Section 6 summarizes the principal findings of the work and discusses their broader implications. The results confirm that geometrical spreading, numerical dispersion control, and frequency-dependent attenuation must be simultaneously accounted for in order to achieve reliable quantitative identification. Future research directions are outlined, including the extension to higher-gradient continuum theories, micro-inertial effects, and heterogeneous microstructured materials. The long-term objective is to provide a rigorous scientific basis for the evolution of ultrasonic testing from an empirical correlation-based method to a predictive, physics-driven material characterization framework.

For clarity, Table 1.2 summarizes all symbols and notations adopted throughout the analytical formulations, numerical models, convergence analyses, and post-processing procedures.

Symbol	Description	Unit SI system
	Variational Formulation	
$A(u)$	Action functional	[J·s]
K	Kinetic energy density (1D)	[J/m]
W^{int}	Internal potential energy density (1D)	[J/m]
W^{ext}	External potential energy density (1D)	[J/m]
R	Rayleigh dissipation function	[J/s]
δ	First variation operator	[-]
	Geometry and Time	
x, y	Spatial coordinates	[m]
t	Time	[s]
t_{pulse}	Excitation pulse duration	[s]
t_0, t_1	Initial and final time instants	[s]
L	Length of the 1D model	[m]
H	Height of the 2D specimen	[m]
x_s	Sensor position	[m]
Ω	Computational domain	[m^2]
$\partial\Omega$	Boundary of the domain	[-]
	Kinematics	
$u(x,t)$	Displacement field (1D)	[m]
$\mathbf{u} = (u_x, u_y)$	Vector displacement field (2D)	[m]
u_0 or A_0	Complex initial wave amplitude	[m]
$A(x)$	Wave amplitude at position x	[m]
u_{peak}	Peak displacement amplitude	[m]
u'	First space derivative of displacement	[-]
u''	Second space derivative of displacement	[1/m]
$\dot{u}$	First time derivative of displacement	[m/s]
$\ddot{u}$	Second time derivative of displacement	[m/s^2]
δu	Virtual displacement (test function)	[m]

Symbol	Description	Unit
$\mathbf{v}$	Vector-valued test function (2D)	[m]
$u_i(t)$	Nodal displacement degrees of freedom	[m]
$N_i(x)$	Finite element shape functions	[-]
$\boldsymbol{\varepsilon}$	Strain tensor	[-]
$\nabla \mathbf{u}$	Displacement gradient	[-]
Material Parameters		
k_1	Standard elastic modulus (1D formulation)	[J/m]
k_2	Strain-gradient elastic modulus (or microstructure parameter)	[N·m^2]
E	Young's modulus	[Pa]
ν	Poisson's ratio	[-]
ρ	Lineic mass density (1D)	[kg/m]
η	Micro-inertia parameter	[kg·m]
c	Damping viscosity parameter	[kg/(m·s)]
c_1	Kelvin-Voigt viscosity parameter (first-gradient field)	[(N·s)/m]
c_2	Internal viscosity (second-gradient field)	[N·m^2·s]
ζ	Damping ratio	[-]
Q	Quality factor	[-]
L_E	Material characteristic length	[m]
External Actions		
F_y^{ext}	Concentrated force applied at $x = y$, with $y \in \{0, L\}$	[N]
B_y^{ext}	Concentrated double force at $x = y$ with $y \in \{0, L\}$	[N·m]
b_n	Distributed force density	[N/m]
b_d	Distributed double-force density	[N]
Wave Propagation Quantities		
f	Excitation frequency (kHz notation)	[kHz]
ν	Excitation frequency (Hz notation)	[Hz]
ω	Angular frequency ($2\pi f$)	[rad/s]
ω_s	Characteristic frequency for wave solution	[rad/s]
ω_c	Characteristic frequency of damped elastic solid	[rad/s]
ω_{c_1}	Characteristic frequency for Kelvin-Voigt material	[rad/s]
k_w or k	Complex wave number	[1/m]
λ	Wavelength	[m]
v_p	Phase velocity	[m/s]
$v_p^{elastic}$	Phase velocity elastic regime	[m/s]

Symbol	Description	Unit
v_l	Low-frequency phase velocity (or elastic regime)	[m/s]
v_h	High-frequency phase velocity	[m/s]
α	Attenuation coefficient	[1/m]
Ω_2	Wave motion phase	[rad]
a	Real part of squared wavenumber	[1/m^2]
b	Imaginary part of squared wavenumber	[1/m^2]
Mathematical Operators		
i	Imaginary unit	[-]
∇ or grad	Gradient operator	[-]
$\nabla\cdot$ or div	Divergence operator	[-]
Δ	Laplace operator	[-]
:	Double tensor contraction	[-]
T	Transpose operator	[-]
$\Re(\cdot)$	Real part operator	[-]
$\Im(\cdot)$	Imaginary part operator	[-]
cos	Cosine function	[-]
sin	Sine function	[-]
arctan	Inverse tangent function	[-]
π	Archimedes' constant	[-]
$\mathbb{R}$	Set of real numbers	[-]
$\mathbb{N}$	Set of natural numbers	[-]
Spatial and temporal Discretization		
N_{el}	Number of spatial finite elements (1D)	[-]
N_{ti}	Number of temporal subdivisions	[-]
m_x, m_y	Number of elements along x and y	[-]
Δx, Δy	Spatial mesh sizes	[m]
Δt	Time step size	[s]
Error and Identification		
ε_{v_p}	Relative phase-velocity error	[%]
ε_A	Relative amplitude error	[%]
RMSE	Root-mean-square error	[%]
$\text{RMSE}_{\text{global}}$	Global RMSE indicator	[%]
TOF	Time of flight	[s]
v_p^{meas}	Measured phase velocity	[m/s]
α^{meas}	Measured attenuation	[1/m]

Table 1.2: *List of symbols used throughout the thesis, grouped according to their physical and mathematical role in the analytical formulation, finite element implementation, and inverse identification framework.*

2 Analytical models for ultrasonic wave dispersion in construction materials

In this section we consider three different models capable of predicting dispersive behavior, i.e., the dependence of the phase velocity on frequency, for longitudinal wave propagation in a one-dimensional continuum, representative of a bar or rod.
In detail, each constitutive models represent different physical mechanisms governing wave propagation and generating different dispersive phenomena.The strain-gradient elastic model accounts for dispersive effects associated with microstructural length scales, without including dissipation. The viscous damping model introduces dissipation through a velocity-proportional term, representing a distributed viscous resistance. The Kelvin–Voigt model incorporates internal structural viscosity, associated with spatial gradients of the velocity field.
These models are not intended to be used simultaneously, but rather to provide complementary insights into the different mechanisms influencing wave propagation. For clarity, the main assumptions and physical implications of the considered models are summarized in Table 2.1.

Model	Dispersion	Dissipation	Main mechanism
Strain-gradient elastic	✓	×	Microstructural effects
Viscous damping	✓	✓	Velocity damping
Kelvin–Voigt	✓	✓	Internal viscosity

Table 2.1: *Summary of the constitutive models introduced in Chapter 2 and their main physical implications in terms of dispersion and dissipation.*

2.1 1D elastic strain gradient model

In this section we consider a conservative non-dissipative model, capable of predicting dispersive behavior, i.e., the dependence of the phase velocity to the frequency.

2.1.1 Variational formulation

According to the Principle of Least Action[85], once the displacement $u(x,t)$ is prescribed at two instants of time t_0 and t_1 (i.e., $u(x,t=t_0)=u_0(x)$ and $u(x,t=t_1)=u_1(x)$), the action functional A is associated to the motion of a body (i.e., to the displacement $u(x,t)$ for each point placed in the reference configuration at x and for each instant of time t). The action is asserted to be the minimum, over all the admissible displacement, once it is evaluated at the solution $u(x,t)$; as it is well-known, it is worth to note that this principle states that natural phenomena occur always in the most efficient way, i.e. with the minimal possible effort[85;86]. Thus, by calling K the kinetic energy density, W the potential energy density, and W^{ext} the external energy function, and by considering a one-dimensional body of length L, we assume the following relation

$$A(u)=\int_{t_0}^{t_1}\left\{\int_0^L (K-W)\,dx + W^{\text{ext}}\right\}dt, \tag{2.1}$$

where the action A is a functional of the displacement field $u(x,t)$. The explicit forms of the last three energy functions for the linear elastic and strain gradient case are as follows

$$K=\int_0^L \left(\frac{1}{2}\rho\dot{u}^2+\frac{1}{2}\eta\dot{u'}^2\right)dx, \tag{2.2}$$

$$W^{\text{int}}=\int_0^L \left(\frac{1}{2}k_1u'^2+\frac{1}{2}k_2u''^2\right)dx, \tag{2.3}$$

$$W^{\text{ext}} = \left[F_0^{\text{ext}} u + B_0^{\text{ext}} u'\right]_{x=0} + \left[F_L^{\text{ext}} u + B_L^{\text{ext}} u'\right]_{x=L} + \int_0^L (b_n u + b_d u')\, dx, \tag{2.4}$$

where: k_1 and k_2 are the standard elastic modulus for a linear one-dimensional elastic body and the non-standard strain-gradient modulus, respectively; given the displacement u, its derivatives with respect to time are denoted by $\dot{u}$ and with respect to space u' (first derivative) or u'' (second derivative), ρ and η are the mass density (mass per unit length) and the micro-inertia of the mono-dimensional body, respectively; b_n and b_d are the external distributed (per unit length) forces and double forces, respectively; F_0^{ext} (or F_L^{ext}) and B_0^{ext} (or B_L^{ext}) are the concentrated forces and double forces, evaluated at the extrema at $x = 0$ (or at $x = L$) of the one-dimensional body, respectively.
In order to find the minimum of the Action, we calculate its variation δA and we set it equal to zero, for any admissible variation δu of the displacement field u

$$\delta A = \int_{t_0}^{t_1} \left\{ \int_0^L (\delta K - \delta W^{\text{int}})\, dx + \delta W^{\text{ext}} \right\} dt = 0, \quad \forall \delta u \in V, \tag{2.5}$$

where V is the set of the admissible variations, defined with the set of kinematic restrictions induced by the external constraints.
Replacing equations (2.2), (2.3) and (2.4) in equation (2.5) and calculating the variation of the Action, it results

$$\begin{aligned} \delta A = \int_{t_0}^{t_1} \Bigg\{ \int_0^L & \left[\rho \dot{u} \delta \dot{u} + \eta \dot{u}' \delta \dot{u}' - k_1 u' \delta u' - k_2 u'' \delta u'' + (b_n \delta u + b_d \delta u') \right] dx \\ & + \left[F^{\text{ext}} \delta u + B^{\text{ext}} \delta u'\right]_{x=0} + \left[F^{\text{ext}} \delta u + B^{\text{ext}} \delta u'\right]_{x=L} \Bigg\}\, dt = 0. \end{aligned} \tag{2.6}$$

Integrating by parts, in space and in time, leads the equation (2.6) to the following

$$\begin{aligned} \delta A = \int_{t_0}^{t_1} \Bigg\{ \int_0^L & \left[\delta u \left(-\rho \ddot{u} + k_1 u'' + \eta \ddot{u}' - k_2 u^{(4)} + b_n - b_d' \right) \right] dx \\ & - \delta u(x=0) \left[-\eta \dot{u}'(x=0) - k_1 u'(x=0) + k_2 u'''(x=0) + b_d - F^{\text{ext}}(x=0) \right] \\ & + \delta u(x=L) \left[-\eta \dot{u}'(x=L) - k_1 u'(x=L) + k_2 u'''(x=L) + b_d + F^{\text{ext}}(x=L) \right] \\ & - \delta u'(x=0) \left[-k_2 u''(x=0) - B^{\text{ext}}(x=0) \right] \\ & + \delta u'(x=L) \left[-k_2 u''(x=L) + B^{\text{ext}}(x=L) \right] \Bigg\}\, dt = 0. \end{aligned} \tag{2.7}$$

where, since the displacement $u(x,t)$ is assumed to be prescribed both at $t = t_0$ and at $t = t_1$, we have that $\delta u(x, t = t_0) = \delta u(x, t = t_1) = 0$. As for the Principle of Least Action, equation (2.7) must hold for every admissible variation δu of the displacement field u. The last four lines of equation (2.7) must be null, because the displacement u and the displacement gradient u' are prescribed at the boundary (i.e., the left-hand sides of the following equations are satisfied), then its variation is null as well as the corresponding line of equation (2.7). In order to make null the same lines of equation (2.7), if the mentioned kinematic conditions are not prescribed, then the right-hand sides of the following equations are satisfied

$$u(0,t) = u_0(t) \qquad \text{or} \quad -\eta \dot{u}'(x=0,t) - k_1 u'(x=0,t) + k_2 u'''(x=0,t) + b_d = F_0^{\text{ext}}, \tag{2.8}$$

$$u(L,t) = u_L(t) \qquad \text{or} \quad -\eta \dot{u}'(x=L,t) - k_1 u'(x=L,t) + k_2 u'''(x=L,t) + b_d = -F_L^{\text{ext}}, \tag{2.9}$$

$$u'(0,t) = b_0(t) \qquad \text{or} \qquad -k_2 u''(x=0,t) \;\; = B_0^{\text{ext}}(t), \tag{2.10}$$

$$u'(L,t) = b_L(t) \qquad \text{or} \qquad -k_2 u''(x=L,t) \;\; = -B_L^{\text{ext}}(t). \tag{2.11}$$

for every instant of time, i.e., $\forall t \in \mathbb{R}$. Finally, also the first line of equation (2.7) must be zero for every admissibile variation δu of the displacement field. Thus, because of its arbitrariness, it results

$$-\rho\ddot{u} + k_1 u'' + \eta\ddot{u}' - k_2 u^{(4)} - b_d' + b_n = 0, \quad \forall x \in [0,L], \quad \forall t \in \mathbb{R}. \tag{2.12}$$

Equation (2.12) is the Partial Differential Equation (PDE) governing the evolution of the displacement field $u(x,t)$ for the investigated model, that will be solved in the following two subsections. In particular, in the subsection b, we search for equation (2.12) a closed form solution and we assume the body length L to be sufficiently large so that the boundary conditions (BCs) (2.8)-(2.11) do not influence the solution.

2.1.2 Wave form solution

Equation (2.12) can be solved considering no external distributed actions ($b_n = 0$ and $b_d = 0$) in the form of the following plane wave solution for the displacement field

$$u(x,t) = \text{Re}\left(u_0 e^{i(\omega t - k_w x)}\right), \tag{2.13}$$

where u_0 is the complex wave amplitude, ω is the frequency of the wave expressed in Rad/sec, k_w is the wave number, i is the imaginary unit and Re is the real part operator. Calculating the derivatives of equation (2.13) and replacing them into equation (2.12), it results

$$-k_1 k_w^2 - k_2 k_w^4 = -\rho\omega^2 - \eta\omega^2 k_w^2, \tag{2.14}$$

where the arbitrariness of the complex wave amplitude u_0 has been considered. Equation (2.14) is a 4th grade algebraic equation in terms of k_w, admitting therefore four complex solutions for k_w. Two solutions are imaginary and correspond to non-propagating standing waves. Two solutions are real ($k_w = \pm\hat{k}_w$) and correspond to two propagating waves, with

$$\hat{k}_w = \sqrt{\frac{-k_1 + \eta\omega^2 + \sqrt{4k_2\rho\omega^2 + (k_1 - \eta\omega^2)^2}}{\sqrt{2}k_2}}. \tag{2.15}$$

Among these last two solutions, one is negative ($k_\omega = -\hat{k}_w$) and corresponds to a propagative wave towards the left-hand direction, and one is positive ($k_\omega = +\hat{k}_w$) corresponding to a propagative wave towards the right-hand direction. Remembering the correlation between frequency ω, wave number k_w and phase velocity v_p[4], we obtain from equation (2.15)

$$v_p = \text{Re}\left(\frac{\omega}{k_w}\right) = \text{Re}\left(\frac{\omega}{\hat{k}_w}\right) = \frac{\sqrt{2}\omega\sqrt{k_2}}{\sqrt{-k_1 + \eta\omega^2 + \sqrt{4k_2\rho\omega^2 + (k_1 - \eta\omega^2)^2}}}, \tag{2.16}$$

which reduces, when $\omega \to 0$ (low frequency regime), to

$$\lim_{\omega\to 0} v_p = v_l = \sqrt{\frac{k_1}{\rho}}. \tag{2.17}$$

Another important reduction of the phase velocity expression (2.16) is under the restriction of no the second gradient parameters k_2 and η. Then, first from equation (2.16) we calculate the square phase velocity,

$$v_p^2 = \frac{2\omega^2 k_2}{-k_1 + \eta\omega^2 + \sqrt{4k_2\rho\omega^2 + (k_1 - \eta\omega^2)^2}}. \tag{2.18}$$

A direct limit of equation (2.18) for k_2 and η tends to zero, yields an indeterminate form, so, thus, we first perform the limit for $\eta \to 0$,

$$\lim_{\eta\to 0} v_p^2 = \frac{2\omega^2 k_2}{-k_1 + \sqrt{4k_2\rho\omega^2 + k_1^2}}. \tag{2.19}$$

In order to evaluate the limit for $k_2 \to 0$, we rationalize the denominator of Eq. (2.19):

$$\begin{aligned}
\lim_{k_2\to 0} v_p^2 &= \lim_{k_2\to 0} \frac{2\omega^2 k_2}{-k_1 + \sqrt{4k_2\rho\omega^2 + k_1^2}} \cdot \frac{k_1 + \sqrt{4k_2\rho\omega^2 + k_1^2}}{k_1 + \sqrt{4k_2\rho\omega^2 + k_1^2}} \\
&= \lim_{k_2\to 0} \frac{2\omega^2 k_2 \left(k_1 + \sqrt{4k_2\rho\omega^2 + k_1^2}\right)}{4k_2\rho\omega^2} \\
&= \lim_{k_2\to 0} \frac{k_1 + \sqrt{4k_2\rho\omega^2 + k_1^2}}{2\rho} \\
&= \frac{k_1}{\rho} = v_l^2
\end{aligned} \tag{2.20}$$

Thus, the low-frequency limit in equation (2.17) and that without second-gradient parameters in equation (2.20) yield the same phase velocity. Thus, the low frequency limit in equation (2.17) and that without second gradient parameters in equation (2.20) yeld the same phase velocity.

Equation (2.17) shows that the second gradient parameters k_2 and η have no influence on the phase velocity v_l at the low frequency regime; indeed, equation (2.17) is the velocity value evaluated by using the classic linear elastodynamic theory. From the mechanical point of view, the reason for the latter result is that the wavelength $\lambda = \frac{2\pi}{k_w}$ is, in this regime, larger than the microstructural length of the medium. This intrinsic length emerges naturally from the balance between the classical elastic term $k_1 u''$ and the strain-gradient contribution $k_2 u^{(4)}$ appearing in equation (2.12). Introducing a characteristic spatial scale L, these terms scale respectively as k_1/L^2 and k_2/L^4; equating their orders yields $L^2 \sim k_2/k_1$, which defines the elastic characteristic length L_E,

$$L_E = \sqrt{\frac{k_2}{k_1}}. \tag{2.21}$$

Besides, in the high frequency limit, from equation (2.16) we have that the phase velocity

$$\lim_{\omega\to\infty} v_p = v_h = \sqrt{\frac{k_2}{\eta}}, \tag{2.22}$$

depends only upon the strain gradient parameters k_2 and η. Indeed, now the wavelength λ and the elastic characteristic length L_E have comparable dimensions. The phase velocity expression (2.16) can be also written in the following form

$$v_p = \frac{\sqrt{2}v_l}{\sqrt{\left(\frac{v_l}{v_h}\right)^2 - \left(\frac{v_l}{\omega L_E}\right)^2 + \sqrt{4\left(\frac{v_l}{\omega L_E}\right)^2 + \left(\left(\frac{v_l}{\omega L_E}\right)^2 - \left(\frac{v_l}{v_h}\right)^2\right)^2}}}. \tag{2.23}$$

i.e., as a function of the characteristic length L_E, or

$$v_p = \frac{\sqrt{2}\, v_l}{\sqrt{\left(\frac{v_l}{v_h}\right)^2 - \left(\frac{\omega_s}{\omega}\right)^2 + \sqrt{4\left(\frac{\omega_s}{\omega}\right)^2 + \left[\left(\frac{\omega_s}{\omega}\right)^2 - \left(\frac{v_l}{v_h}\right)^2\right]^2}}}, \tag{2.24}$$

i.e., as a function of the characteristic frequency ω_s

$$\omega_s = \frac{v_l}{L_E} = \frac{k_1}{\sqrt{\rho k_2}}, \tag{2.25}$$

where the denominator in equation (2.24) is a dimensionless number, function of two dimensionless quantities, i.e., the ratio v_l/v_h between the velocities in the low and high-frequency regimes, and the ratio ω_s/ω between the characteristic frequency defined in equation (2.25) and the actual frequency.

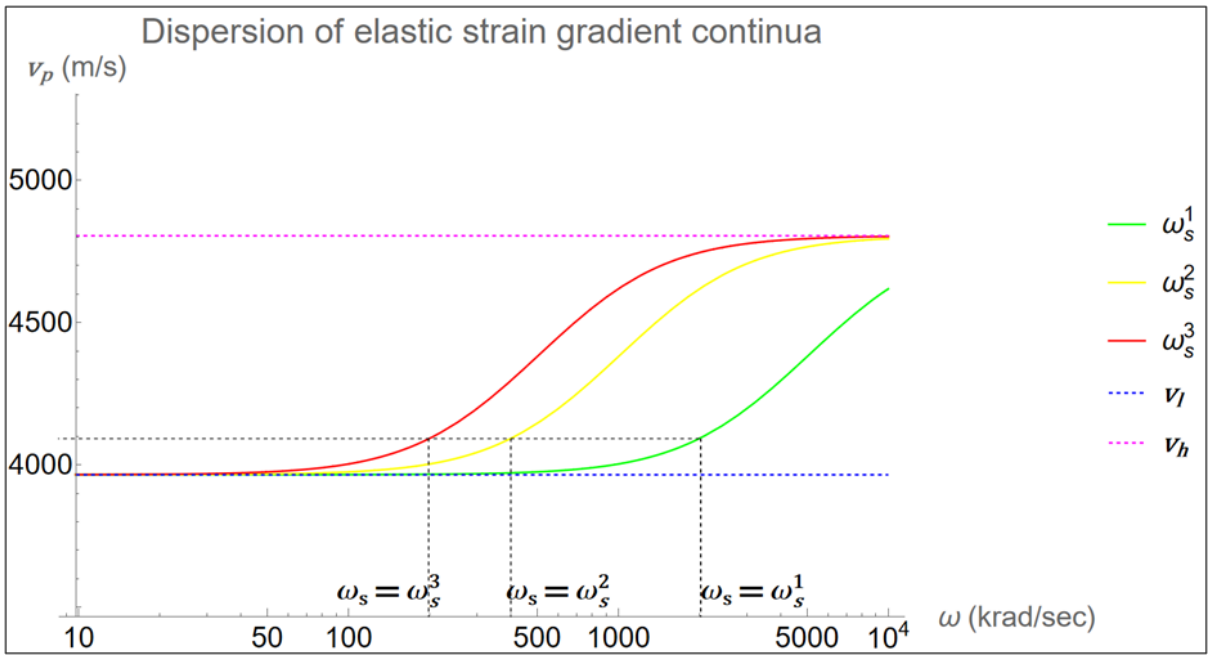

Figure 2.1: *Phase velocity v_p (m/s) as a function of the frequency ω (krad/s) according eqn. (2.23) for a given value of the phase velocity $v_l = 3{,}965$ m/s in the low-frequency regime, for a double value of the phase velocity $v_h = 4{,}805$ m/s in the high-frequency regime, and for three different values of the characteristic frequency ($\omega_s^1 = 2$ Mrad/s, $\omega_s^2 = 400$ krad/s, and $\omega_s^3 = 200$ krad/s) corresponding, because of equation (2.25), to three different values of the elastic characteristic length ($L_E = 1$ mm, $L_E = 5$ mm, $L_E = 10$ mm). The two asymptotes defined in equations (2.17) and (2.22) are also represented.*

In Figure 2.1, we show from equation (2.24) the plot of the phase velocity v_p for different elastic characteristics $\omega_s = \omega_s^1, \omega_s = \omega_s^2, \omega_s = \omega_s^3$. We observe that for low and high-frequency regimes, the phase velocity tends, respectively, to v_l and to v_h according to euqations (2.17) and (2.22). Besides, the transition between these two regimes occurs at the characteristic frequency $\omega = \omega_s$, which, because of equation (2.25), depends upon the elastic characteristic length L_E.

2.2 1D standard viscous dissipative model

In this section, we reconsider the propagation problem in the context of a non-conservative 1D viscous dissipative model. Indeed, dissipation is always present in natural phenomena, and, at

the same time, it yields wave dispersion. However, in this case, the mathematical treatment is more complicated, and, for the sake of simplicity, we avoid considering strain gradient effects superposed to viscous effects simultaneously.

2.2.1 Variational formulation

We consider again the action functional expression (2.1) and, as recalled above, neglect all the second gradient contributions from equations (2.2), (2.3) and (2.4), as following

$$K = \int_0^L \frac{1}{2}\rho \dot{u}^2 \, dx, \tag{2.26}$$

$$W^{\text{int}} = \int_0^L \frac{1}{2} k_1 u'^2 \, dx, \tag{2.27}$$

$$W^{\text{ext}} = \left[F_0^{\text{ext}} u\right]_{x=0} + \left[F_L^{\text{ext}} u\right]_{x=L} + \int_0^L b_n u \, dx. \tag{2.28}$$

The variational principle expression (2.1) is replaced, due to dissipation, by the extended Rayleigh–Hamilton principle, which postulates that the variation of the action δA is connected to the Rayleigh function R

$$\delta A = \int_{t_0}^{t_1} \left\{ \int_0^L \left(\delta K - \delta W^{\text{int}} + \delta W^{\text{ext}} \right) dx \right\} dt = \int_{t_0}^{t_1} \int_0^L \left(\frac{\delta R}{\delta \dot{u}} \delta u + \frac{\delta R}{\delta \dot{u}'} \delta u' \right) dx. \tag{2.29}$$

Here, R is defined as

$$R = \int_0^L \left(\frac{1}{2} c \dot{u}^2 + \frac{1}{2} c_1 \dot{u}'^2 \right) dx. \tag{2.30}$$

Here, c and c_1 represent the a distributed viscous damping proportional to the velocity and internal structural viscosity coefficients, respectively. The two mechanisms act at different kinematic levels (velocity vs. velocity gradient), leading to distinct attenuation behaviors. The term governed by c represents a viscous damping proportional to the local velocity, acting along the entire domain as a distributed dissipation mechanism, similar to the resistance experienced by a body moving in a viscous fluid. In contrast, the term proportional to $\dot{u}'^2$, governed by c_1, corresponds to an internal structural viscosity of Kelvin–Voigt type, associated with spatial gradients of the velocity field; this mechanism can be interpreted as the viscous resistance of the material to deformation, analogous to a Kelvin–Voigt element (spring and dashpot in parallel), where stress depends on both strain and strain rate.
Replacing equations (2.26), (2.27), (2.28) and (2.30) into equation (2.29) and calculating the variation, we find

$$\begin{aligned} \delta A &= \int_{t_0}^{t_1} \left\{ \int_0^L \left(\rho \dot{u} \delta \dot{u} - k_1 u' \delta u' + b_n \delta u \right) dx + \left[F_0^{\text{ext}} \delta u\right]_{x=0} + \left[F_L^{\text{ext}} \delta u\right]_{x=L} \right\} dt \\ &= \int_{t_0}^{t_1} \left\{ \int_0^L \left(c \dot{u} \delta u + c_1 \dot{u}' \delta u' \right) dx \right\} dt. \end{aligned} \tag{2.31}$$

After integrating by parts in both space and time, and collecting dissipative terms on the left-hand side, we derive

$$\begin{aligned} &\int_{t_0}^{t_1} \left\{ \int_0^L \delta u \left(-\rho \ddot{u} + k_1 u'' - c \dot{u} + c_1 \ddot{u}'' + b_n \right) dx \right\} dt \\ &\qquad + \int_{t_0}^{t_1} \delta u(0) \left[-F_0^{\text{ext}} - k_1 u' - c_1 \dot{u}' \right]_{x=0} dt \\ &\qquad + \int_{t_0}^{t_1} \delta u(L) \left[F_L^{\text{ext}} - k_1 u' - c_1 \dot{u}' \right]_{x=L} dt = 0, \end{aligned} \tag{2.32}$$

where the displacement $u(x,t)$ is assumed, as in the previous section, to be prescribed at two instants of time at $t = t_0$ and $t = t_1$ so that the displacement variations, at those times, are null: $\delta u(x, t = t_0) = \delta u(x, t = t_1) = 0$.
The extended Rayleigh–Hamilton principle, and therefore equation (2.32), must hold for every admissible variation of the displacement field u. The last two lines of equation (2.32) must therefore be null.
On one hand, if the displacement u is prescribed at the boundary (i.e., the left-hand sides of the following equations (2.33) and/or (2.34) are satisfied), then their variations are null as well as the corresponding line of equation (2.32). On the other hand, in order to make null the same lines of equation (2.32), if the mentioned kinematic conditions are not prescribed, then the right-hand sides of the following equations (2.33) and/or (2.34) are satisfied

$$u(0,t) = u_0(t) \quad \text{or} \quad k_1 u' + c_1 \dot{u}'(x = 0, t) = -F_0^{\text{ext}}, \tag{2.33}$$

$$u(L,t) = u_L(t) \quad \text{or} \quad k_1 u' + c_1 \dot{u}'(x = L, t) = F_L^{\text{ext}}, \tag{2.34}$$

for every instant of time, i.e., $\forall t \in \mathbb{R}$.
Finally, also the first line of equation (2.32) must be zero for every admissible variation δu of the displacement field. Thus, because of the arbitrariness of δu, it results

$$\rho \ddot{u} + c\dot{u} - k_1 u'' - c_1 \dot{u}'' - b_n = 0, \quad \forall x \in [0, L], \quad \forall t \in \mathbb{R}, \tag{2.35}$$

that is, a Partial Differential Equation (PDE) of the 2nd order in space and time, governing the evolution of the displacement field $u(x,t)$ of the investigated model.
Also equation (2.35), in the assumption of no external distributed actions ($b_n = 0$), might support solutions for the displacement field in the wave form expression (2.13). Indeed, calculating the derivatives of equation (2.13) and substituting into equation (2.35), it results

$$-\rho\omega^2 + i\omega c + k_1 k_w^2 + c_1 i\omega k_w^2 = 0, \tag{2.36}$$

that is, a 2nd degree algebraic equation in terms of k_w, that in the next subsections will be solved for $c = 0$ and for $c_1 = 0$, respectively.

2.2.2 Wave form solution for elastic solids with damping ($c \neq 0, c_1 = 0$)

By neglecting the internal structural viscosity, i.e., by considering $c_1 = 0$, equation (2.36) can be rewritten as

$$k_w^2 = \frac{\rho\omega^2 - i\omega c}{k_1} = \frac{\rho\omega^2}{k_1} - i\frac{\omega c}{k_1}, \tag{2.37}$$

admitting therefore two solutions for k_w, both characterized by an imaginary and a real part. Using the Euler complex form, we rewrite equation (2.37) as

$$k_w^2 = a - ib = \rho_2 e^{i\Omega_2}, \tag{2.38}$$

where the real values a (real part of k_w^2), b (the opposite of the imaginary part of k_w^2), Ω_2 (the phase of k_w^2), and ρ_2 (the amplitude of k_w^2) take the following forms

$$a = \frac{\rho\omega^2}{k_1}, \quad b = \frac{c\omega}{k_1}, \tag{2.39}$$

$$\Omega_2 = -\arctan(\frac{b}{a} + 2n\pi) = -\arctan(\frac{c}{\omega\rho} + 2n\pi), \quad \forall n \in \mathbb{N}, \tag{2.40}$$

$$\rho_2 = \sqrt{a^2 + b^2} = \frac{\omega}{k_1}\sqrt{\rho^2\omega^2 + c^2}. \tag{2.41}$$

with n being an integer number. Meaningful values for n are 0 or 1.

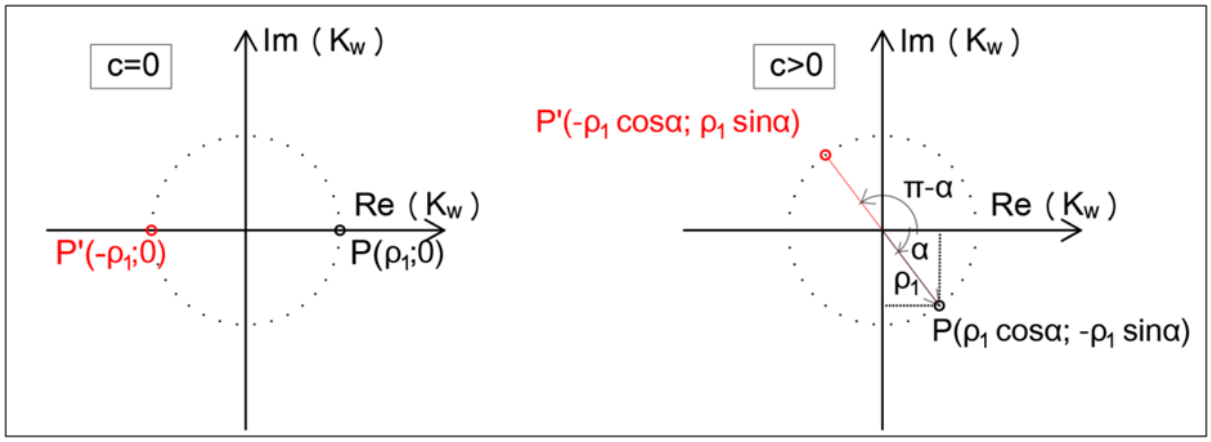

Figure 2.2: *Schematic representation of the wave number with $c_1 = 0$ in the complex plane. On the left-hand side we have the non-dissipative case with $c = 0$. On the right-hand side we have the dissipative case with $c > 0$.*

The wave number is the square root of equation (2.38), so it results

$$k_w = \sqrt{\rho_2} e^{i\frac{\Omega_2}{2}} = \rho_1 \cos(\Omega_1) + i\rho_1 \sin(\Omega_1), \tag{2.42}$$

where, with the aid of equations (2.39), (2.40), and (2.41), we obtain

$$\rho_1 = \sqrt{\rho_2} = \sqrt[4]{a^2 + b^2} = \omega\sqrt{\frac{\rho}{k_1}}\sqrt[4]{1 + \frac{c^2}{\omega^2\rho^2}}, \tag{2.43}$$

and

$$\Omega_1 = \frac{\Omega_2}{2} = -\frac{1}{2}\arctan\left(\frac{c}{\rho\omega} + n\pi\right) = -\alpha + n\pi, \quad \forall n \in \mathbb{N}. \tag{2.44}$$

Thus, we have

$$\mathrm{Re}(k_w) = \omega\sqrt{\frac{\rho}{k_1}}\sqrt[4]{1 + \frac{c^2}{\omega^2\rho^2}}\cos\left(-\frac{1}{2}\arctan\left(\frac{c}{\rho\omega} + n\pi\right)\right) = \rho_1\cos(-\alpha + n\pi), \tag{2.45}$$

and

$$\mathrm{Im}(k_w) = \omega\sqrt{\frac{\rho}{k_1}}\sqrt[4]{1 + \frac{c^2}{\omega^2\rho^2}}\sin\left(-\frac{1}{2}\arctan\left(\frac{c}{\rho\omega} + n\pi\right)\right) = \rho_1\sin(-\alpha + n\pi). \tag{2.46}$$

When $n = 0$ or n is an even integer, it corresponds (see the black solution in the right-hand side of Figure 2.2) to a positive real part of the wave number ($\mathrm{Re}(k_w) > 0$), i.e., a wave propagating towards the positive values of x, and to a negative imaginary part of the wave number ($\mathrm{Im}(k_w) < 0$), i.e., a wave that is attenuating towards the same positive values of x. On the other hand, when $n = 1$ or n is an odd integer, it corresponds (see the red solution in the right-hand side of Figure 2.2) to a negative real part of the wave number ($\mathrm{Re}(k_w) < 0$), i.e., a wave propagating towards the negative values of x, and to a positive imaginary part of the wave number ($\mathrm{Im}(k_w) > 0$), i.e., a wave that is attenuating towards the same negative values of x.

Let us now better explain Figure 2.2. On the left-hand side, we represent the non-attenuated case with $c = 0$, where the two solutions of equation (2.36) are real ($k_w = \pm\rho_1$) and correspond to $\mathrm{Im}(k_w) = 0$, with waves propagating towards the left (negative wave number with $k_w = -\rho_1$) and the right (positive wave number with $k_w = \rho_1$) parts of the 1D domain. On the right-hand

side of Figure 2.2, we represent the attenuated case with $c > 0$, where the two solutions of equation (2.36) are complex. The real parts, as for the left-hand side case, correspond to a wave propagating towards the left part of the 1D domain for $n = 1$ or another odd integer (negative real part of the wave number with $\mathrm{Re}(k_w) = \rho_1 \cos(-\alpha + \pi) = -\rho_1 \cos(\alpha) < 0$), and towards the right part of the 1D domain for $n = 0$ or another even integer (positive real part of the wave number with $\mathrm{Re}(k_w) = \rho_1 \cos(\alpha) > 0$).
For the positive real part of the wave number ($n = 0$ or an even integer, i.e., for a wave propagating towards the positive values of x), we have from equation (2.42) a negative imaginary part $\mathrm{Im}(k_w) = -\rho_1 \sin(\alpha) < 0$, which corresponds to an attenuation in space of a signal propagating towards the right part of the 1D domain. The reason is that, from equation (2.13), the displacement amplitude is proportional to the factor

$$e^{-ik_w x} = e^{-i\mathrm{Re}(k_w)x + \mathrm{Im}(k_w)x}, \tag{2.47}$$

which tends to zero for large positive values of the position x with $\mathrm{Im}(k_w) < 0$. For the negative real part of the wave number ($n = 1$ or another odd integer, i.e., for a wave propagating towards the negative values of x), we have from equation (2.46) a positive imaginary part $\mathrm{Im}(k_w) = \rho_1 \sin(-\alpha + \pi) = \rho_1 \sin(\alpha) > 0$, also corresponding to an attenuation in space (of a signal propagating towards the left), since from equation (2.47) the displacement amplitude is proportional to the same factor $e^{-ik_w x}$, which again tends to zero for large negative values of the position x with $\mathrm{Im}(k_w) > 0$.
Finally, equation (2.16) is also used to calculate the phase velocity in combination with equation (2.42)

$$\begin{aligned}(v_p)_{c_1=0} &= \mathrm{Re}\left(\frac{\omega}{k_w}\right) = \mathrm{Re}\left(\frac{\omega}{\rho_1 e^{-i\Omega_1}}\right) = \frac{\omega}{\rho_1}\cos(\Omega_1) \\ &= \sqrt{\frac{k_1}{\rho}}\sqrt[4]{\frac{1}{1+\left(\frac{c}{\omega\rho}\right)^2}}\cos\left(\frac{1}{2}\arctan\left(\frac{c}{\omega\rho}\right)\right).\end{aligned} \tag{2.48}$$

which, similarly to the previous section, can be rewritten as

$$(v_p)_{c_1=0} = \sqrt{\frac{k_1}{\rho}}\sqrt[4]{\frac{1}{1+\left(\frac{\omega_c}{\omega}\right)^2}}\cos\left(\frac{1}{2}\arctan\left(\frac{\omega_c}{\omega}\right)\right), \tag{2.49}$$

with the characteristic frequency

$$\omega_c = \frac{c}{\rho}. \tag{2.50}$$

First of all, we observe that the phase velocity is a decreasing function of the viscosity coefficient c. On one hand, for low viscosity, the phase velocity tends to the value evaluated by using the classic linear elastodynamic theory

$$\lim_{c\to 0}(v_p)_{c_1=0} = \sqrt{\frac{k_1}{\rho}} = v_l, \tag{2.51}$$

the same velocity of the low-frequency regime for the non-dissipative second gradient case v_l (see Section 2.1.2). On the other hand, as the viscosity c increases, the phase velocity approaches, zero

$$\lim_{c\to\infty}(v_p)_{c_1=0} = 0. \tag{2.52}$$

To better understand this behavior, we compare it to the fall of an object attached to a parachute in a viscous medium: the higher the viscosity, the lower the velocity.

Secondly, we analyze the dispersion relation (2.48), i.e., the dependence of the phase velocity on the frequency. For a fixed viscosity value c, the two limits for low and high frequencies are independent of c

$$\lim_{\omega\to 0}(v_p)_{c_1=0} = 0, \tag{2.53}$$

$$\lim_{\omega\to \infty}(v_p)_{c_1=0} = \sqrt{\frac{k_1}{\rho}}. \tag{2.54}$$

Thus, the viscosity has a stiffening effect for higher frequencies, a softening effect for lower frequencies, and the transition from low-frequency to high-frequency regimes occurs at the characteristic frequency ω_c according equation (2.50). As the viscosity c increases, this transition occurs at higher frequencies.
In Figure 2.3, we show the phase velocity expression (2.49) for different values of the characteristic frequency expression ω_c (2.50) as a function of frequency. As highlighted above, at a certain frequency, as the damping and the corresponding characteristic frequency value decrease, the phase velocity increases towards the phase velocity expression (2.51) of the classical linear elastodynamics. However, as the damping and the corresponding characteristic frequency expression ω_c (2.50) increase, the phase velocity decreases towards zero. Moreover, given a fixed phase velocity, we observe an increase in the characteristic frequency as the damping increases.

2.2.3 Wave form solution for Kelvin–Voigt viscous material ($c = 0, c_1 \neq 0$)

In the case of a Kelvin–Voigt material ($c_1 \neq 0$), and neglecting the viscous interaction between the investigated 1D body and the surrounding environment ($c = 0$), equation (2.36) can be rewritten as

$$k_w^2 = \frac{\rho\omega^2}{k_1 + i\omega c_1}. \tag{2.55}$$

In order to adopt, as in the previous subsection, the Euler complex form, we use the following algebraic properties

$$\begin{aligned} k_w^2 &= \frac{\rho\omega^2}{k_1 + i\omega c_1}\frac{k_1 - i\omega c_1}{k_1 - i\omega c_1} \\ &= \frac{\rho\omega^2 k_1}{k_1^2 + \omega^2 c_1^2} - i\frac{\rho\omega^3 c_1}{k_1^2 + \omega^2 c_1^2} \\ &= a_1 - ib_1 = \rho_2 e^{i\Omega_2}, \end{aligned} \tag{2.56}$$

where, in this case, the real values a_1 (real part of k_w^2), b_1 (the opposite of the imaginary part of k_w^2), Ω_2 (the phase of k_w^2), and ρ_2 (the amplitude of k_w^2) correspond to

$$a_1 = \frac{\rho\omega^2 k_1}{k_1^2 + \omega^2 c_1^2}, \quad b_1 = \frac{\rho\omega^3 c_1}{k_1^2 + \omega^2 c_1^2}, \tag{2.57}$$

$$\Omega_2 = -\arctan(\frac{b_1}{a_1} + 2n\pi) = -\arctan(\frac{\omega c_1}{k_1} + 2n\pi), \quad \forall n \in \mathbb{N}, \tag{2.58}$$

$$\rho_2 = \sqrt{a_1^2 + b_1^2} = \frac{\rho\omega\sqrt{\omega^2 k_1^2 + \omega^3 c_1^2}}{k_1^2 + \omega^2 c_1^2}. \tag{2.59}$$

The wave number is the square root of equation (2.55), so it results

$$k_w = \sqrt{\rho_2} e^{i\frac{\Omega_2}{2}} = \rho_1\cos(\Omega_1) + i\rho_1\sin(\Omega_1), \tag{2.60}$$

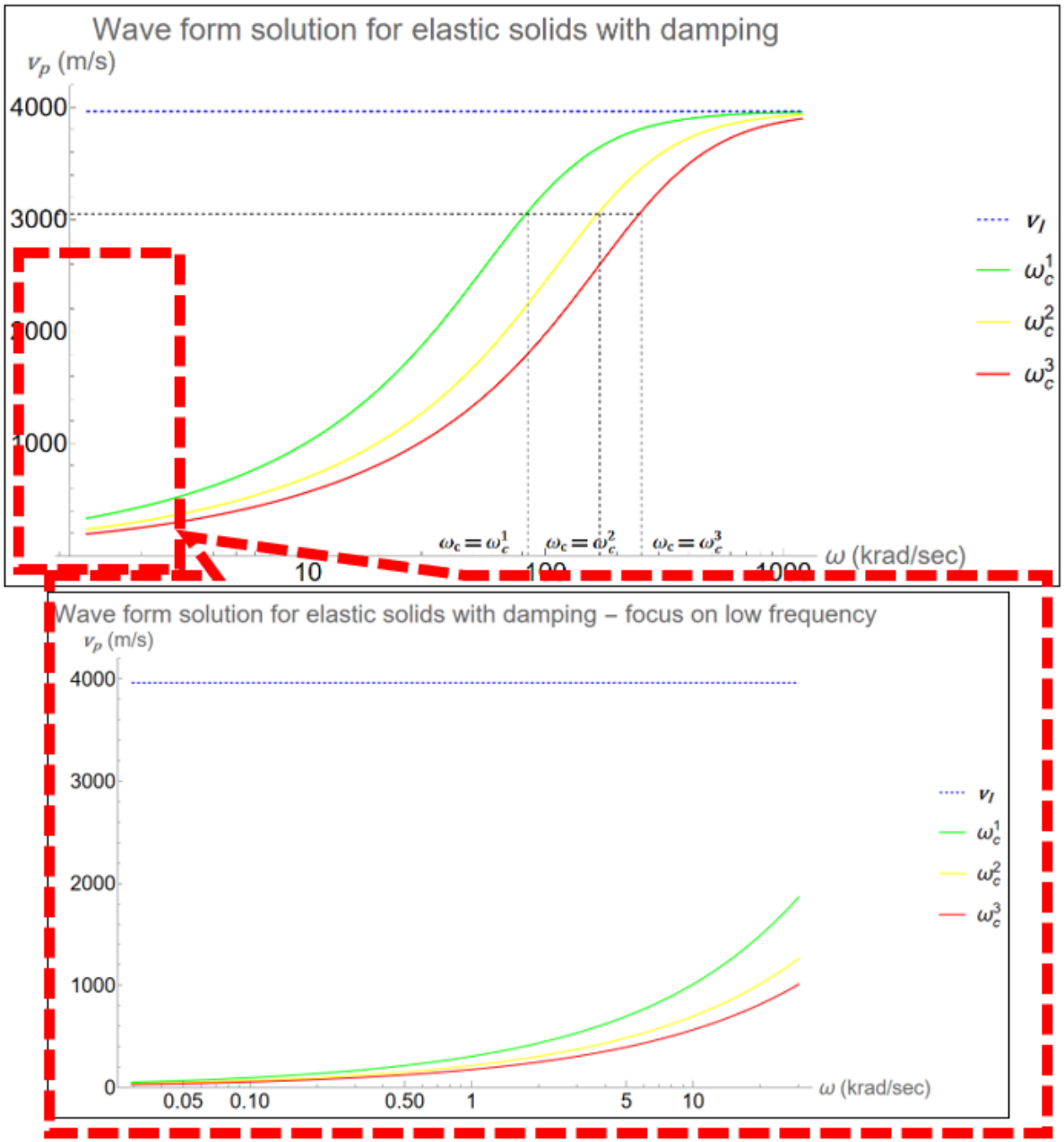

Figure 2.3: *The phase velocity v_p (m/s), as a function of the frequency ω (krad/s) according eqn. (2.49) for a viscoelastic material ($c_1 = 0$) and for three different values of damping ($c = 200{,}000\,\mathrm{kg/(m\,s)}$, $c = 400{,}000\,\mathrm{kg/(m\,s)}$, $c = 600{,}000\,\mathrm{kg/(m\,s)}$), corresponding, because of equation (2.50), to three different characteristic frequencies ($\omega_c^1 = 85\,\mathrm{krad/s}$, $\omega_c^2 = 140\,\mathrm{krad/s}$, and $\omega_c^3 = 240\,\mathrm{krad/s}$). The blue asymptote, defined in equation (2.51), is the classical linear elastic phase velocity ($c_1 = 0$) with no damping ($c = 0$), that is, $v_l = 3{,}965\,\mathrm{m/s}$.*

where, by equations (2.57), (2.58), and (2.59), we obtain

$$\rho_1 = \sqrt{\rho_2} = \sqrt[4]{a_1^2 + b_1^2} = \omega\sqrt{\frac{\rho}{k_1}}\sqrt[4]{\frac{1}{1+\left(\frac{\omega c_1}{k_1}\right)^2}}, \tag{2.61}$$

$$\Omega_1 = \frac{\Omega_2}{2} = -\frac{1}{2}\arctan\left(\frac{\omega c_1}{k_1} + n\pi\right) = -\alpha + n\pi, \quad \forall n \in \mathbb{N}. \tag{2.62}$$

Following the same steps described in the previous subsection, and using equation (2.42), the

real and imaginary parts of the wave number are, respectively

$$\mathrm{Re}(k_w) = \omega\sqrt{\frac{\rho}{k_1}}\sqrt[4]{\frac{1}{1+\left(\frac{\omega c_1}{k_1}\right)^2}}\cos\left(-\frac{1}{2}\arctan\left(\frac{\omega c_1}{k_1}+n\pi\right)\right) = \rho_1\cos(-\alpha+n\pi), \tag{2.63}$$

$$\mathrm{Im}(k_w) = \omega\sqrt{\frac{\rho}{k_1}}\sqrt[4]{\frac{1}{1+\left(\frac{\omega c_1}{k_1}\right)^2}}\sin\left(-\frac{1}{2}\arctan\left(\frac{\omega c_1}{k_1}+n\pi\right)\right) = \rho_1\sin(-\alpha+n\pi). \tag{2.64}$$

As in the previous subsection, $n = 0$ or an even integer corresponds to a positive real part of the wave number ($\mathrm{Re}(k_w) > 0$) and a negative imaginary part ($\mathrm{Im}(k_w) < 0$); $n = 1$ or an odd integer corresponds to a negative real part ($\mathrm{Re}(k_w) < 0$) and a positive imaginary part ($\mathrm{Im}(k_w) > 0$). Thus, the signs of the real and imaginary parts of the wave number correspond to wave amplitude attenuation, which decreases in the propagation direction.
In conclusion, the phase velocity for the Kelvin–Voigt material, assuming the real part of the wave number $\mathrm{Re}(k_w)$ and neglecting all second gradient contributions, is

$$(v_p)_{c=0} = \mathrm{Re}\left(\frac{\omega}{k_w}\right) = \sqrt{\frac{k_1}{\rho}}\sqrt[4]{1+\frac{\omega^2 c_1^2}{k_1^2}}\cos\left(\frac{1}{2}\arctan\left(\frac{\omega c_1}{k_1}\right)\right). \tag{2.65}$$

A characteristic frequency can be defined as

$$\omega_{c_1} = \frac{k_1}{c_1}, \tag{2.66}$$

thus resulting

$$(v_p)_{c=0} = \mathrm{Re}\left(\frac{\omega}{k_w}\right) = \sqrt{\frac{k_1}{\rho}}\sqrt[4]{1+\left(\frac{\omega}{\omega_{c_1}}\right)^2}\cos\left(\frac{1}{2}\arctan\left(\frac{\omega}{\omega_{c_1}}\right)\right). \tag{2.67}$$

First of all, we observe that the phase velocity is an increasing function of the viscosity coefficient c_1. On one hand, for low internal material viscosity c_1 we have that the phase velocity tends to the classic linear elastodynamic theory velocity

$$\lim_{c_1\to 0}(v_p)_{c=0} = \sqrt{\frac{k_1}{\rho}}, \tag{2.68}$$

that is, the same velocity of the low frequency regime for the non-dissipative second gradient case. On the other hand, as the internal structural viscosity c_1 increases, the phase velocity evaluated at a fixed frequency increases to infinity

$$\lim_{c_1\to\infty}(v_p)_{c=0} = \infty. \tag{2.69}$$

Thus, we can deduce that the internal viscosity rise has a stiffening effect on a material under dynamic loading.
Secondly, we analyze the dispersion equation (2.65), i.e., the dependence of the phase velocity with the frequency. For a fixed value of the internal structural viscosity c_1, as expected, for frequencies approaching 0, the phase velocity tends to the classic linear elastic value, while for frequencies approaching infinity, the phase velocity tends to infinity. Thus, the two limits for low and high frequency regime are independent of the internal structural viscosity c_1

$$\lim_{\omega\to 0}(v_p)_{c=0} = \sqrt{\frac{k_1}{\rho}}, \tag{2.70}$$

$$\lim_{\omega\to\infty}(v_p)_{c=0}=\infty. \tag{2.71}$$

In conclusion, we can state that, similarly to the previous subsection, the internal viscosity has a stiffening effect for higher frequency, a softening effect for low frequency, and the transition between low frequency regime and high frequency regime is obtained in correspondence of the characteristic frequency expression ω_{c_1} (2.66). As the viscosity c_1 increases, the transition zone from low to high frequency regime as the in-phase velocity increases occurs at lower frequencies. In Figure 2.4 we show the phase velocity expression (2.65) for different values of the characteristic frequency equation (2.66), i.e., of the viscosity c_1. As highlighted before, for a fixed frequency, on one hand, as the internal viscosity value increases, the velocity phase also increases, toward infinity, but on the other hand, as the internal viscosity value decreases, the phase velocity tends to the classical linear elasticity velocity expression (2.68). Moreover, for a fixed phase velocity, we observe a characteristic frequency increase, as the internal viscosity decreases. Finally, in the present case there is not an asymptotic value of the velocity for the high frequency range, since the phase velocity tends to infinity as the frequency goes to infinity. This asymptotic behavior, although mathematically consistent within the Kelvin–Voigt framework, is not physically realistic and highlights a limitation of the adopted constitutive model at high frequencies.

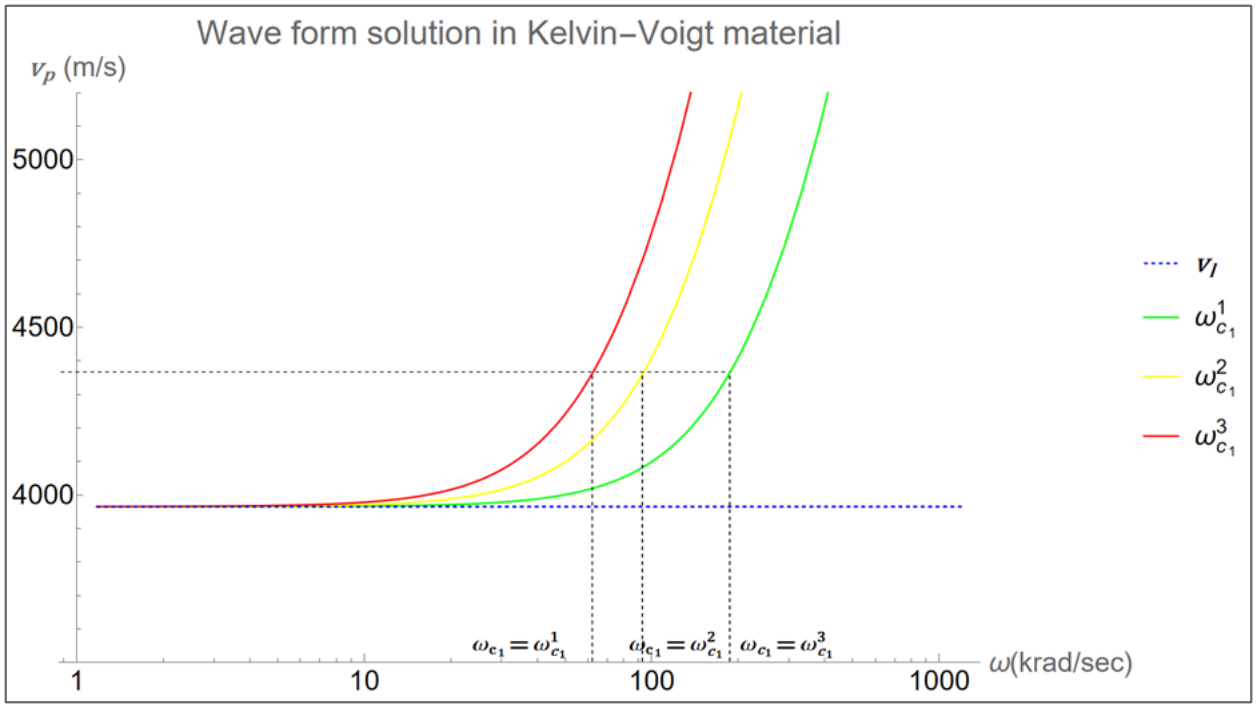

Figure 2.4: *Phase velocity v_p (m/s) as a function of frequency ω (krad/s), according to Eq. (2.67) for a Kelvin–Voigt model, shown for three different values of internal viscosity: $c_1^{(1)} = 200\times10^6\,\mathrm{N\,s/m^2}$, $c_1^{(2)} = 400\times10^6\,\mathrm{N\,s/m^2}$, and $c_1^{(3)} = 600\times10^6\,\mathrm{N\,s/m^2}$. According to Eq. (2.66), these correspond to three different values of the characteristic frequency: $\omega_{c_1}^{(1)} = 62\,\mathrm{krad/s}$, $\omega_{c_1}^{(2)} = 93\,\mathrm{krad/s}$, and $\omega_{c_1}^{(3)} = 187\,\mathrm{krad/s}$, respectively. The blue asymptote, defined in Eq. (2.68), represents the classical linear elastic phase velocity ($c_1 = 0$), i.e., in the absence of viscous damping ($c = 0$), equal to $v_l = 3965\,\mathrm{m/s}$.*

2.3 Experimental tests

2.3.1 Initial remarks

In order to validate the proposed theoretical models to predict the mechanical properties of some widely diffused construction materials, we performed ultrasonic tests at the laboratory M. Salvati of Polytechnic University of Bari. In particular, we have carried out ultrasonic contact tests by the through-transmission method, i.e., by using a couple ultrasonic longitudinal Panametrics narrowband piezoelectric transducers. Transducers with different values of the resonance central frequency were attached to the two opposite faces of each tested specimen. Other components of the experimental setup are: (1) an ultrasonic pulser/receiver Panametrics 5072PR for generating and receiving the ultrasonic waves; (2) a digital oscilloscope KEYSIGHT DSOS254A (2.5 GHz, 4 channels) for monitoring the ultrasonic signals. In particular, ultrasonic contact tests have been performed by using 6 different couples of longitudinal waves transducers, operating at central frequencies of 50 kHz, 250 kHz, 500 kHz, 1 MHz and 2.25 MHz, respectively. The oscilloscope allowed to measure the travelling time that is the Time Of Flight (TOF), in μs, employed by the wave in the path from the emitting transducer to the receiving one. So, the phase velocity of the tested specimen material is determined by the ratio between the space traveled by the acoustic wave in the specimen (practically, the thickness of the specimen orthogonally to the transducers) and the TOF.
Preliminarily, it is worth noting that, for a correct interpretation of the test results, it could be useful to take into consideration some laboratory measurement errors, that can be caused, for instance, by motion of samples and transducers during measurement, by the variable pressure applied on the transducers by the hands of the technician during the test, by disturbing effects in the area of contact between the transducer and the specimen surface, by the sensibility of the instruments, and of course by some intrinsic characteristics of the sample itself (internal fractures, inhomogeneity, anisotropy, characteristic length, etc.). In the last years, some contactless techniques such as the laser-ultrasonic technique and the ultrasonic immersion technique were proposed for the mitigation of measurement errors during ultrasonic tests. These techniques are suitable for investigating the mechanical behavior of complex materials like anisotropic materials, which have a different mechanical – and acoustic – response depending on the direction of propagation of the acoustic waves. To this aim, an innovative goniometric device has been proposed[30]capable of rotating the material specimen immersed in a water tank in order to test the acoustic response of the material along different directions of propagation of ultrasonic beam. Moreover, a fixed gripping system was proposed to minimize errors due to the pressure exerted on the transducer for the study of the damage of concrete samples during cyclic compression tests, based on the variation of linear and nonlinear ultrasonic parameters[31].
When devices like those above described are not suitable to be used on a field study, like in the case of the present work, an alternative is to examine experimental data through a probabilistic approach. Thus, we proceeded by carrying out more phase velocity measurements on a sample of the same material for each available transducer central frequency, aimed to obtain an average value of phase velocity that could be considered as the reference one.
Another important issue is the choice of the material to be investigated. For this specific study, we have analyzed both natural and artificial construction materials. Specifically, tests were carried out on sandstones and concrete. Specifically, we analyzed sandstone specimens collected from the Manciano Formation outcropping in Central Italy, specifically in Bagni di Saint Agostino location along the Tyrrhenian Sea shoreline (see Figure 2.5) with the aim of ascertaining the influence of the microstructure and average grain size on the dispersity of acoustic waves.
The microstructure of this sedimentary rock is a moderately sorted very fine to fine calcarenite sandstone, with carbonate cement and clay matrix. Grains are sub-angular to sub-rounded. Monomineralic quartz is dominant, and feldspar (plagioclase and feldspar) grains are common

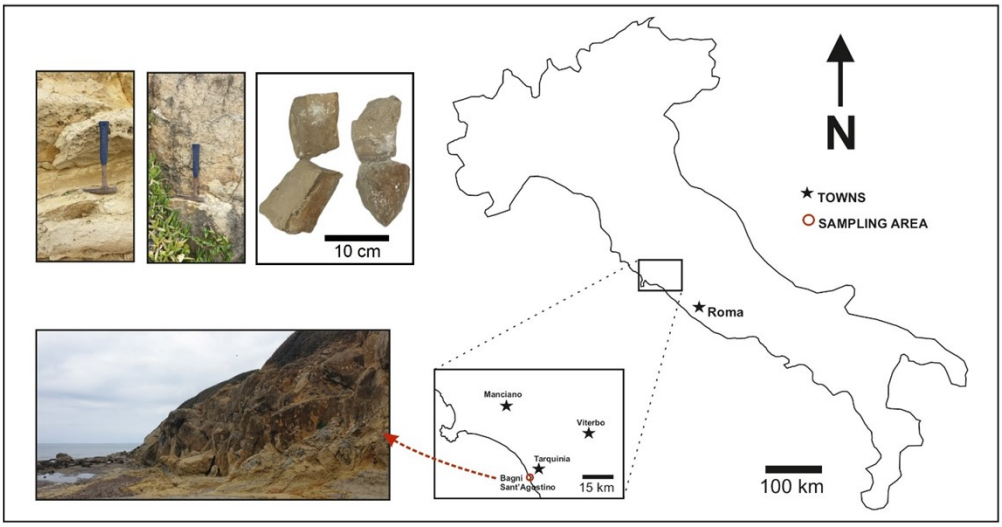

Figure 2.5: *Location of the sampling area, outcrop and samples collected - sandstone.*

with minor biotite grains. Minor lithic include siliciclastic and carbonate sedimentary lithic fragments and low-grade meta-sedimentary lithic fragments. Carbonate bioclasts are dominant and include calcite spicule, echinoderms, benthic foraminifers and planktic tests. The microstructure shows that this wide variety of grain types are no larger than a millimeter under a transmitted light microscope (see Figure 2.6). For what concerns concrete specimens, the

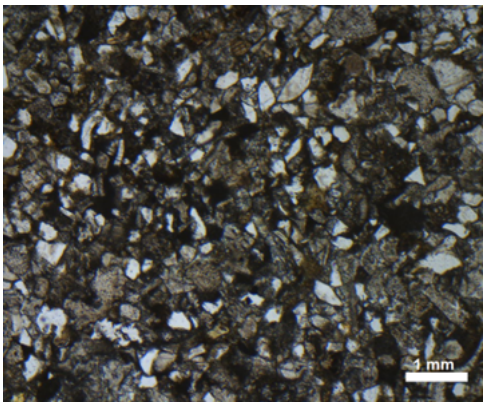

Figure 2.6: *Manciano sandstones sampled at Sant'Agostino on the Tyrrhenian Sea shoreline show a microstructure with clast sizes of less than 1 mm under a transmitted light optical microscope.*

microstructure is characterized by a high assortment of fine to very large carbonate fragments in a matrix of carbonate cement and clay. The grains profile is sub-angular to angular. The angular nature of carbonate clasts contributes to the concrete's cohesion. What particularly distinguishes this material is the presence of large angular clasts, which can reach sizes of up to about 3 cm (Figure 2.7). These clasts are mainly of carbonate origin, with a dense and compact structure. Their presence contributes to the cement's considerable mechanical strength and greater seismic wave transmission capacity.
Concerning the geometry of the samples used for the ultrasonic experiments, cylindrical sandstone samples were adopted with heights of 32 mm, 60 mm, and 80 mm, and an irregular circular face with an average diameter of 8 cm. As for the concrete samples, the material was cut from the same batch of concrete into cubes with face dimensions of 15x15 cm, and lengths of 44 mm, 71 mm, and 90 mm. All concrete cubes come from the same concrete pour (class 30/37). The

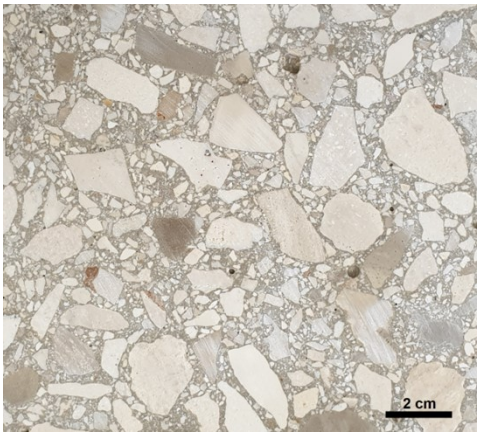

Figure 2.7: *Concrete analyzed in this work showing wide assortment of grains with size up to 3 cm.*

densities of the two materials, measured with the Hydrostatic Weighing Method (Archimedes Principle) in laboratory, are: 2,401 kg/m^3 for the concrete samples and 2,544 kg/m^3 for the sandstone samples.

2.3.2 Data measurements collection and screening

In Table 2.1, we have summarized the results obtained by the ultrasonic contact tests. However, before proceeding further, it is necessary to conduct a preliminary exam of these data, also for excluding anomalous measurements.
Considering that the ratio between the wavelength and the specimen thickness should be less than 1 to allow for the completion of an integer wave travel cycle within the material from one transducer to the other, we see that by the well-known relationship between the wavelength λ, the angular frequency ω, and the phase velocity v_p:

$$v_p = \lambda f = \lambda 2\pi\omega, \tag{2.72}$$

we observe that, for concrete samples, to a frequency of 50 kHz corresponds a wavelength of 8 cm, which is greater than the thickness of the specimen (7.1 cm or 4.4 cm). Consequently, these measurements cannot be considered reliable. Furthermore, for measurement number 13 (frequency 2.25 MHz, sample thickness 90 mm) we observed such a high attenuation that it was impossible to reliably measure the TOF. Finally, measurements number 14, 18, and 21 provided anomalous values for the phase velocity, significantly higher or lower compared to the average value of the other measurements. Therefore, these data have been disregarded as considered not reliable.
It is worth to note that the scale separation across the lenghts related to microstructures, waves and samples is not always guaranteed in the present study. The reason for such a choice is not only to emphasize the dispersive characteristics of the wave propagation, but also because these are the ranges that are often used in the present non-destructive evaluation techniques by engineers.
In conclusion, excluding the above commented measurements, we considered a set of 16 ultrasonic results for the validation of the discussed theoretical models.

2.3.3 Strain gradient elastic model – validation and results interpretation

First, we consider the elastic strain gradient model in Section 2.1, for which the expression of the phase velocity is given by equation (2.23), and depends on the unknown material param-

Exp	Material	Measurement	f [kHz]	L [mm]	TOF [s]	v_p [m/s]
1	Concrete samples	1	50	99	2.590×10^{-5}	3,821.995
		2	50	71	1.909×10^{-5}	3,718.816
		3	50	44	1.260×10^{-5}	3,491.925
		4	250	99	2.410×10^{-5}	4,107.219
		5	250	71	1.819×10^{-5}	3,903.158
		6	250	44	1.170×10^{-5}	3,761.488
		7	500	99	2.423×10^{-5}	4,086.148
		8	500	71	1.747×10^{-5}	4,063.017
		9	500	44	1.115×10^{-5}	3,944.809
		10	1,000	99	2.226×10^{-5}	4,448.399
		11	1,000	71	1.672×10^{-5}	4,246.691
		12	1,000	44	1.016×10^{-5}	4,332.457
		13	2,250	99	8.043×10^{-8}	1,230,883.999
		14	2,250	71	9.804×10^{-6}	7,241.669
		15	2,250	44	1.006×10^{-5}	4,374.671
2	Sandstone samples	16	1,000	80	2.079×10^{-5}	3,848.226
		17	1,000	60	1.621×10^{-5}	3,700.780
		18	1,000	32	1.233×10^{-5}	2,596.096
		19	2,250	80	2.043×10^{-5}	3,916.194
		20	2,250	60	1.581×10^{-5}	3,794.970
		21	2,250	32	1.188×10^{-5}	2,692.492

Table 2.2: *Input (frequency, wave travelling time, and sample thickness) and output (phase velocity) data from ultrasonic tests on concrete and sedimentary rock samples.*

eter represented by the elastic characteristic length L_E. For reconstructing the phase velocity function, we applied a least squares interpolation approach by minimizing the function

$$g(v_l, v_h, L_E) = \sum_{i=1}^{n} \left[v_{p_i} - f(\omega_i, v_l, v_h, L_E) \right]^2 , \tag{2.73}$$

i.e., by determining the parameters v_l, v_h, and L_E that minimize the overall approximation error between theoretical previsions and experimental data (ω_i, v_{p_i}) from Table 2.1 (more precisely the average phase velocities v_{p_i} at each frequency ω_i, with $i = 1, n$).
For the concrete sample, we show in Figure 2.8 with the blue line the phase velocity evaluated through the 1-D strain gradient model, according to equation (2.23), to the above minimization procedure. Moreover, the experimental velocity values and the range of the experimental error are indicated. The error has been calculated as the maximum deviation between the experimental data point and the extrapolated regression curve. In detail, it is the maximum value of the differences between the experimental data measured at a certain frequency ω and the predicted value from the model for the same frequency value.
For the considered case, the average value of phase velocity at low-high frequency regime and of the characteristic length are respectively $v_l = 3,965$ m/s, $v_h = 4,805$ m/s, and $L_E = 20$ mm. The maximum error on phase velocity is 231.63 m/s, and the relative error for the low-

frequency regime (particularly relevant for the calculation of the longitudinal elastic modulus) is about 5.8%. The same holds for Figure 2.9, concerning the sandstone samples. Here, the

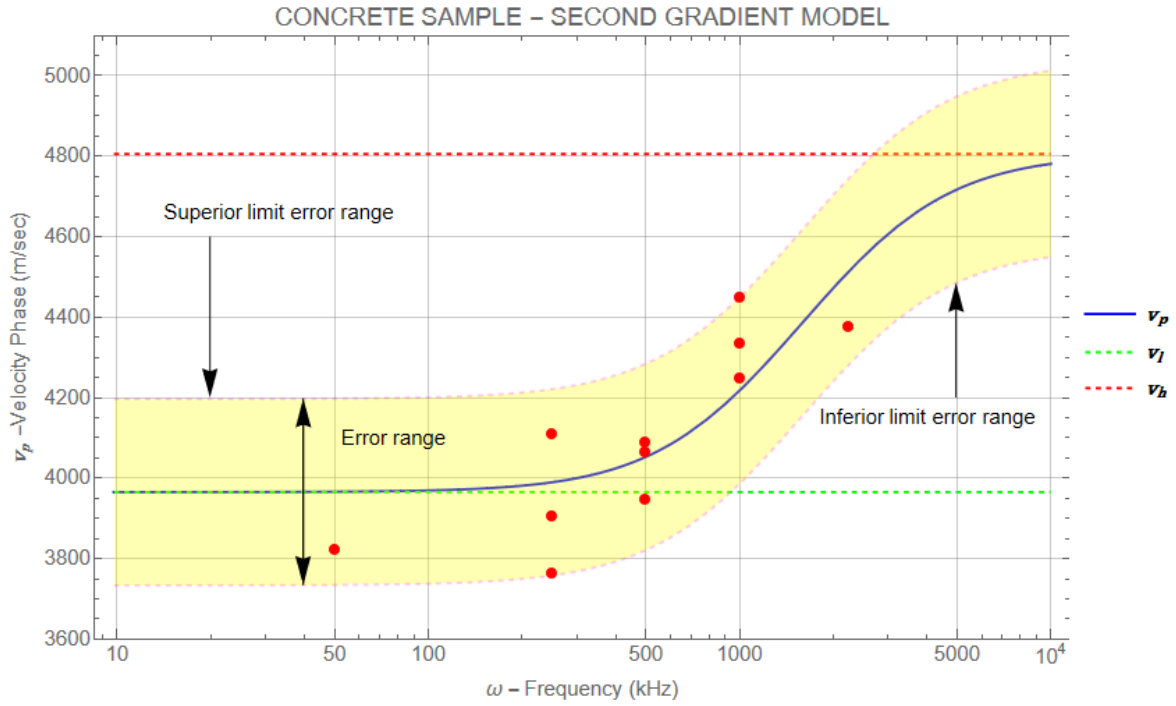

Figure 2.8: *Concrete samples-least squares interpolation (blue line) of experimental data phase velocity (red dots) using equation (2.23). Asymptotic values of the phase velocity for low (dashed green horizontal line) and for the high (dashed red horizontal line) frequency regime are also shown.*

average value of phase velocity at low-high frequency regime and of the characteristic length are respectively: $v_l = 3,750$ m/s, $v_h = 4,469$ m/s, and $L_E = 6.23$ mm. The maximum error on phase velocity is 73.72 m/s, with a small relative error for the low-frequency regime (particularly relevant for the calculation of the longitudinal elastic modulus); indeed, the relative error is about 2%. Examining Figure 2.8 and Figure 2.9 it is possible to see that experimental data (red dots) are close to the graph (blue line) of the interpolating function: this means a low value of the generating function $g(v_l, v_h, L_E)$. The interpolation of the phase velocity function depicted in these figures shows that the elastic strain gradient model can effectively describe the dispersivity of ultrasonic waves experimentally observed. Therefore, it is possible to distinguish a low and a high frequency regime, respectively, characterized by the asymptotic values of the phase velocities v_l and v_h (actually, data in Figure 2.9 do not cover the high frequency regime). Finally, the above cited figures allow for distinguishing a range frequency transition directly correlated to the characteristic length L_E. In particular, we have a transition range between 100 and 5000 kHz for concrete and between 500 and 10000 kHz for sandstone. The higher frequencies characterizing the sandstone transition range with respect to that of concrete can be explained because of the lower characteristic length of sandstone. The recalled values of the characteristic length, obtained interpolating experimental data, appear consistent also from the physical point of view, since the mechanical properties of concrete are mainly influenced by its aggregate properties, yielding to a microstructure dimension quite larger than that of the sandstone. On the other hand, the presence of carbonate clasts in concrete motivates higher wave velocity property with respect to sandstone.
Furthermore, it is worth noting that the yellow band shown in Figure 2.8 and Figure 2.9 represents the error range associated with the interpolation of the dispersion curve. Inaccuracies

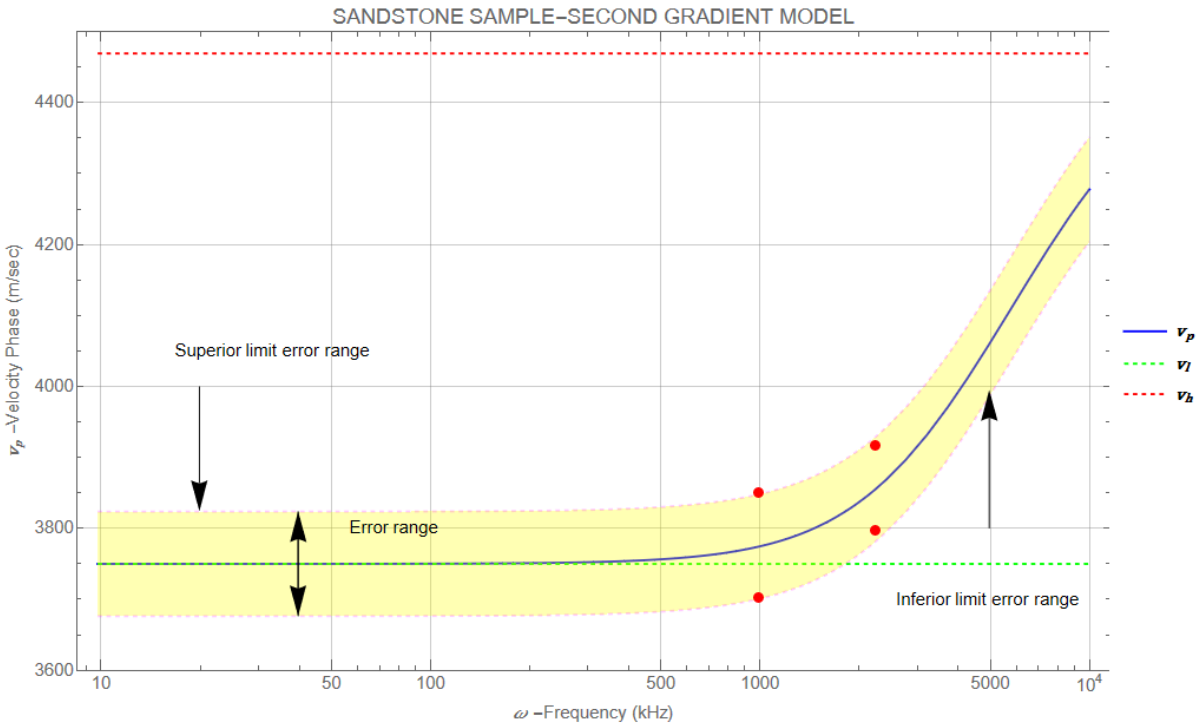

Figure 2.9: *Sandstone samples - least squares interpolation (blue line) of experimental data phase velocity (red dots) using equation (2.23). Asympthotic values of the phase velocity for low (dashed green horizontal line) and for the high (dashed red horizontal line, which is nevertheless not oncluded in the experimental range) frequency regime are also shown*

are due to experimental errors, as discussed in subsection 2.3.1, but also to some limits of the considered one-dimensional model: indeed, three-dimensional effects of wave propagation are neglected.

Despite this, since we have observed an error on the linear elasticity velocity v_l lesser than 6% for the concrete sample and 2% for the sandstone, generally the described results confirm the representativity of the proposed model for describing the ultrasonic response of dispersive materials in the high frequencies range, and this is useful especially for interpreting laboratory test results. On the contrary, if the classical (first gradient) linear elastodynamic theory is employed for evaluating the longitudinal elastic modulus starting from wave velocity measurements at high frequency range, wrong determinations will be made. From the physical point of view, this happens because classical first gradient theory neglects the microstructure influence, despite in the high frequency regime the wavelengths are very small, and thus comparable with the dimensions of the microstructure of the material. In on-site tests on geotechnical materials, where low-frequency waves are employed, wavelengths are bigger than the microstructure, and therefore waves by–pass it: no interactions influence in this case wave phase velocity, which can be predicted with the classical theory. In laboratory tests, for making ultrasonic tests at the same frequencies adopted for on-site tests, extremely large specimens and powerful probes have to be employed, and this makes such an approach not practically feasible and economically sustainable.

Therefore, as observed above, the use for laboratory measurements at high frequencies of the classical expression (2.17) relating the phase velocity to the elastic properties, would lead to the conclusion that the elastic modulus, that in principle is a physical property, would depend on the frequency adopted for the experiment. This result is not physically plausible for the simple fact that in a general engineering problem the material is exposed to many frequencies and its stiffness is only one. For example, a lower frequency value of the phase velocity $v_l = 3,965\,\mathrm{m/s}$,

as in Figure 2.8, corresponds to a longitudinal elastic modulus of $E = 33.957,85\,\mathrm{N/mm^2}$ (consistent with the value typically expected for a concrete of the class UNI EN206-1:2006 30/37). However, if we apply (2.17) directly to the phase velocity measurement at 1000 kHz (i.e., with a phase velocity equal to $4,448.39\,\mathrm{m/s}$), we would markedly overestimate the elastic modulus of the material with $E = 47,491.62\,\mathrm{N/mm^2}$. The latter observation underlines the relevance of establishing a more accurate theoretical framework for the interpretation of ultrasonic velocity data in terms of construction materials elastic moduli; otherwise–as for example by employing the classical first gradient linear elasticity model-large errors can occur. One promising solution, as we have seen above, can be that of taking into account second gradient contributions, i.e., the influence of the microstructure.

2.3.4 Wave form solution for elastic solids with damping –validation and results interpretation

With an approach similar to that adopted in the previous section, here we refer to the viscoelastic model for interpreting the dispersion of experimental ultrasonic phase velocity in elastic solids with damping ($c \neq 0, c_1 = 0$), for which the expression of the phase velocity is given by equation (2.49). As for the previous models, for reconstructing the phase velocity function we applied the least squares interpolation approach by minimizing the function

$$g(c) = \sum_{i=1}^{n} \left[v_{pi} - f(k_1, \rho, c, \omega_i)\right]^2, \tag{2.74}$$

i.e., by determining the parameters c, k_1 that minimize the overall approximation error between theoretical previsions and experimental data (ω_i, v_{pi}) from Table 2.1 (more precisely the average phase velocities v_{pi} at each frequency ω_i, with $i = 1, n$).
For the concrete sample, we show in Figure 2.10 with the blue line the phase velocity evaluated through the damping model and the experimental points (red dots); moreover, the range of the experimental error is indicated. Here, the average value of the phase velocity at low frequency regime is $v_l = 4,137$ m/s, the maximum error on phase velocity is 358.07 m/s, and the relative error for low frequency regime (particularly relevant for the calculation of the longitudinal elastic modulus) is about 8.7%.
A similar investigation has been done for the sandstone sample in Figure 2.11, where we show the interpolating phase velocity function, according to equation (2.49), the experimental points (red dots), and the range of the experimental error. In this case, the average value of the phase velocity at low frequency regime is $v_l = 3,872$ m/s, the maximum error on phase velocity is 73.72 m/s, and the relative error for low frequency regime (particularly relevant for the calculation of the longitudinal elastic modulus) is about 1.90%.
Comparing the results obtained with the second gradient model to those obtained by the damping model, we observe that the low-frequency regime phase velocity values determined by the interpolation are approximately of the same magnitude (on the concrete sample, the deviation between the results, calculated as the ratio of the difference between the two velocities and the smallest one, is 4.3%, while for the sandstone material, it is 3.2%).

2.3.5 Kelvin–Voigt viscous material – model validation and results interpretation

With an approach similarly to that adopted in the previous section, here we refer to the viscoelastic model for interpreting the dispersion of experimental ultrasonic phase velocity data in the case of Kelvin-Voigt material ($c = 0, c_1 \neq 0$) from Section 2.2.3, for which the expression of the phase velocity is given by (2.67). For reconstructing the phase velocity function we applied

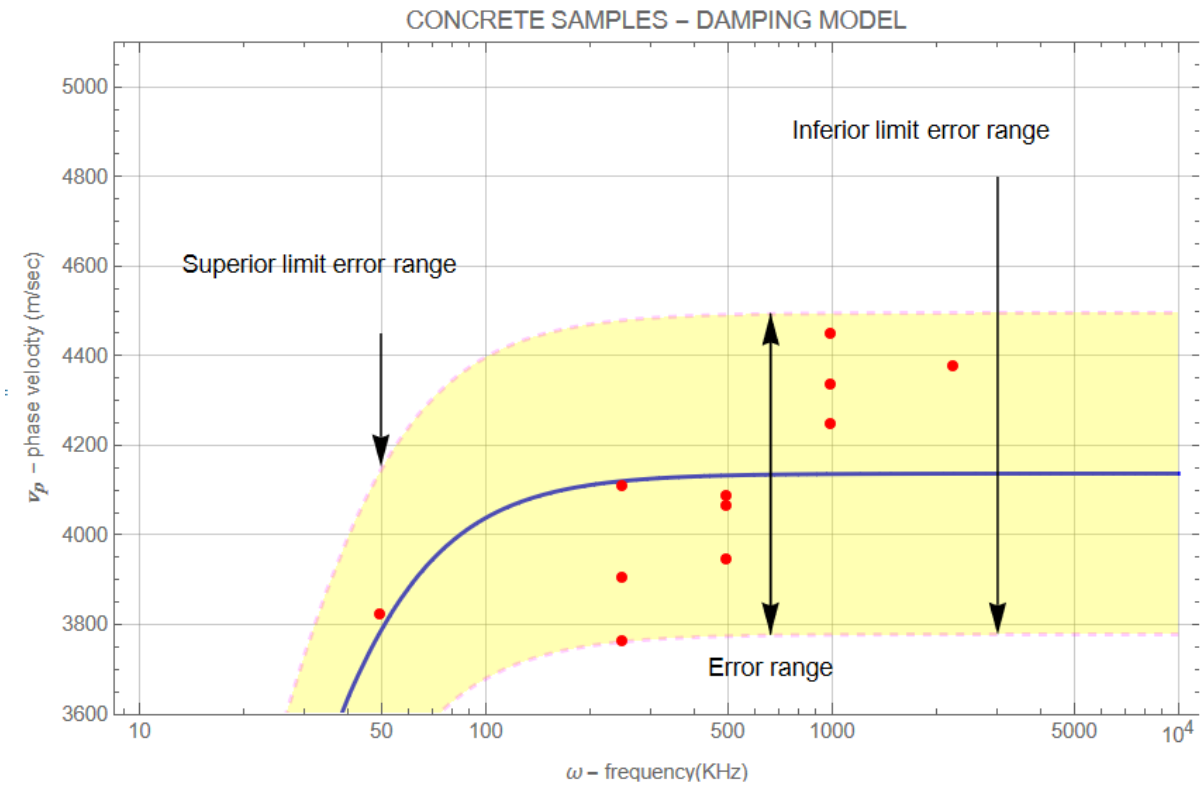

Figure 2.10: *Concrete samples: least squares interpolation (blue line) of experimental data phase velocity (red dots) using equation (2.49)*

the least squares interpolation approach by minimizing the function

$$g(c_1) = \sum_{i=1}^{n} \left[v_{pi} - f(k_1, \rho, c_1, \omega_i) \right]^2 , \tag{2.75}$$

i.e., by determining the parameters c_1, k_1 that minimize the overall approximation error between theoretical previsions and experimental data (ω_i, v_{pi}) from Table 2.1 (more precisely the average phase velocities v_{pi} at each frequency ω_i, with $i = 1, n$).
For the concrete sample, we show in Figure 2.12 with the blue line the phase velocity evaluated through the Kelvin-Voigt visco-elastic model and the experimental points (red dots); moreover, the range of the experimental error is indicated. Here, the average value of the phase velocity at low frequency regime is $v_l = 3,997$ m/s, the maximum error on phase velocity is 311.02 m/s, and the relative error for low frequency regime (particularly relevant for the calculation of the longitudinal elastic modulus) is about 7.8%.
A similar investigation has been done for the sandstone sample in Figure 2.13, where we show the interpolating phase velocity function, according to equation (2.67), the experimental points (red dots), and the range of the experimental error. In this case, the average value of the phase velocity at low frequency regime is $v_l = 3,753$ m/s, the maximum error on phase velocity is 73.72 m/s, and the relative error for low frequency regime (particularly relevant for the calculation of the longitudinal elastic modulus) is about 1.96%. For the frequency range experimentally explored, also the Kelvin-Voigt visco-elastic model reveals to be capable of interpreting experimental data at high frequencies range, since the latter are very close to the graph of the function interpolating the phase velocity theoretical predictions. Moreover, we can notice a limited error range (the yellow area), that can be due both to experimental errors and to limitations of the theoretical model: indeed, more than 3D effects, now we are not considering the influence of microstructure on dispersion, as for second gradient models. As a matter of fact, a second-order

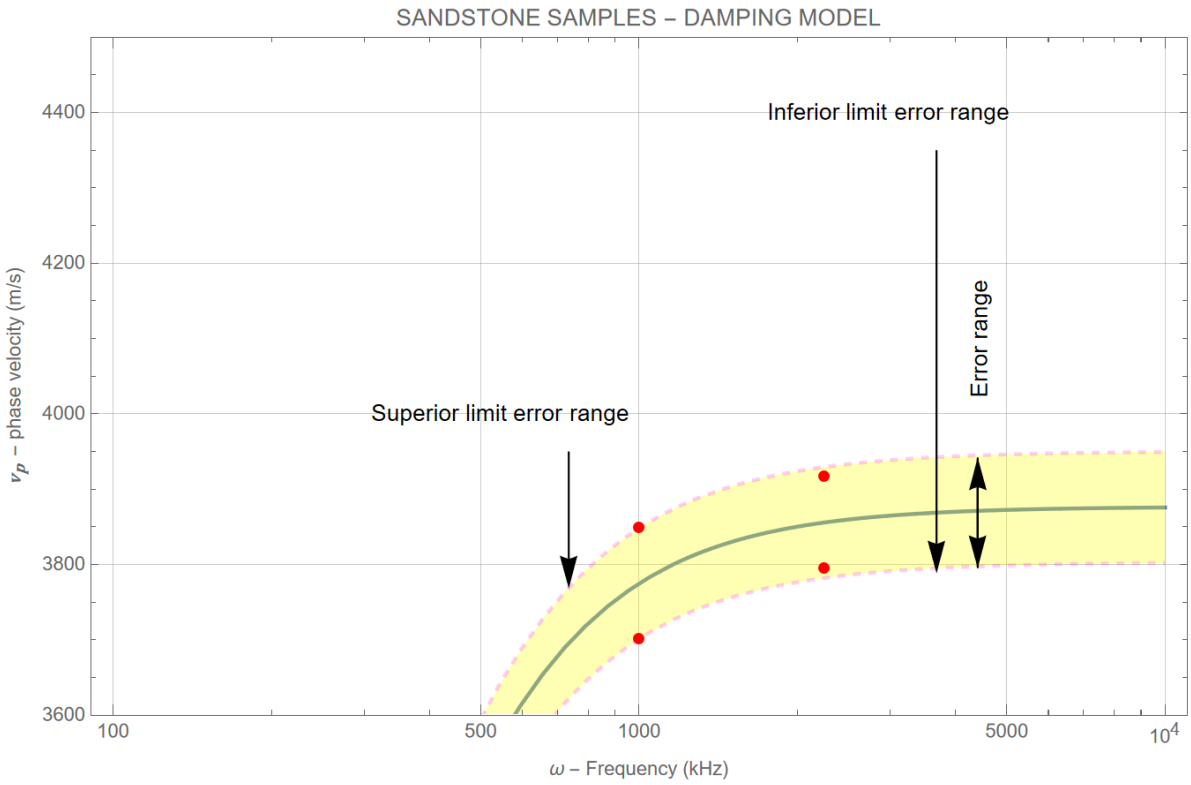

Figure 2.11: *Sandstone sample: least squares interpolation (blue line) of experimental data phase velocity (red dots) using equation (2.49).*

gradient model taking into account also dissipative effects would yield more accurate results: this will be the subject of future research.
Comparing the results obtained with the second gradient model to those obtained by the Kelvin-Voigt visco-elastic model, we observe that the low-frequency regime phase velocity values determined by the interpolation are approximately of the same magnitude (on the concrete sample, the deviation, calculated as the ratio of the difference between the two velocities and the smallest one, is 0.8%, while for the sandstone material, it is 0.1%).

2.4 Summary and discussion of the results

2.4.1 Phase velocity

In the Tables below 2.3 and 2.4, we summarize the results of the experiments in terms of standard velocity values (that is related, as known, directly to the material stiffness k_1) and the corresponding maximum error calculated as the ratio of absolute error over standard velocity. It is observed that, in general, the margin of error for the results obtained with concrete (average 7.43%) is greater than that for sandstone (average 1.93%), which is not surprising considering that concrete is extremely heterogeneous compared to the fine-grained sandstone. Furthermore, the errors observed, in the evaluation of the standard velocity, for the various samples are below 10%, thus well within the safety factors used in the design to evaluate material strength and, consequently, acceptable.
Comparing the velocity phase curves obtained by least squares interpolation of the experimental data for the three models studied in this research for concrete samples, respectively sandstone samples, we can observe that the results from the second gradient and Kelvin-Voigt material models are closer to each other than those from the model with damping material. In this regard, it should be mentioned that in the Kelvin-Voigt and second gradient material models,

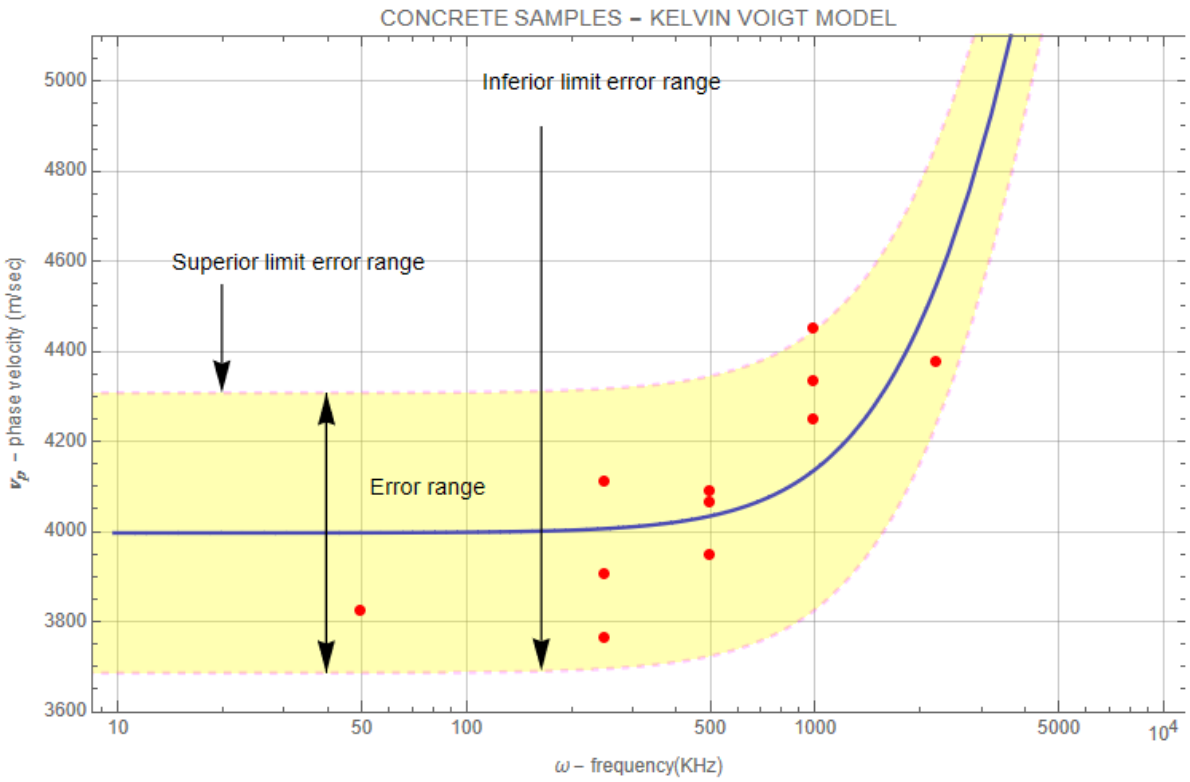

Figure 2.12: *Concrete samples: least squares interpolation (blue line) of experimental data phase velocity (red dots) using equation (2.67).*

the standard velocity is reached at low frequencies, meanwhile in the model with damping material at high frequencies, where the iteration material structure and wave evidently radically changes. However, the standard velocity value for the damping material model falls within the error range of the standard velocity of the second gradient material model. Moreover, in the comparison between second gradient and Kelvin-Voigt material model, we can observe that in both cases the velocity phase dispersion starts around 200 kHz for concrete samples / 500 kHz for sandstone samples, although, in the absence of microstructure, at high frequencies the two models, as expected, diverge: the Kelvin-Voigt material tends towards infinity, while the second gradient material model tends to the value for the high frequency regime. In any case, to rule out one of the two models with dissipation, it would be necessary to investigate a broader range of frequencies and, above all, measure the attenuation of wave amplitudes using advanced methodologies (such as immersion testing). These approaches could reduce measurement errors and enable a more accurate assessment of the contribution of each of the two dissipation coefficients discussed in Sections 2.1 and 2.2, an aspect that will be addressed in the future developments of this research. For this reason, at the current stage of this study, we have presented both models.

2.4.2 Characterization of the material constitutive parameters

In Tables 2.5 and 2.6 we summarize the results of the experiments in terms of second gradient and viscous parameters. We have also reported the values of material stiffness, calculated using equation 2.21, once we know the characteristic length L_E.
The results regarding the internal material viscosity c_1 confirm, as is generally recognized, that concrete is more viscous than sandstone. The microstructure parameter k_2 of concrete is approximately 10 times that of sandstone, which aligns with the considerations regarding the clast dimensions of the two materials, as discussed in subsection 2.3.1.

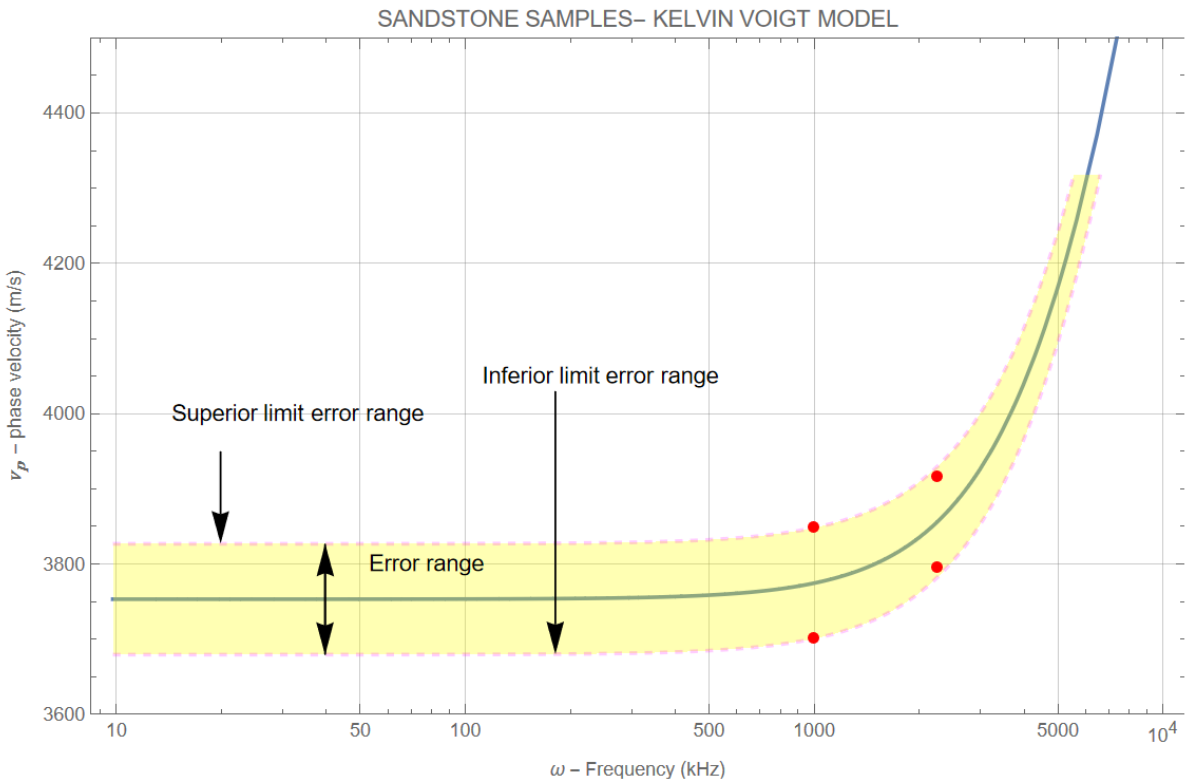

Figure 2.13: *Sandstone sample: least squares interpolation (blue line) of experimental data phase velocity (red dots) using equation 2.67.*

Concrete	v_l [m/s]	Absolute error [m/s]	% Error [%]
Second gradient model	3,965.0	232.0	5.8
Viscous solid with damping model	4,137.0	359.0	8.7
Kelvin-Voigt viscous model	3,996.0	311.0	7.8

Table 2.3: *Comparison of standard velocity, absolute error, and percentage error for models applied to concrete samples.*

Sandstone	v_l [m/s]	Absolute error [m/s]	% Error [%]
Second gradient model	3,751.0	74.0	2.0
Viscous solid with damping model	3,872.0	74.0	1.9
Kelvin-Voigt viscous model	3,864.0	74.0	1.9

Table 2.4: *Comparison of standard velocity, absolute error, and percentage error for models applied to sandstone samples.*

As for the phase velocities, since the proportionality between v_p and k_1, the deviations between the standard material elastic moduli calculated with the three models do not exceed 10%, making the results acceptable. We underline that the obtained moduli are consistent with

Concrete Model	L_E [mm]	k_2 [kg m^{-1} s^{-1}]	η [kg m^{-1}]	c [kg m^{-1} s^{-1}]	c_1 [N s m^{-2}]	k_1 [kg m^{-1} s^{-2}]
Second gradient model	20	1.53×10^7	0.66	-	-	3.77×10^{10}
Viscous solid with damping model	-	-	-	9.89×10^6	-	4.11×10^{10}
Kelvin-Voigt viscous model	-	-	-	-	1.33×10^5	3.83×10^{10}

Table 2.5: *Second gradient and viscous parameters for concrete samples.*

Sandstone Model	L_E [mm]	k_2 [kg m^{-1} s^{-1}]	η [kg m^{-1}]	c [kg m^{-1} s^{-1}]	c_1 [N s m^{-2}]	k_1 [kg m^{-1} s^{-2}]
Second gradient model	6.23	1.38×10^6	0.07	-	-	3.58×10^{10}
Viscous solid with damping model	-	-	-	1.10×10^8	-	3.82×10^{10}
Kelvin-Voigt viscous model	-	-	-	-	4.85×10^4	3.58×10^{10}

Table 2.6: *Second gradient and viscous parameters for sandstone samples.*

laboratory practice, as previously highlighted for C30/37 concrete in subsection 2.3.3, and can also be found in the literature, as in the case of sandstone, even if there are some minor differences between the results of the three model. The engineering outcome will depend on the adopted model and the chosen data interpretation.

3 Analysis of ultrasonic wave dispersion in the presence of attenuation and second-gradient effects

3.1 Preliminary definitions

In Section 2, we have focused our attention on dispersive aspects and on how the second-gradient and viscosity parameters of the material can influence this phenomenon. We now intend, first of all, to investigate what happens when, as in real experimental conditions, both effects, second-gradient behavior and viscosity, simultaneously act on wave propagation, and to distinguish attenuation phenomena from dispersion phenomena. A clear definition of these two concepts is therefore required. Dispersion refers to the phenomenon in which the speed of a wave depends on its frequency. As seen in Section 2, it depends on scattering phenomena, the refraction and reflection of the wave within the material, when the wavelength is comparable to the microstructure material, i.e. the grain size.
Attenuation refers to the decrease of amplitude that occurs when a wave propagates through a medium. In the traditional wave theory, attenuation is typically associated with damping mechanisms, such as viscoelastic effects or material imperfections. However, in materials exhibiting second-gradient behavior, attenuation can arise due to the nonlocal interactions and microstructural features that influence wave propagation. As ultrasonic waves pass through a material with second-gradient effects, their energy is dispersed in a way that cannot be fully explained by classical damping models. The attenuation in such materials is also frequency-dependent, with the energy dispersion being more significant at higher frequencies. We would like to highlight a recent contribution that has significantly inspired our work, specifically the thesis by Ronny Hofmann[87]. His study focuses on laboratory measurements of clastic rocks, ranging from 3 Hz to 500 kHz, and their application to well log analysis and a time-lapse study in the North Sea. Within this framework, the measurements reveal substantial dispersion in sandstones due to the saturation of inhomogeneities and open boundaries (such as pore pressure diffusion), which in turn affects the material's compressibility and stiffness.
Furthermore, attenuation is directly related to the rate of change of the modulus. This concept is summarized in Figure 3.1, which illustrates that as the parameter μ (defined in Hofmann's thesis as a distribution parameter that gives the range over which a relaxation mechanism operates) changes, i.e., from 0.8 to 0.2, the dispersion of phase velocities is higher as in Fig.3.1a and the attenuation peaks in Fig.3.1b become more pronounced. Figure 3.1c summarizes the content presented in Figures 3.1a and 3.1b, which are taken from Hofmann's thesis, then illustrates how the phase velocity varies as a function of frequency ω, and how this variation is closely associated with attenuation behavior, both influenced by the parameter μ. The blue curve represents the frequency-dependent phase velocity v_{p1}, which exhibits dispersion-meaning that the phase velocity increases with frequency. This increase is particularly evident around the frequency where attenuation reaches its maximum. The black curve shows the attenuation trend, which peaks at a specific frequency marked by the vertical dashed magenta line. At this point, the energy loss within the material is at its highest due to internal viscosity. The green line indicates the reference phase velocity v_l at low frequencies, representing the asymptotic limit as frequency approaches zero. Conversely, the red line corresponds to the high-frequency limit v_h, where dispersion effects diminish and the phase velocity stabilizes. Overall, the figure highlights that the most significant change in phase velocity occurs near the frequency where attenuation peaks.
Since no continuous model currently exists that can capture the aforementioned effect, in this section we will try to provide a model that, starting from the Rayleigh–Hamilton principle and considering both the material's internal viscosity and second-gradient parameters, can simulate the aforementioned dispersive and dissipative effects.

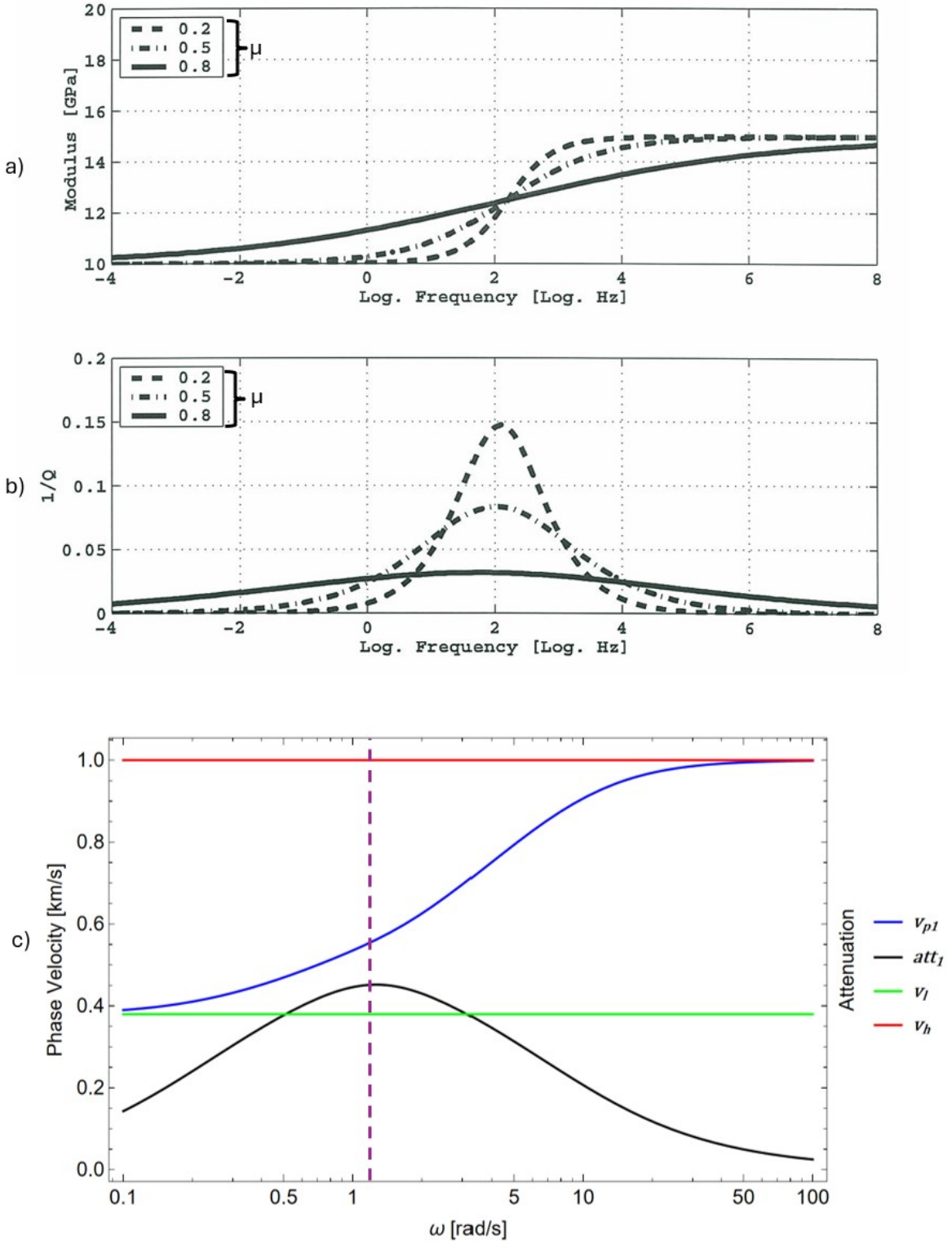

Figure 3.1: *Influence of the material parameter μ, related to the dissipative properties of the medium, as defined in Hofmann's thesis[87], on phase velocity (a) and attenuation (b). The variation of phase velocity as a function of frequency is shown in (c), where a significant change occurs near the attenuation peak*

.

3.2 Modeling and methods

3.2.1 Scope and strategy

We are searching for a model that can reproduce the variation of phase velocity and attenuation with wave frequency for a given material, as shown in Figure 1c, which is our benchmark. In this context, we will consider the Rayleigh–Hamilton principle, using second-gradient and viscous parameters to describe the displacement involved in the energies represented in the principle. The Partial Differential Equation (PDE) obtained will be solved using a wave-form solution to derive the dispersion equation that includes phase velocity and attenuation.

3.2.2 Variational formulation

We begin by recalling the extended Rayleigh–Hamilton principle, which postulates that the variation of the action, δA, is connected to the Rayleigh function R

$$\delta A = \int_{t_0}^{t_1} \left\{ \int_0^L \left(\delta K - \delta W^{\text{int}} \right) dx + \delta W^{\text{ext}} \right\} dt = \int_{t_0}^{t_1} \left(\frac{\delta R}{\delta \dot{u}'} \delta u' + \frac{\delta R}{\delta \dot{u}''} \delta u'' \right) dt, \tag{3.1}$$

where the three energy functions K, the kinetic energy density, W, the potential energy density, W^{int}, the internal energy per unit volume, and W^{ext}, the external energy function, are defined as

$$K = \int_0^L \left(\frac{1}{2} \rho \dot{u}^2 + \frac{1}{2} \eta \dot{u'}^2 \right) dx, \tag{3.2}$$

$$W^{\text{int}} = \int_0^L \left(\frac{1}{2} k_1 u'^2 + \frac{1}{2} k_2 u''^2 \right) dx, \tag{3.3}$$

$$W^{\text{ext}} = \left[F_0^{\text{ext}} u + B_0^{\text{ext}} u' \right]_{x=0} + \left[F_L^{\text{ext}} u + B_L^{\text{ext}} u' \right]_{x=L} + \int_0^L \left(b_n u + b_d u' \right) dx, \tag{3.4}$$

and the Rayleigh function is equal to

$$R = \int_0^L \left(\frac{1}{2} c_1 \dot{u}'^2 + \frac{1}{2} c_2 \dot{u}''^2 \right) dx \tag{3.5}$$

We recall that k_1 and k_2 are the standard elastic modulus for a linear one-dimensional elastic body and the non-standard strain-gradient modulus, respectively. Given the displacement u, its derivatives with respect to time are denoted by $\dot{u}$, and with respect to space by u' (first derivative) or u'' (second derivative); ρ and η are the mass density (mass per unit length) and the micro-inertia of the one-dimensional body, respectively. b_n and b_d are the external distributed (per unit length) forces and double forces, respectively. F_0^{ext} (or F_L^{ext}) and B_0^{ext} (or B_L^{ext}) are the concentrated forces and double forces evaluated at the extrema $x = 0$ (or $x = L$) of the one-dimensional body, respectively.
Meanwhile, in the Rayleigh function, two internal viscosities are present: c_1, related to the first gradient field, and c_2, related to the second gradient field.
Replacing equations (3.2), (3.3), (3.4), and (3.5) in the left side of equation (3.1) and integrating by parts, for every admissible variation of the displacement field, the variation of the action, δA, can be reduced to

$$\delta A = \int_{t_0}^{t_1} \left\{ \int_0^L \left[\delta u \left(-\rho \ddot{u} + k_1 u'' + \eta \ddot{u}'' - k_2 u^{(4)} + b_n - b_d' \right) \right] dx \right\}$$
$$- \int_{t_0}^{t_1} \delta u(x=0) \left[-\eta \ddot{u}'(x=0) - k_1 u'(x=0) + k_2 u'''(x=0) + b_d \right] dt$$
$$+ \int_{t_0}^{t_1} \delta u(x=L) \left[-\eta \ddot{u}'(x=L) - k_1 u'(x=L) + k_2 u'''(x=L) + b_d \right] dt$$
$$- \int_{t_0}^{t_1} \delta u'(x=0) \left[-k_2 u''(x=0) \right] dt$$
$$+ \int_{t_0}^{t_1} \delta u'(x=L) \left[-k_2 u''(x=L) \right] dt. \tag{3.6}$$

The variation of the Rayleigh function is:

$$\int_{t_0}^{t_1} \left(\frac{\delta R}{\delta \dot{u}'} \delta u' + \frac{\delta R}{\delta \dot{u}''} \delta u'' \right) dt = \int_0^t \int_0^L \left(c_1 \dot{u}' \delta u' + c_2 \dot{u}'' \delta u'' \right) dx\, dt, \tag{3.7}$$

which, after integrating by parts in space and time, becomes:

$$\int_{t_0}^{t_1} \left(\frac{\delta R}{\delta \dot{u}'} \delta u' + \frac{\delta R}{\delta \dot{u}''} \delta u'' \right) dt = \int_{t_0}^{t_1} \left[c_1 \dot{u}' \delta u \right]_0^L dt - \int_{t_0}^{t_1} \int_0^L c_1 \dot{u}'' \delta u\, dx\, dt$$
$$+ \int_{t_0}^{t_1} \left[c_2 \dot{u}'' \delta u' \right]_0^L dt - \int_{t_0}^{t_1} \left[c_2 \dot{u}''' \delta u \right]_0^L dt$$
$$+ \int_{t_0}^{t_1} \int_0^L c_2 \dot{u}^{(4)} \delta u\, dx\, dt. \tag{3.8}$$

Then, replacing equations (3.6) and (3.8) into equation (3.1) and rearranging, we obtain:

$$\delta A = \int_{t_0}^{t_1} \left\{ \int_0^L \left[\delta u \left(-\rho \ddot{u} + k_1 u'' + \eta \ddot{u}'' - k_2 u^{(4)} + b_n - b_d' + c_1 \dot{u}'' - c_2 \dot{u}^{(4)} \right) \right] dx \right\} dt$$
$$- \int_{t_0}^{t_1} \delta u(x=0) \left[-\eta \ddot{u}'(x=0) - k_1 u'(x=0) + k_2 u'''(x=0) + b_d \right.$$
$$\left. - c_1 \dot{u}'(x=0) + c_2 \dot{u}'''(x=0) \right] dt$$
$$+ \int_{t_0}^{t_1} \delta u(x=L) \left[-\eta \ddot{u}'(x=L) - k_1 u'(x=L) + k_2 u'''(x=L) + b_d \right.$$
$$\left. - c_1 \dot{u}'(x=L) + c_2 \dot{u}'''(x=L) \right] dt$$
$$- \int_{t_0}^{t_1} \delta u'(x=0) \left[-k_2 u''(x=0) - c_2 \dot{u}''(x=0) \right] dt$$
$$+ \int_{t_0}^{t_1} \delta u'(x=L) \left[-k_2 u''(x=L) - c_2 \dot{u}''(x=L) \right] dt = 0. \tag{3.9}$$

where, since the displacement $u(x,t)$ is assumed to be prescribed both at $t = t_0$ and at $t = t_1$, we have that $\delta u(x, t = t_0) = \delta u(x, t = t_1) = 0$. Equation (3.9) must hold for every admissible variation δu of the displacement field u. Therefore, the last four terms of equation (3.9) must be null. On one hand, if the displacement u or the displacement gradient u' are prescribed at the boundary (i.e., the left-hand sides of the following equations are satisfied), then their variation is null, as well as the corresponding terms in equation (3.9). On the other hand, if these kinematic conditions are not prescribed, then the right-hand sides of the following equations must be satisfied to make the same terms of equation (3.9) null:

$$
\begin{aligned}
&u(0,t) = u_0(t) \\
&\text{or} \quad -\eta\ddot{u}'(x=0,t) - k_1 u'(x=0,t) + k_2 u'''(x=0,t) + b_d \\
&\qquad - c_1\dot{u}'(x=0,t) + c_2\dot{u}'''(x=0,t) = F_0^{\text{ext}},
\end{aligned} \tag{3.10}
$$

$$
\begin{aligned}
&u(L,t) = u_L(t) \\
&\text{or} \quad -\eta\ddot{u}'(x=L,t) - k_1 u'(x=L,t) + k_2 u'''(x=L,t) + b_d \\
&\qquad - c_1\dot{u}'(x=L,t) + c_2\dot{u}'''(x=L,t) = -F_L^{\text{ext}},
\end{aligned} \tag{3.11}
$$

$$
u'(0,t) = b_0(t) \qquad \text{or} \quad -k_2 u''(x=0,t) - c_2\dot{u}''(x=0,t) \;= B_0^{\text{ext}}(t), \tag{3.12}
$$

$$
u'(L,t) = b_L(t) \qquad \text{or} \quad -k_2 u''(x=L,t) - c_2\dot{u}''(x=L,t) \;= -B_L^{\text{ext}}(t). \tag{3.13}
$$

for every instant of time, e.g., $\forall t \in \mathbb{R}$. Finally, also the first line of equation (3.9) must be zero for every admissible variation δu of the displacement field. Thus, because of its arbitrariness, it follows that

$$
-\rho\ddot{u} + k_1 u'' + \eta\ddot{u}'' - k_2 u^{(4)} - b_d' + b_n + c_1\dot{u}'' - c_2\dot{u}^{(4)} = 0, \quad \forall x \in [0,L], \quad \forall t \in \mathbb{R}. \tag{3.14}
$$

3.2.3 Wave form solution

Equation (3.14) is the Partial Differential Equation (PDE) governing the evolution of the displacement field $u(x,t)$ for the investigated model, which will be solved in the following two subsections. In particular, we look for a wave-form solution to equation (3.14), and we assume the body length L to be sufficiently large so that the boundary conditions (BCs) (3.10)-(3.13) do not influence the solution.
Equation (3.14) can be solved by considering no external distributed actions ($b_n = 0$ and $b_d = 0$), in the form of the following plane wave solution for the displacement field

$$
u(x,t) = \text{Re}\left(u_0 e^{i(\omega t - k_\omega x)}\right), \tag{3.15}
$$

where u_0 is the complex wave amplitude, ω is the frequency of the wave expressed in rad/s, k_ω is the complex wave number, i is the imaginary unit, and Re is the real part operator. Calculating the derivatives of equation (3.15) and replacing them into equation (3.14), it results

$$
(k_2 + ic_2\omega)k_\omega^4 + (k_1 + ic_1\omega - \eta\omega^2)k_\omega^2 - \rho\omega^2 = 0, \tag{3.16}
$$

where the arbitrariness of the complex wave amplitude u_0 has been considered. Equation (3.16) is a fourth-degree algebraic equation in terms of k_ω, and therefore admits four complex solutions for k_ω. However, in equation (3.16), k_ω appears only with even powers (k_ω^2 or k_ω^4). Thus, if $k_\omega = \hat{k}_\omega$ is a solution of equation (3.16), then also $k_\omega = -\hat{k}_\omega$ is a solution. As a consequence, two of these solutions correspond to right-hand propagating waves, while the other two are equal in magnitude and opposite in sign. The reason is the isotropy of the domain. In the formulae, two independent solutions are

$$
k_{\omega_{1,2}} = \sqrt{\frac{-(k_1 + ic_1\omega - \eta\omega^2) \pm \sqrt{(k_1 + ic_1\omega - \eta\omega^2)^2 + 4(k_2 + ic_2\omega)(\rho\omega^2)}}{2(k_2 + ic_2\omega)}}. \tag{3.17}
$$

Remembering the correlation between frequency ω, wave number k_ω, and phase velocity v_p, we obtain an expression for the two phase velocities

$$v_{p_{1,2}} = \mathrm{Re}\left(\frac{\omega}{k_{\omega_{1,2}}}\right) = \\ = \mathrm{Re}\left(\sqrt{\frac{2(k_2 + ic_2\omega)\omega^2}{-(k_1 + ic_1\omega - \eta\omega^2) \pm \sqrt{(k_1 + ic_1\omega - \eta\omega^2)^2 + 4(k_2 + ic_2\omega)(\rho\omega^2)}}}\right). \quad (3.18)$$

Similarly, starting from the wave number k_ω, it is possible to determine the corresponding two quality factors Q_1 and Q_2 as the inverse of the damping ratio ζ[87], which characterizes the rate of energy loss in the system, expressed as a function of the real and imaginary parts of the wave number

$$\zeta_{1,2} = \frac{1}{Q_{1,2}} = -\frac{\mathrm{Im}(k_{\omega_{1,2}})}{\mathrm{Re}(k_{\omega_{1,2}})}. \quad (3.19)$$

The quality factors can also be understood as the ratio between stored and dissipated energy. The quality factor has two definitions in the literature, which yield approximately the same value when $Q \gg 1$, as is the case for seismic waves. These definitions are given in terms of twice the strain energy and the total energy, respectively, both time-averaged over a cycle[88]. In conclusion, equations (3.18) and (3.19) serve as the reference for our model, linking phase velocity and attenuation to the frequency of the wave propagating through the material. Figure 3.2 presents the results of our theoretical model, based on the constitutive framework and equations introduced in this manuscript (notably equations (3.18) and (3.19)). In summary, Figure 3.1 is qualitative and illustrative, derived from Hofmann's experimental work, whereas Figure 3.2 is quantitative, based on our theoretical development, and directly supports the validation of the proposed model.

3.3 Validation: results and discussion

We want to validate this model with data available for common construction materials in the literature[13;89;90]. Such literature has been selected because, among many available articles, both phase velocity and attenuation measurements have been made for the same material at the same frequencies.
In detail, we investigate a sandstone[89] sample, a cement paste[90] sample, and finally a concrete sample[90]. For each material, we have developed a case study; then, the validation is obtained by superimposing the theoretical predictions (obtained from numerical simulations) with the experimental data.
First, we propose a numerical simulation that allows us to make general considerations about the dispersive behavior of the wave, characteristic of our model. Second, we validate the model using the materials presented above, comparing the available experimental data with the numerical simulation. The material constitutive parameters used in this section are presented in Table 3.1.
Figures 3.2 and 3.3 refer to the numerical simulation toward the benchmark (Figure 3.1), while Figures 3.4, 3.5, and 3.6 refer to the case studies.

3.3.1 Numerical simulation toward the benchmark

Figure 3.2 presents a graphical representation of the two phase velocities (3.18) and their respective attenuations (3.19) computed using the material parameters listed in Table 3.1. When c_1

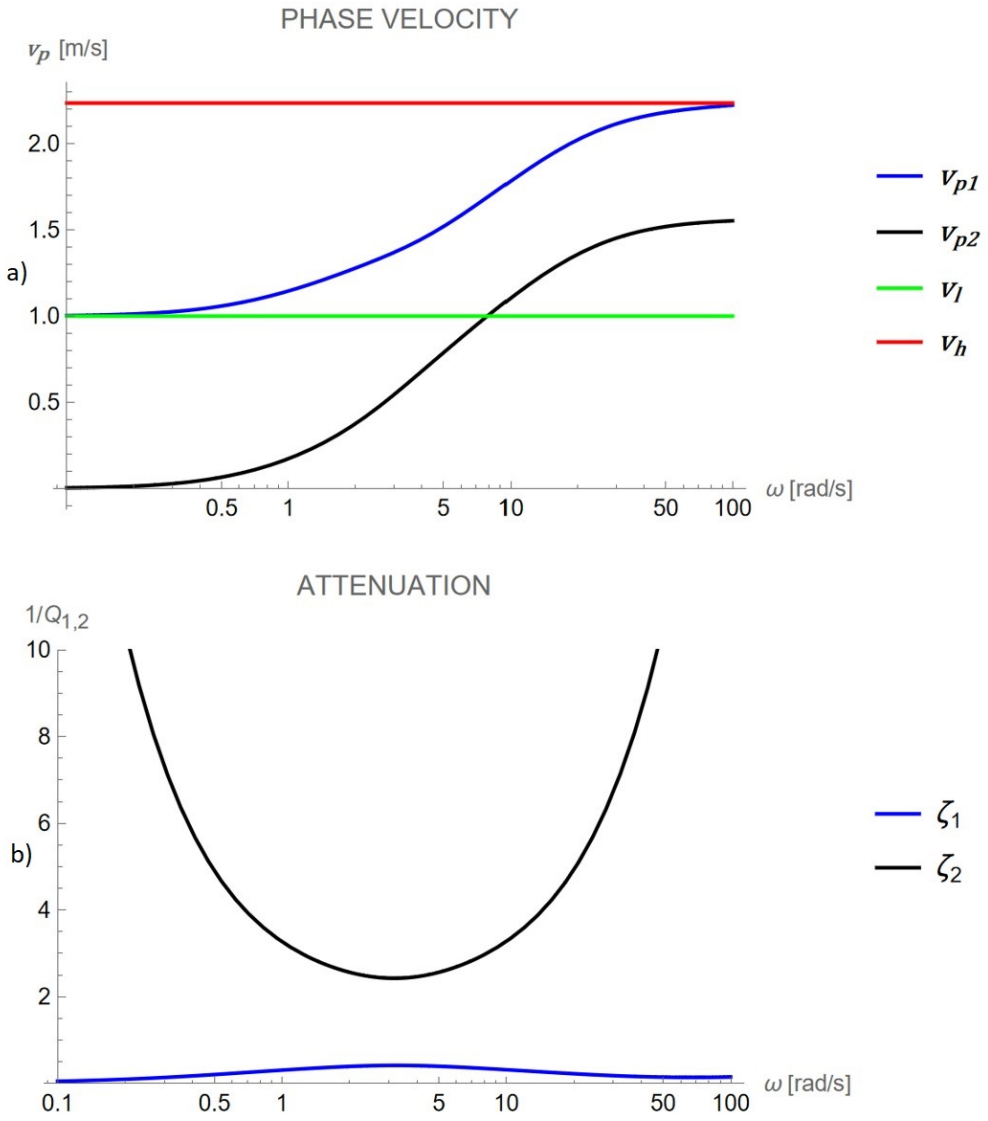

Figure 3.2: *Phase velocity* v_p (m/s) *and damping ratio as functions of the frequency* ω (rad/s) *according to equations (3.18) and (3.19) for a given material with constitutive parameters shown in Table 3.1. The characteristic frequency at which the attenuation peak occurs is* 3.2 rad/s. *The two asymptotes defined by equations (3.20) and (3.21) are also shown.*

Reference	**Figure nr.**	**Constitutive Parameters**					
		k_1	k_2	ρ	η	c_1	c_2
		$[\mathrm{kg\,m^{-1}\,s^{-2}}]$	$[\mathrm{kg\,m\,s^{-2}}]$	$[\mathrm{kg\,m^{-3}}]$	$[\mathrm{kg\,m^{-1}}]$	$[\mathrm{kg\,m^{-1}\,s^{-1}}]$	$[\mathrm{kg\,m\,s^{-1}}]$
benchmark 1	2	1	0.5	1	0.1	1	1×10^{-3}
benchmark 2	3	1	0.5	1	0.1	3	1×10^{-3}
sandstone	4	7.7×10^{9}	0.1×10^{6}	2650	0.04	100	5×10^{-3}
cement paste	5	11.3×10^{9}	1.8×10^{6}	1500	0.253	23.8×10^{3}	1×10^{-3}
concrete	6	37.3×10^{9}	33.5×10^{6}	2450	1.4	300×10^{3}	1×10^{-3}

Table 3.1: *Table of constitutive parameters for different figures.*

and c_2 are set to zero, v_{p2} becomes zero, while v_{p1} asymptotically approaches the low-frequency velocity v_l and the high-frequency velocity v_h, defined as follows

$$\lim_{\omega\to 0}\lim_{c_1\to 0}\lim_{c_2\to 0} v_{p_{1,2}} = v_l = \sqrt{\frac{k_1}{\rho}}, \tag{3.20}$$

$$\lim_{\omega\to \infty}\lim_{c_1\to 0}\lim_{c_2\to 0} v_{p_{1,2}} = v_h = \sqrt{\frac{k_2}{\eta}}, \tag{3.21}$$

For c_1 and c_2 different from zero, Figure 3.2 shows that the wave with phase velocity v_{p2} exhibits significantly higher attenuation than the wave with phase velocity v_{p1}, rendering it experimentally unmeasurable. Moreover, the transition of velocity from low- to high-frequency regimes occurs at a characteristic frequency for both waves, corresponding to the attenuation peak. For certain values of the viscosities c_1 and c_2, as illustrated in Figure 3.3, a jump in the phase velocities v_{p_1} and v_{p_2} is observed at the frequency where the attenuation curves of both signals share a common peak. The jump observed in Fig. 3.3 should not be interpreted as a physical discontinuity. In this regime, the transition between low frequencies and high frequencies is affected by the competition between modes, leading to a numerical/post-processing artifact. From a physical viewpoint, the dispersion behavior is expected to remain continuous. Nevertheless, the phase velocity measurable by ultrasonic instruments will always correspond to the wave with lower attenuation, namely v_{p_1} in the numerical example considered.

3.3.2 Validation with data from the literature

Since experimental attenuation measurements available in the literature are generally expressed as the loss of signal amplitude between one end and the other of the sample along its length L, and are measured in (dB/m), it is useful to introduce an attenuation coefficient α, according to the following formulation[89]

$$\alpha = -\frac{20}{x}\log\left(\frac{u_x}{u_0}\right), \tag{3.22}$$

where u_0 and u_x denote the complex wave amplitudes at the source location and at a generic position x, respectively, along the propagation direction through the medium. Replacing equation (3.15) into equation (3.22), using the Euler properties and considering the real and imaginary parts of the wavenumber, we obtain:

$$\alpha = -20ik_\omega \approx 20\mathrm{Im}(k_\omega), \tag{3.23}$$

where in the wavenumber we can omit the real part since, due to the fact that we use maximum values of amplitude in equation (3.23), the cosine of the wavenumber, corresponding to its real part, assumes values that are certainly lower than those related to the imaginary part. Once the material stiffness parameters, microstructure, micro-inertias, and density are set, the next step is to evaluate how variations in the internal viscosity of the material influence the combination of parameters that best approximate the experimental data for phase velocity and attenuation.

1st case of study: Sandstone The sediment specimen was prepared in a 100 mm x 100 mm x 50 mm container immersed in water to optimize velocity dispersion and minimize ultrasonic pulse attenuation. The experiment took place in a 650 mm x 750 mm x 1,500 mm water bath, using two matched pairs of broadband transducers with center frequencies of 0.5 MHz and 1.0 MHz[89]. The transducers were aligned coaxially with a 150 mm separation, mounted on a stable frame to ensure accurate wave amplitude measurements and prevent pressure variations on the probes.

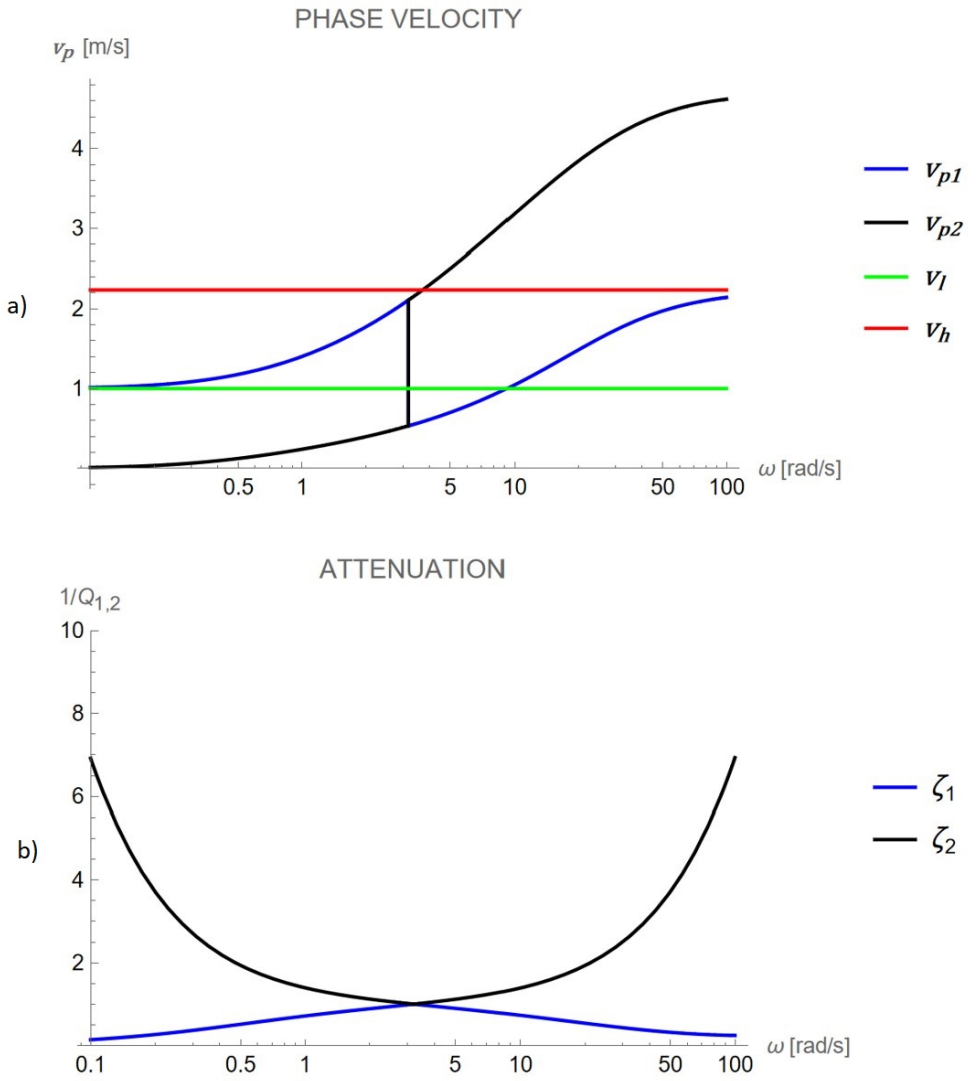

Figure 3.3: *Phase velocity v_p (*m/s*) and damping ratio as functions of the frequency ω (*rad/s*) according to equations (3.18), subfigure a, and (3.19), subfigure b, for a given material with constitutive parameters as shown in Table 3.1. The point at which the velocity jump occurs corresponds to the common peak—respectively maximum and minimum—of the two wave signals. The two asymptotes defined in equations (3.20) and (3.21) are also represented in subfigure a.*

In this case study, we already know the bulk modulus of the material and its density, so the phase velocity for the low-frequency regime is immediately obtained by equation (3.20). The values of microstructure and micro-inertia can be derived by calculating the characteristic length of the material, taking into account that the velocity in the high-frequency regime is lower than that in the low-frequency regime according to experimental data.
In Figure 3.4, we present the overlap between numerical simulation, using the constitutive parameters of Table 3.1, and experimental data for phase velocity and wave attenuation in the tested material. In the frequency range of investigation, no attenuation peak is observed. The monotonic trend observed in both phase velocity (decreasing) and attenuation (increasing) is successfully captured by the numerical simulation, confirming the model's accuracy in describing wave propagation behavior.
Table 3.2 summarizes the theoretical and experimental ultrasonic wave velocities measured in the sandstone sample at frequencies ranging from 300 kHz to 1,000 kHz. To evaluate the ac-

curacy of the theoretical model, the Root Mean Square Error (RMSE) between the theoretical and experimental velocities was calculated. The RMSE value of approximately 19.82 m/s corresponds to 1.21% relative to the average theoretical velocity, indicating very good agreement between theoretical predictions and experimental results.

ω **(kHz)**	**Theo.** v_p **(m/s)**	**Exp.** v_p **(m/s)**	**Theo.** α **(dB/m)**	**Exp.** α **(dB/m)**
300	1,665	1,680	0.13	0.38
400	1,648	1,670	0.29	0.40
500	1,634	1,660	0.53	0.42
600	1,623	1,650	0.84	0.59
700	1,614	1,638	1.23	0.80
800	1,608	1,625	1.68	1.20
900	1,604	1,610	2.21	2.10
1,000	1,600	1,590	2.80	3.05

Table 3.2: *Ultrasonic wave velocities and attenuation for sandstone sample: comparison between theoretical (Theo.) and experimental (Exp.) values.*

2nd case of study: Cement paste The specimens tested were cubic with 150 mm edge. The experimental setup uses a simple through-transmission ultrasonic configuration, employing a waveform generator board and two broadband transducers with frequencies between 100 kHz and 1 MHz, along with a data acquisition system[90]. We consider the data for a sample with water/cement ratio = 0.375.
In Figure 3.5, we compare experimental data with the numerical simulation of the model. The phase velocity suddenly decreases around 200 kHz, tending towards the high-frequency regime velocity. In the attenuation plot, an increasing trend is observed, although a resonance peak appears at 100 kHz in the experimental data, probably due to effects not captured by the model such as internal micro-fractures with fluid inclusions or measurement errors.
Table 3.3 summarizes the theoretical and experimental ultrasonic wave velocities measured in the cement paste sample for frequencies ranging from 10 kHz to 1,000 kHz. As observed also in the sandstone case, discrepancies between experimental and theoretical results increase slightly at higher frequencies. These discrepancies may arise from frequency-dependent attenuation mechanisms and effects of second gradient parameters (e.g., micro-inertia), which become significant at high frequencies when the wavelength approaches the size of the microstructure. To evaluate the accuracy of the theoretical model, the Root Mean Square Error (RMSE) between the theoretical and experimental velocities was calculated. The RMSE value of approximately 19.10 m/s corresponds to 0.71% relative to the average theoretical velocity, indicating very good agreement between theoretical predictions and experimental results.

3rd case of study: Concrete As for the cement paste, the specimens tested were cubic of 150 mm edge, and the experimental setup was the same of previous case of study. Several different compositions of concrete were manufactured in function of water to cement ratio and of aggregate to cement ratio for a total of 24 specimens. We consider the data for a sample with ratio water/cement=0.375. Also in this case the model confirms the monotonic trend of the experimental data (see Figure 3.6). The Table 3.4 summarizes the theoretical and experimental ultrasonic wave velocities measured in the concrete sample at frequencies ranging from

ω (kHz)	**Theo.** v_p (m/s)	**Exp.** v_p (m/s)	**Theo.** α (dB/m)	**Exp.** α (dB/m)
10	2,750	2,740	0.00	0.18
100	2,738	2,700	0.06	0.73
200	2,695	2,664	0.17	0.27
400	2,660	2,661	0.28	0.31
600	2,659	2,659	0.32	0.25
800	2,661	2,658	0.34	0.29
1,000	2,663	2,668	0.36	0.33

Table 3.3: *Ultrasonic wave velocities and attenuation for cement paste (w/c = 0.375): comparison between theoretical (Theo.) and experimental (Exp.) values.*

10 kHz to 800 kHz. The comparison reveals a close match for both velocity and attenuation across all frequencies, except for a slight overestimation in the theoretical model around 200-400 kHz. This could be attributed to heterogeneities and multiple scattering in the coarse aggregate matrix. To evaluate the accuracy of the theoretical model, the Root Mean Square Error (RMSE) between the theoretical and experimental velocities was calculated. The RMSE value of approximately 251.07 m/s corresponds to 5.75% relative to the average theoretical velocity, indicating a reasonably good agreement between the theoretical predictions and experimental results.

ω (kHz)	**Theo.** v_p (m/s)	**Exp.** v_p (m/s)	**Theo.** α (dB/m)	**Exp.** α (dB/m)
10	3,907	3,879	0.01	0.03
100	4,145	4,605	0.11	0.17
200	4,241	4,743	0.24	0.19
400	4,498	4,780	0.35	0.33
600	4,657	4,789	0.39	0.38
800	4,742	4,697	0.41	0.42

Table 3.4: *Ultrasonic wave velocities and attenuation for concrete sample (a/c = 3, w/c = 0.375): comparison between theoretical (Theo.) and experimental (Exp.) values.*

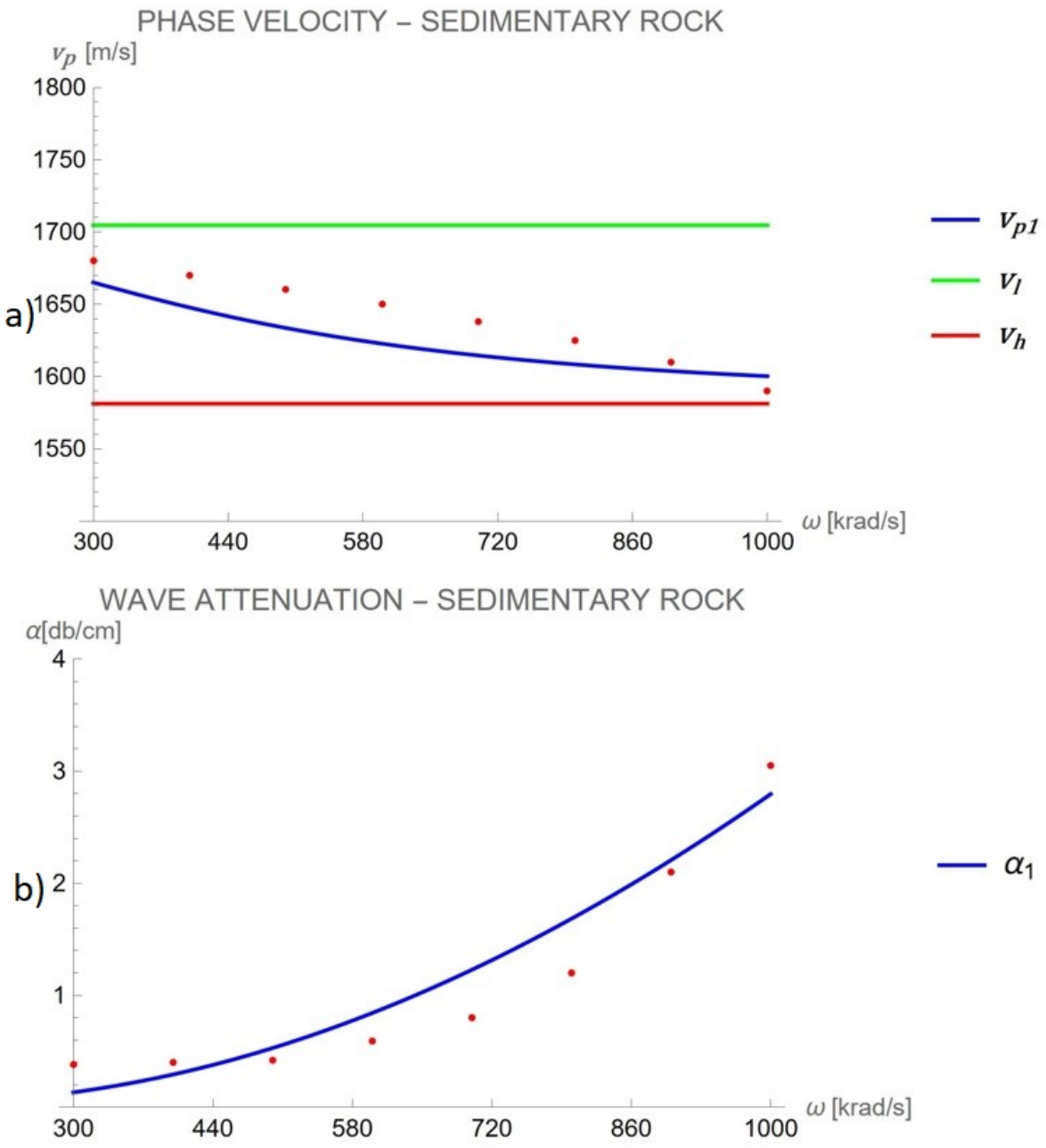

Figure 3.4: *Phase velocity v_p (*m/s*) and attenuation coefficient α (*dB/cm*) as functions of the frequency ω (*krad/s*) according to equations (3.18), subfigure a, and (3.23), subfigure b, for a sedimentary rock with constitutive parameters as shown in Table 3.1. Red points represent the experimental data from literature for phase velocity (subfigure a) and attenuation (subfigure b).*

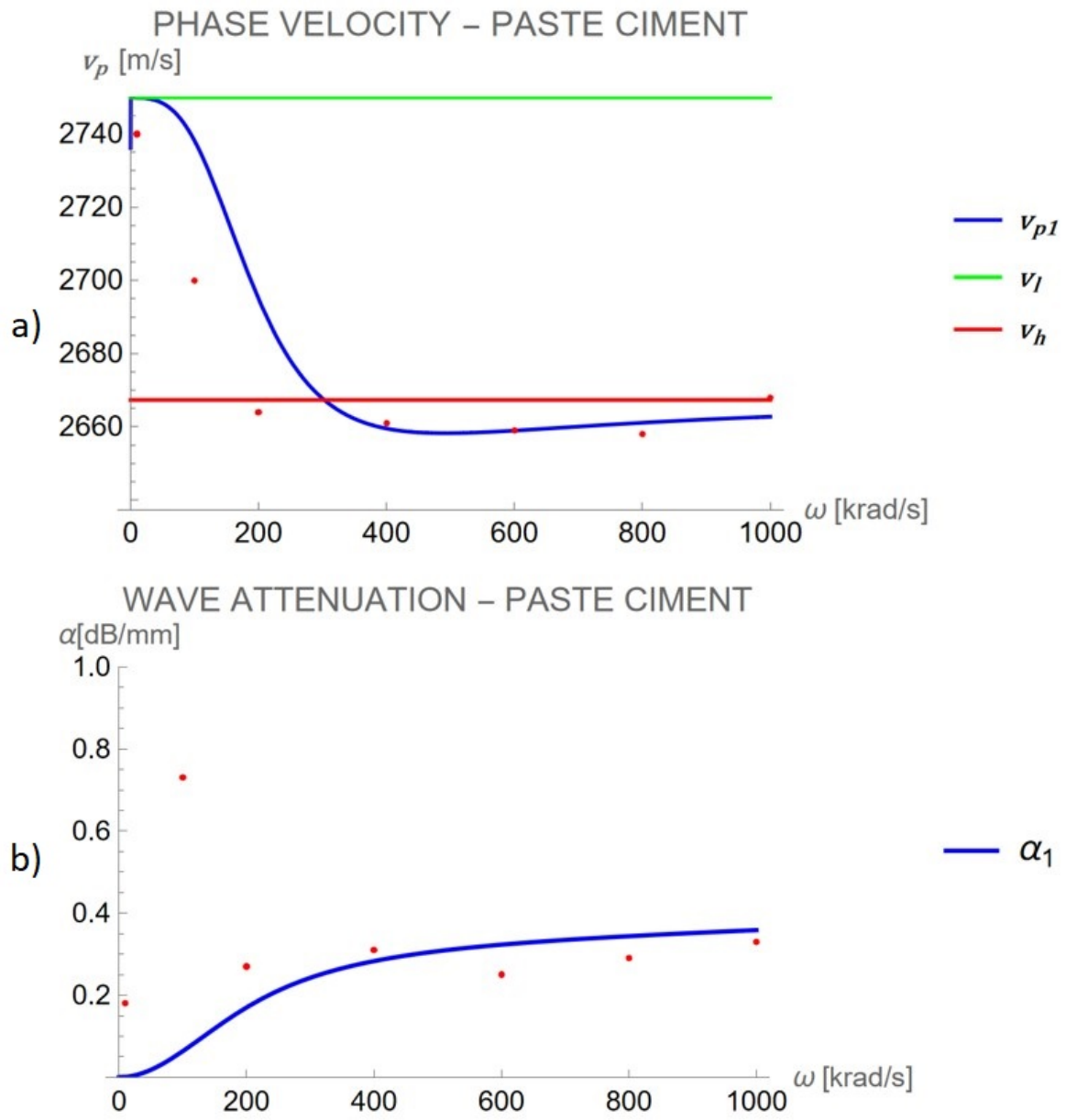

Figure 3.5: *Phase velocity v_p (*m/s*) and attenuation coefficient α (*dB/cm*) as functions of frequency ω (*krad/s*), according to equations (3.18), subfigure a, and (3.23), subfigure b, for a cement paste sample with constitutive parameters listed in Table 3.1. Red points represent the experimental data from literature for phase velocity (subfigure a) and attenuation (subfigure b).*

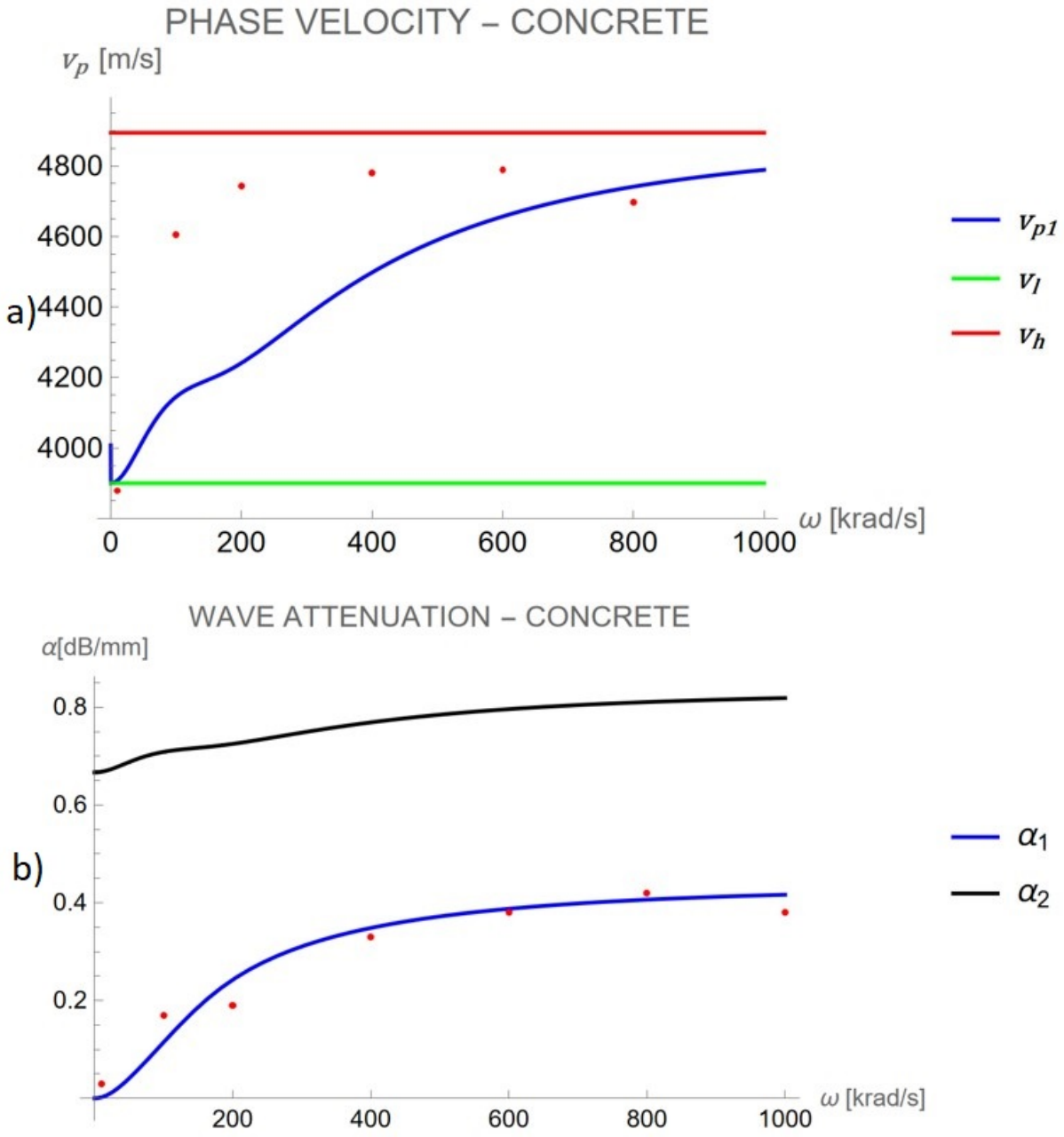

Figure 3.6: *Phase velocity v_p (*m/s*) and attenuation coefficient α (*dB/cm*) as functions of frequency ω (*krad/s*), according to equations (3.18), subfigure a, and (3.23), subfigure b, for a concrete sample with constitutive parameters listed in Table 3.1. Red points represent the experimental data from literature for phase velocity (subfigure a) and attenuation (subfigure b).*

3.4 Summary and discussion of the results

Within this section we have formulated and validated a theoretical model that allows us to characterize, for a given material, both the dispersion and attenuation of the ultrasonic wave propagating through it, as well as all the key constitutive parameters associated with ultrasonic propagation (mechanical stiffness, microstructure, internal viscosity), execpt singular points such as cavities or localized heterogeneities. The model has been constructed by applying the principle of Hamilton-Rayleigh and for the sake of simplicity, a one-dimensional model and

only the longitudinal elastic modulus have been considered, whereas for the future a more in-depth investigation can take into account also 2D/3D effects and therefore all the relevant elastic parameters. On this regard, it is important to underline that multidimensional modeling requires numerical methods such as the Finite Element Method (FEM) to tackle the added complexity due to three-dimensional wave propagation and potential nonlinearities in material behavior or boundary conditions. This approach is essential for accurately representing the effect of transducers acting over areas on the material surface, generating spherical harmonic waves. Nevertheless, the one-dimensional model presented here, despite its simplifications, reproduces experimental data with satisfactory accuracy, confirming its validity as a preliminary tool before addressing more complex multidimensional models next sections. Building on this foundation, the key findings of the research are summarized as follows, illustrating the model's effectiveness in capturing ultrasonic wave propagation phenomena:

- **Wave Dispersion:** The analytical expression for the phase velocity (Eq.(3.18)) reveals a frequency-dependent behavior with two distinct propagating modes. As frequency increases, the phase velocity transitions between two asymptotic regimes, consistent with experimental observations in complex structured materials.

- **Wave Attenuation:** Attenuation is described through the damping ratio ζ (Eq.(3.19)), derived from the real and imaginary parts of the complex wave number. This parameter quantifies energy dissipation and reflects the influence of both first- and second-gradient viscosity.

- **Characteristic Frequency:** The model predicts a characteristic frequency at which attenuation peaks. This defines a transition zone between low-frequency (non-dispersive) and high-frequency (asymptotic) behavior.

- **Agreement with Literature:** The model qualitatively reproduces trends in phase velocity and attenuation observed experimentally, notably those reported in Hofmann's work (Fig.3.1), supporting the validity of the constitutive assumptions.

- **Role of Higher-Order Effects:** The inclusion of higher-order elastic (k_2) and viscous (c_2) terms introduces additional length and time scales, enhancing the model's ability to capture the mechanical response of architectured or microstructured materials.

4 Selection of the spatial and temporal discretization for the FEM model

4.1 Strategy definition

In order to describe the propagation of an ultrasonic wave within an isotropic, homogeneous, and viscous body $\Omega \in \mathbb{R}^2$, we employ the Finite Element Method (FEM). First, we extrapolate the governing equations of motion (balance equations) starting from the previous validated one-dimensional analytical model for plane-wave propagation and we define the boundary conditions in terms of displacements on the body's edges. The domain is then discretized using a mesh, which allows the governing equations to be rewritten in their weak form, making it more suitable for FEM analysis. In the end, the objective is to obtain the displacement field $u(x_i, t)$, expressed in a Cartesian coordinate system $x_i = (x, y)$ for $\Omega \subset \mathbb{R}^2$, at every point of the body throughout the entire duration of the wave propagation simulation. From this full spatio-temporal description, the time of flight (TOF) and the wave attenuation can then be extracted. In Figures 4.1 and 4.2, the flowchart of the proposed strategy is summarized: starting from the one-dimensional analytical model, the governing equations are fully transposed into a calibrated 1D FEM formulation. Once the numerical model has been rigorously validated against the analytical reference solution in the 1D domain, it is subsequently extended to investigate wave propagation in higher-dimensional configurations (2D and potentially 3D).

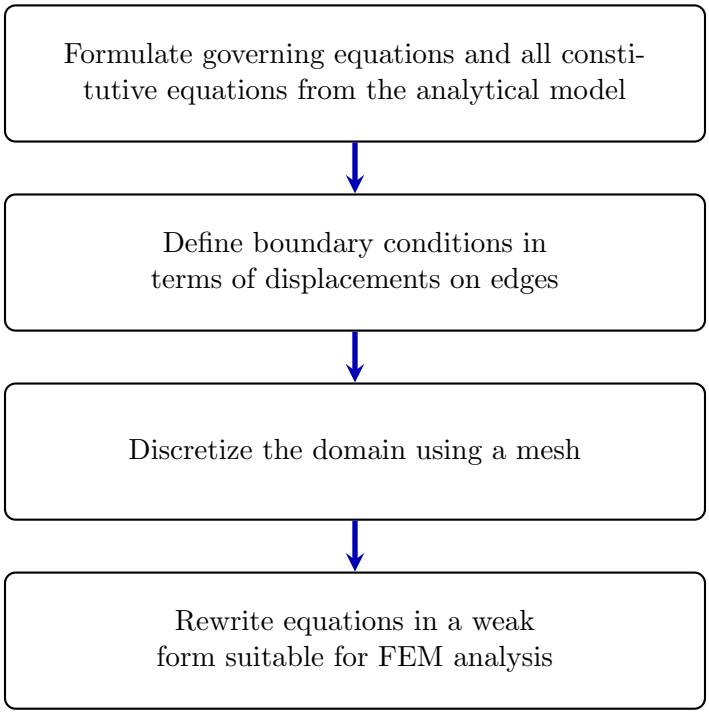

Figure 4.1: *Finite element strategy for simulating wave propagation in a two or three viscoelastic domain - modeling: governing equations, boundary conditions, and weak formulation.*

4.2 Analytical reference model

We begin from the one-dimensional analytical model for plane-wave propagation analyzed in Sections 2 and 3[71;72], which provides closed-form expressions for both the phase velocity and the attenuation in first-gradient viscoelastic materials. As seen in the previous sections, the analytical model considers an infinitely long, free one-dimensional bar subjected to a harmonic perturbation applied at its left boundary, in order to reproduce typical experimental conditions,

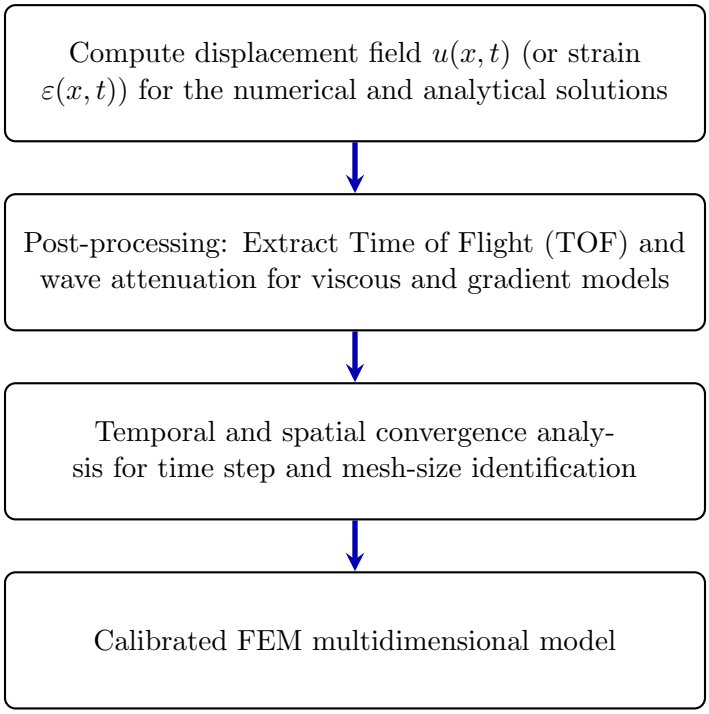

Figure 4.2: *Finite element strategy for simulating wave propagation in a multidimensional visco-elastic domain - postprocessing: numerical solution, convergence analysis, and model calibration.*

where the excitation transducer is placed at one end of the specimen and the receiver at another location. However, this choice is not essential for the formulation of the problem, as the excitation could be applied at any position without affecting the generality of the solution. We recall the governing partial differential equation of motion is

$$\rho\,\ddot{u} + c\,\dot{u} - k_1\,u'' - c_1\,\ddot{u}'' - b_n = 0, \qquad \forall x \in [0, L],\ \forall t \in \mathbb{R}, \tag{4.1}$$

where:

1. ρ is the material density,
2. k_1 is the material stiffness that takes into account the elastic modulus per unit length (equivalent to EA, respectively Young Modulus E and specimen section A),
3. c is the internal damping coefficient,
4. c_1 is the strain-gradient inertia coefficient (Kelvin–Voigt type),
5. b_n denotes external body forces (here set to zero: $b_n = 0$).

We recall also the displacement assumed in harmonic form

$$u(x,t) = \mathrm{Re}\Big(u_0\, e^{\,i(\omega t - k_w x)}\Big)\,, \tag{4.2}$$

where:

1. ω is the circular frequency,
2. k_w is the (complex) wave number,
3. u_0 is the initial wave amplitude,

4. x is the spatial coordinate,

5. i is the imaginary number,

6. $\mathrm{Re}(\cdot)$ denotes the real part.

In section 2.2 we have analyzed how to obtain closed-form dispersion relations, starting from the wavenumber k_w; when only viscosity is present ($c > 0$ and $c_1 = 0$), the real and imaginary parts of the wavenumber are given exactly by:

$$\mathrm{Re}(k_w) = \omega\sqrt{\frac{\rho}{k_1}}\left(1+\left(\frac{\omega_c}{\omega}\right)^2\right)^{1/4}\cos\left(-\tfrac{1}{2}\arctan\left(\frac{\omega_c}{\omega}\right)\right), \tag{4.3}$$

$$\mathrm{Im}(k_w) = \omega\sqrt{\frac{\rho}{k_1}}\left(1+\left(\frac{\omega_c}{\omega}\right)^2\right)^{1/4}\sin\left(-\tfrac{1}{2}\arctan\left(\frac{\omega_c}{\omega}\right)\right), \tag{4.4}$$

which coincides with Eqs. (2.45) and (2.46), provided that the characteristic viscous frequency is defined as

$$\omega_c = \frac{c}{\rho}. \tag{4.5}$$

The intrinsic material attenuation coefficient

$$\alpha(\omega) = -\mathrm{Im}(k_w) \tag{4.6}$$

governs the exponential decay of the wave amplitude $A(x)$ along the spatial coordinate x into the material as following:

$$A(x) = A_0\, e^{\alpha x}. \tag{4.7}$$

Regarding the wave propagation velocity, it is worth noting that, in dissipative media, the definition of phase velocity requires particular care. While several works in the literature[91] define the phase velocity as the real part of the ratio ω/k_w, i.e. $\mathrm{Re}(\omega/k_w)$, this expression is only valid in the purely elastic case, where the wavenumber is real. When dissipative mechanisms are present, the wavenumber becomes complex and can be written as

$$k_w = k_w^{\mathrm{Re}} + i\, k_w^{\mathrm{Im}}, \tag{4.8}$$

where

$$k_w^{\mathrm{Re}} = \mathrm{Re}(k_w), \qquad k_w^{\mathrm{Im}} = \mathrm{Im}(k_w) \tag{4.9}$$

Here, k_w^{Re} governs the spatial oscillation of the wave, while k_w^{Im} controls its exponential attenuation, as discussed before. Starting from the standard harmonic ansatz used in the analytical model (4.2), and substituting the decomposition (4.8), the displacement field becomes

$$u(x,t) = A_0\, e^{\alpha x}\cos(\omega t - \mathrm{Re}(k_w)\, x)\,. \tag{4.10}$$

Then, equation (4.10) shows that the wave amplitude decays exponentially with the propagation distance x, while the oscillatory behavior is governed by the phase

$$\phi(x,t) = \omega t - \mathrm{Re}(k_w)\, x. \tag{4.11}$$

To determine the phase velocity, one must track the propagation of a *constant-phase point*. Imposing $\phi(x,t) = \text{const}$ and differentiating with respect to time yields

$$\omega\, \mathrm{d}t - \mathrm{Re}(k_w)\, \mathrm{d}x = 0, \tag{4.12}$$

which leads directly to

$$\frac{\mathrm{d}x}{\mathrm{d}t} = \frac{\omega}{\mathrm{Re}(k_w)}. \tag{4.13}$$

In conclusion, the phase velocity is therefore correctly defined as

$$v_p(\omega) = \frac{\omega}{\mathrm{Re}(k_w)}. \tag{4.14}$$

It is important to emphasize that this definition differs from the commonly used expression $\mathrm{Re}(\omega/k_w)$, unless $\mathrm{Im}(k_w) = 0$: the two expressions coincide only in the purely elastic, non-dissipative case, then in dissipative media, using $\mathrm{Re}(\omega/k_w)$ leads to an incorrect estimate of the wave propagation speed. The dispersion relations (4.7), and (4.14) form the analytical benchmark are used in the present Section 4 to calibrate the finite element implementation of the first-gradient viscoelastic model.

4.3 Definition of constitutive parameters of the material and analytical outputs

The reference one-dimensional specimen used in this study for the numerical simulation has a total length of `L` = 200 mm. The material is assumed to be homogeneous and isotropic, with density $\rho = 1.780 \times 10^{-3}$ g/mm^3 and the Poisson ratio of $\nu = 0$ is adopted, meaning that the material is modeled as laterally unconstrained under axial deformation since we are in 1D domain. The elastic response is characterized by a Young's modulus $E = 100\,000$ MPa, which governs the stiffness k_1 of the medium and directly influences the longitudinal wave speed. The adopted properties are comparable to the longitudinal stiffness of unidirectional Carbon Fiber Reinforced Polymer (CFRP) composite laminate, idealized here as an equivalent one-dimensional isotropic medium. To properly investigate dissipative mechanisms within the frequency range typical of ultrasonic nondestructive testing (150 kHz–1,000 kHz), it is necessary to select values of the viscous coefficient c that produces a measurable attenuation over realistic propagation distances (50–150 mm). Table 4.1 reports for the viscous case, the analytical phase velocities (computed from eq. (4.14)) and the corresponding amplitude decay (computed from Eq. (4.7)) at different excitation frequencies and evaluated at three spatial locations within the domain. These results are obtained from the one-dimensional analytical model using the viscous coefficient $c = 0.75$ g/(mm · ms), together with the constitutive parameters introduced above.

f	v_p	λ	$A(x)/A_0$		
[kHz]	[mm/ms]	[mm]	$x = 50$ mm	$x = 100$ mm	$x = 150$ mm
150	7,322.732	48.818	25.3%	6.4%	1.6%
250	7,429.940	29.720	24.8%	6.2%	1.5%
375	7,465.767	19.909	24.7%	6.1%	1.5%
500	7,478.595	14.957	24.6%	6.1%	1.5%
750	7,487.853	9.984	24.6%	6.0%	1.5%
1,000	7,491.112	7.491	24.5%	6.0%	1.5%

Table 4.1: *Phase velocity according equation* (4.14)*, wavelength and amplitude attenuation according equation* (4.7) *for the viscous model at different propagation distances (percentage of the initial amplitude A_0). Simulation parameters: $c = 0.75$ g/(mm · ms), $c_1 = 0$ g · mm/ms, $\rho = 1.780 \times 10^{-3}$ g/mm^3, $k_1 = 100 \times 10^3$ g · mm/ms^2, specimen length $L = 200$ mm.*

In the previous sections and in the reference literature presenting this analytical model[71;72], the discussion is primarily focused on the phase velocity behavior. For this reason, in the

following we provide a detailed analysis of the attenuation characteristics of the viscous model, thereby complementing and extending the results already available in [71;72] and in the section 2.2. Conversely, as far as the phase velocity is concerned, we will limit ourselves to summarizing the numerical results and their physical interpretation, consistently with the analytical insights already discussed previously. We begin by analyzing the attenuation coefficient $\alpha(\omega)$, which is directly related to the imaginary part of the wavenumber. Subsequently, we investigate the corresponding amplitude decay, consistently with the analytical results reported in Table 4.1.
First, we state that the viscous model exhibits an almost frequency-independent attenuation over the range of frequencies investigated in this study, with a slight reduction observed at lower frequencies. This behavior can be directly interpreted from the analytical expression of the complex wavenumber and then of attenuation coefficient that satisfies the following asymptotic limits

$$\lim_{\omega\to 0} \alpha(\omega) = 0, \qquad \lim_{\omega\to\infty} \alpha(\omega) = \frac{c}{2\sqrt{\rho\, k_1}}. \tag{4.15}$$

which implies vanishing attenuation in the low-frequency limit and a finite, frequency-independent attenuation at high frequencies.
The Figure 4.3 highlights the nearly flat attenuation curves observed at higher frequencies, where the imaginary part of the wavenumber approaches a constant value. Conversely, although the attenuation coefficient theoretically tends to zero as the frequency approaches zero, this asymptotic regime cannot be verified within the frequency range considered here. Indeed, lowering the excitation frequency would require wavelengths significantly larger than the sensor spacing and the specimen length, making the extraction of meaningful time-of-flight and attenuation measurements impractical.
In addition to the attenuation coefficient, the amplitude decay is directly evaluated by monitoring the ratio $A(x_s)/A_0$ as a function of frequency at a fixed sensor position, according equations (4.7) in Figure 4.4.
These representations provide a more intuitive measure of energy loss during propagation, highlighting the markedly different dissipative behaviors of the two models considered. In detail, as a consequence of (4.15), for the viscous model the amplitude decay behaves as

$$\lim_{\omega\to 0} \frac{A(x_s)}{A_0} = 1, \qquad \lim_{\omega\to\infty} \frac{A(x_s)}{A_0} = \exp\big(-\alpha_\infty x_s\big). \tag{4.16}$$

At low frequencies (long wavelengths), viscous dissipation becomes negligible, and the wave propagates almost without attenuation. As a result, the amplitude measured at the sensor remains close to the imposed amplitude at the actuator (the ratio $A(x_s)/A_0$ tends to 1). At high frequencies, the attenuation coefficient approaches a constant value, leading to an exponential amplitude decay that is independent of frequency. Physically, this reflects the classical behavior of internal damping, where viscosity introduces a fixed energy loss per unit propagation distance once the oscillation rate is sufficiently high. Consequently, the amplitude decay saturates and no further frequency dependence is observed in the high-frequency regime. In conclusion, we can state that the amplitude decay behavior depends strictly by the attenuation coefficient and by the distance of the sensor position (observation point) from the actuator. Moreover, the dispersive behavior of the phase velocity is clearly visible in both cases. As shown in Section 2.2, the elastic (non-dissipative) phase velocity in condition of uniaxial strain is obtained as

$$v_p^{\text{elastic}} = \sqrt{\frac{k_1}{\rho}}, \tag{4.17}$$

which, for the constitutive parameters adopted in this study, yields $v_p^{\text{elastic}} = 7.495$ mm/ms $=$ 7.495 m/s.
In the viscous case[71] (see Figure 4.5), the phase velocity increases from zero at very low frequencies and asymptotically approaches the elastic limit v_p^{elastic} (Eq. (4.17)) for sufficiently

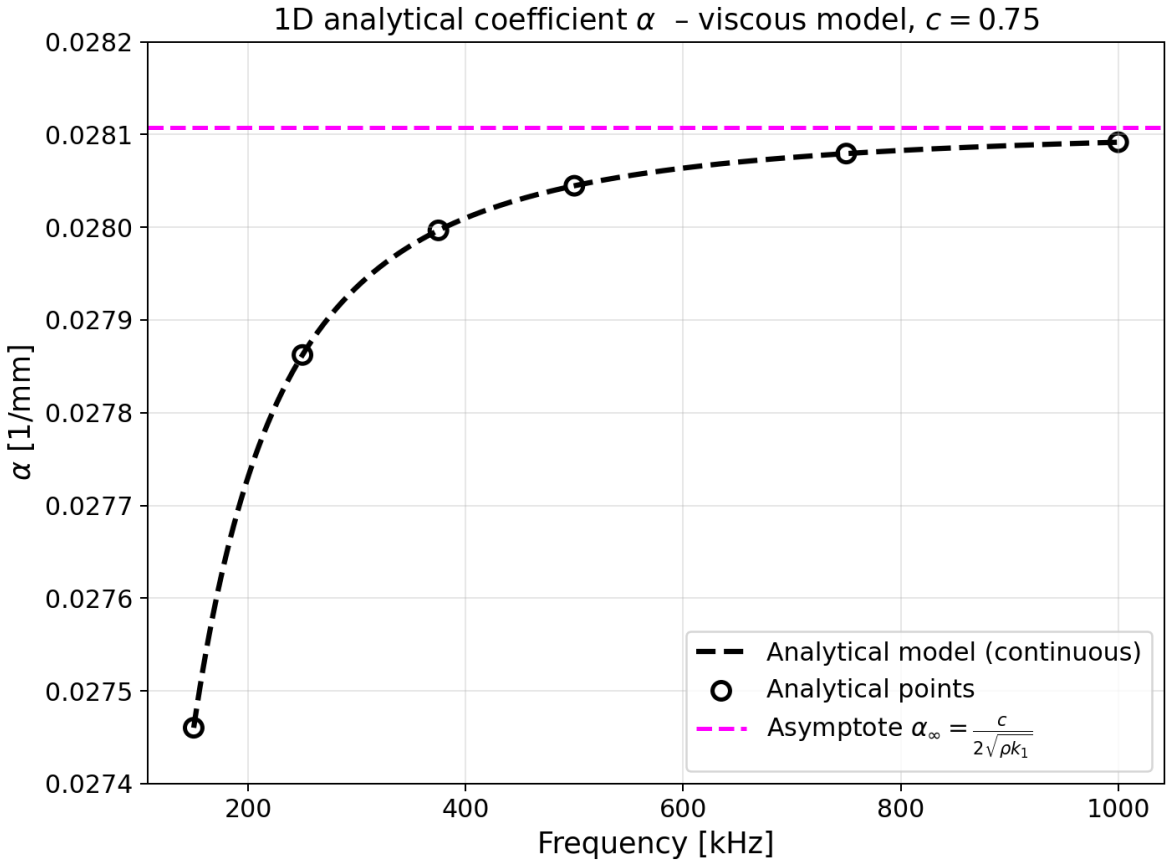

Figure 4.3: *Attenuation coefficient as a function of frequency for the one-dimensional analytical viscous model ($c \neq 0$, $c_1 = 0$) according equation (4.4). Simulation parameters:* $c = 0.75$ g/(mm·ms), $c_1 = 0$ g·mm/ms, $\rho = 1.780\times10^{-3}$ g/mm^3, $k_1 = 100\times10^3$ g·mm/ms^2, $L =$ 200 mm. *The dashed black curve corresponds to the analytical attenuation curve, while circular markers represent the discrete analytical values. The analytical points values are* $\alpha(150\,\text{kHz}) = 2.746 \times 10^{-2}\,\text{mm}^{-1}$, $\alpha(250\,\text{kHz}) = 2.786 \times 10^{-2}\,\text{mm}^{-1}$, $\alpha(375\,\text{kHz}) = 2.800 \times 10^{-2}\,\text{mm}^{-1}$, $\alpha(500\,\text{kHz}) = 2.804 \times 10^{-2}\,\text{mm}^{-1}$, *and* $\alpha(750\,\text{kHz}) = 2.808 \times 10^{-2}\,\text{mm}^{-1}$. *The magenta dashed horizontal line denotes the high-frequency asymptotic attenuation* $\alpha_\infty \approx 0.281$.

high excitation frequencies. This behavior, also discussed in [71] and into the previous section 2.2, is consistent with the classical internal-damping model, in which low-frequency oscillations are strongly influenced by viscosity, while high-frequency waves recover the underlying elastic response. These trends allow us to identify suitable ranges of c for which attenuation remains observable but not excessively strong, thereby ensuring meaningful comparison with the 2D FEM simulations presented later in the work.

4.4 Variational formulation and the problem setup

4.4.1 Weak form

For the implementation of the FEM procedure, we recall equation (2.31) from Section 2.2.1

$$F(u, \delta u) = \int_\Omega \left(\rho\, \ddot{u}\, \delta u + c\, \dot{u}\, \delta u + k_1\, u'\, \delta u' + c_1\, \dot{u}'\, \delta u' \right) \mathrm{d}x = 0. \tag{4.18}$$

Each contribution appearing under the integral in Eq. (5.3) has a clear physical interpretation:

1. $\rho\, \ddot{u}\, \delta u$ - inertial term (mass × acceleration),

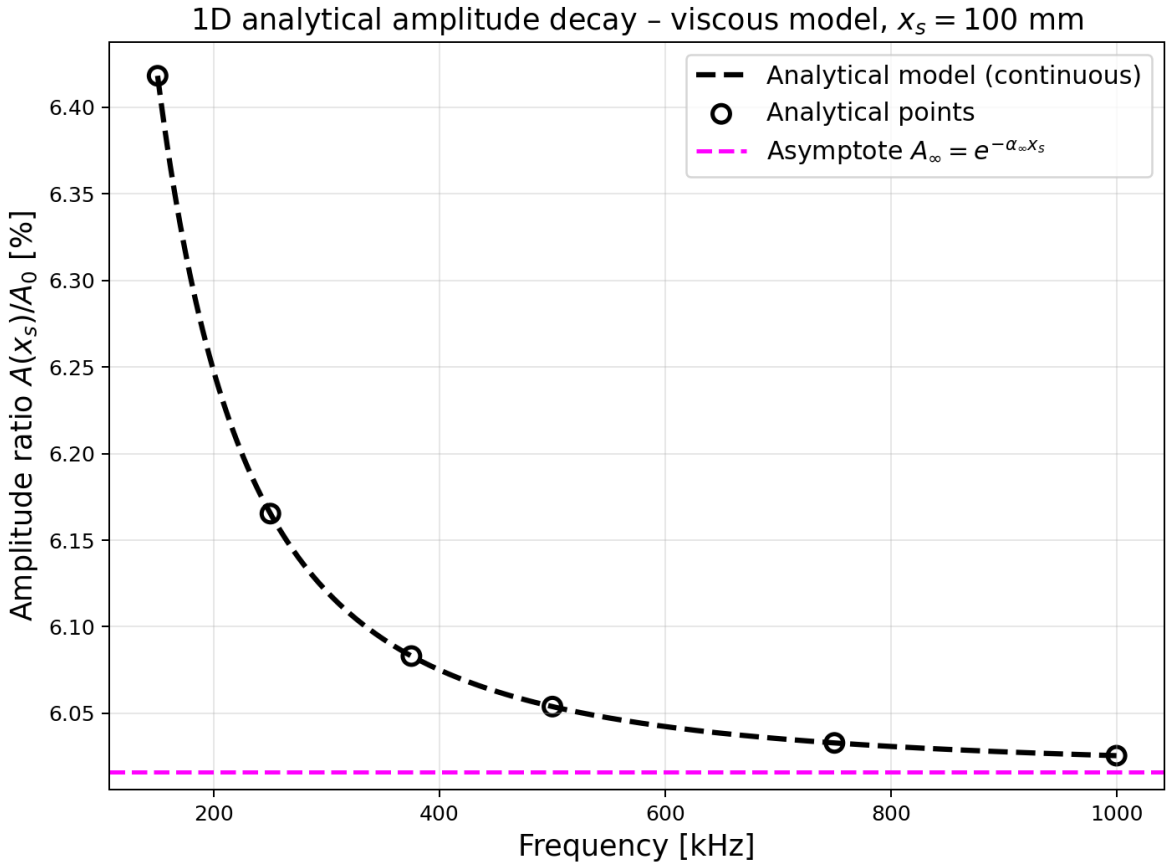

Figure 4.4: *Analytical amplitude decay at the sensor position* $x_s = 100$ mm *for the one-dimensional analytical viscous model (*$c \neq 0$, $c_1 = 0$*) according equation* (4.7)*. Simulation parameters:* $c = 0.75$ g/(mm · ms), $c_1 = 0$ g · mm/ms, $\rho = 1.780 \times 10^{-3}$ g/mm^3, $k_1 = 100 \times 10^3$ g · mm/ms^2, $L = 200$ mm*. The dashed black curve represents the continuous analytical prediction* $A(x_s)/A_0 = \exp[-\alpha^{\text{visc}}(\omega)\, x_s]$*, while circular markers denote the discrete analytical values reported in Table 4.1 for the frequencies 150* kHz*, 250* kHz*, 375* kHz*, 500* kHz *and 750* kHz*. Due to the asymptotic convergence of the viscous attenuation coefficient to a finite value, the amplitude ratio approaches a nonzero plateau at high frequencies.*

2. $c\,\dot{u}\,\delta u$ - internal viscous dissipation,
3. $k_1\,u'\,\delta u'$ - classical elastic stiffness (internal work of strain),
4. $c_1\,\dot{u}'\,\delta u'$ - strain-gradient, rate-dependent dissipation.

This weak formulation is the exact variational counterpart of the analytical PDE in Eq. (4.1). Its structure mirrors the analytical model term by term, ensuring complete consistency between the theoretical derivation and its numerical finite element implementation.

4.4.2 Boundary conditions

In coherence with the analytical reference model, the numerical simulations do not impose any kinematic constraints except on the left edge of the domain ($x = 0$) at the actuator, where the ultrasonic perturbation is injected.
However, given the one-dimensional setting of the problem, deformation is allowed exclusively along the x-direction, leading to a purely uniaxial strain condition.

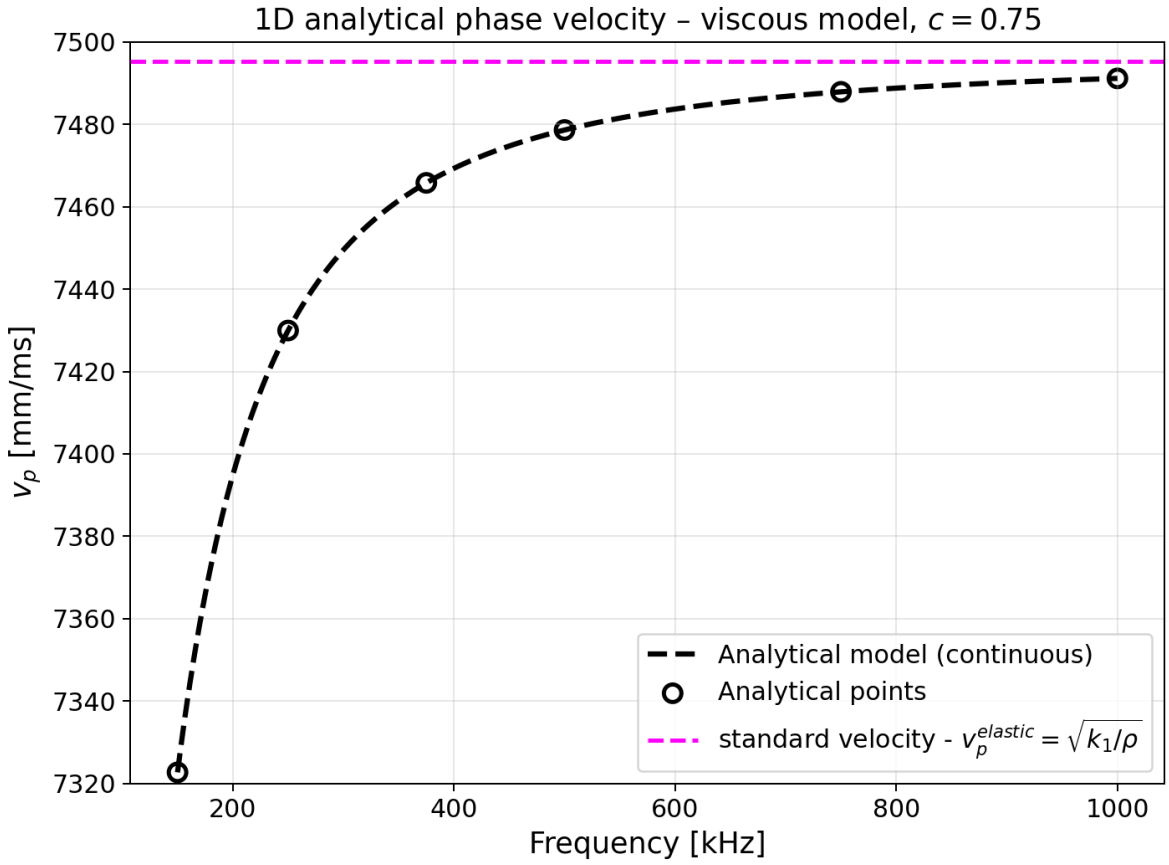

Figure 4.5: *Phase velocity as a function of frequency for the one-dimensional analytical viscous model ($c \neq 0$, $c_1 = 0$), according equation (4.14). Simulation parameters: $c = 0.75$ g/(mm · ms), $c_1 = 0$ g · mm/ms, $\rho = 1.780 \times 10^{-3}$ g/mm^3, $k_1 = 100 \times 10^3$ g · mm/ms^2, $L = 200$ mm. The dashed black curve represents the continuous analytical dispersion relation, while circular markers indicate the discrete analytical values listed in Table 4.1 or the frequencies 150 kHz, 250 kHz, 375 kHz, 500 kHz and 750 kHz. The magenta dashed horizontal line corresponds to the standard elastic wave velocity according equation (4.17) equal to 7.495 mm/ms.*

Following the analytical solution introduced in Eq. (4.2), the imposed excitation must reproduce the same harmonic structure used to derive the dispersion relations. In particular, starting from equation (4.10), the displacement applied at the left boundary ($x = 0$) is defined as

$$u(0, t) = -A_0 \cos(\omega t), \tag{4.19}$$

where A_0 is the imposed amplitude equal to 0.01 mm in our simulation and ω is the excitation frequency corresponding to the circular frequency $\omega = 2\pi f$ expressed in krad/ms, applied on the left edge of the bar, at the actuator. The minus sign simply indicates that the imposed displacement is directed along the negative x-axis and does not influence the dispersion behaviour. Figure 4.6 shows the time history of the imposed boundary condition.

4.4.3 Sensor position

A virtual sensor is placed at a distance x from the left boundary, where it records the time history of the displacement field $u(x, t)$. We investigate the three sensor positions shown for the analytical simulation in Table 4.1: 50 mm, 100 mm and 150 mm. Figure 4.7 shows the geometry of the 1D bar together with the actuator location and the positions of the sensors

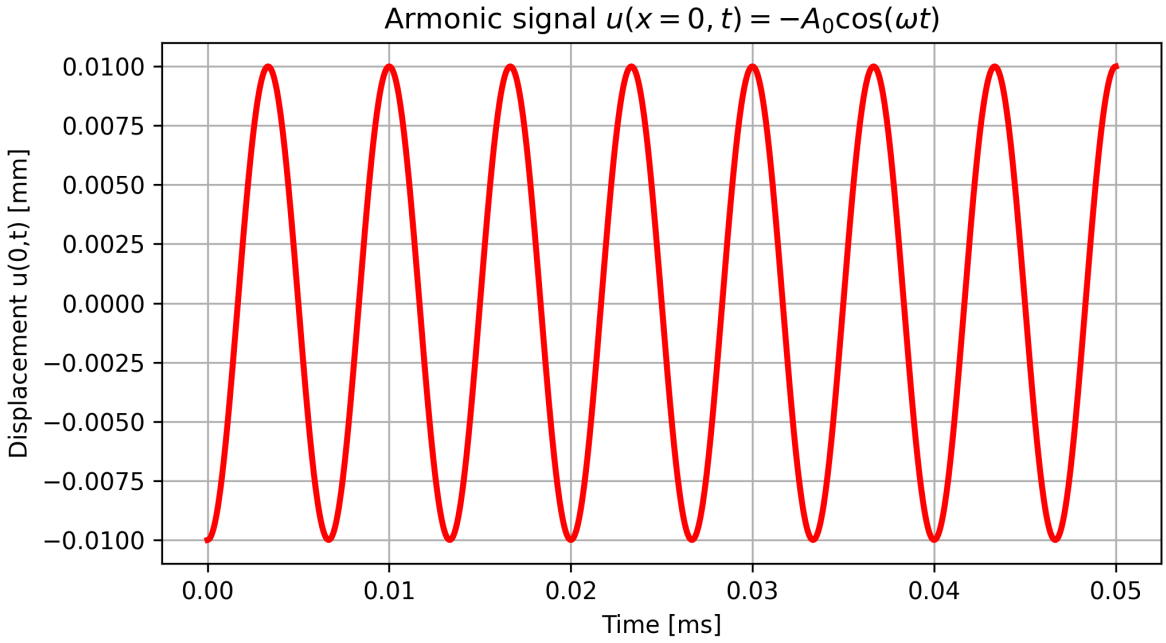

Figure 4.6: *Time history of the prescribed displacement at the actuator location ($x = 0$) for an excitation frequency $f = 150$ kHz and amplitude $A_0 = -0.01$ mm. The harmonic boundary condition $u(0,t) = -A_0\cos(\omega t)$ is imposed at the left boundary of the domain to generate the ultrasonic wave.*

used to evaluate time-of-flight and attenuation.

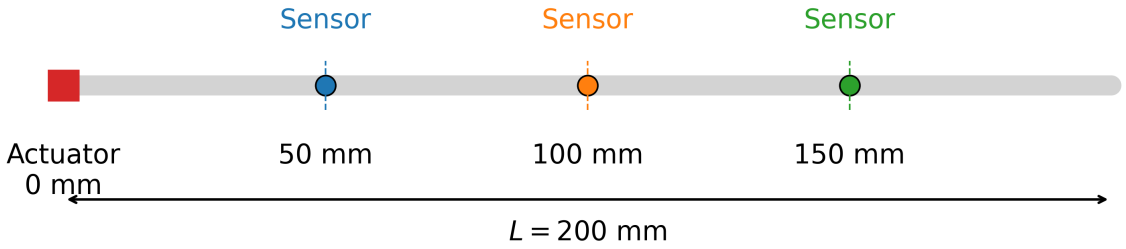

Figure 4.7: *Schematic representation of the one-dimensional bar considered in the numerical and analytical analyses. The actuator is located at the left boundary of the domain ($x = 0$) and generates the harmonic excitation, while three sensors are positioned along the bar at $x =$ 50 mm, $x = 100$ mm, and $x = 150$ mm. The total length of the bar is $L = 200$ mm.*

Figures 4.8 shows the time histories of the displacement recorded at the three sensor locations ($x_s = 50$ mm, 100 mm, and 150 mm), obtained from the FEM viscous model at a fixed excitation frequency of 150 kHz. At this stage, the analysis intentionally abstracts from the influence of spatial / temporal discretization parameters and from the peak detection procedure, that will be systematically investigated in the dedicated analysis presented in the following subsections. All signals start from zero displacement and initially remain quiescent, until the travelling wave, generated at the actuator, reaches the corresponding sensor position. A clear time shift between the responses can be observed: the farther the sensor is from the excitation boundary, the later the onset of the displacement signal occurs. After an initial transient phase associated with the

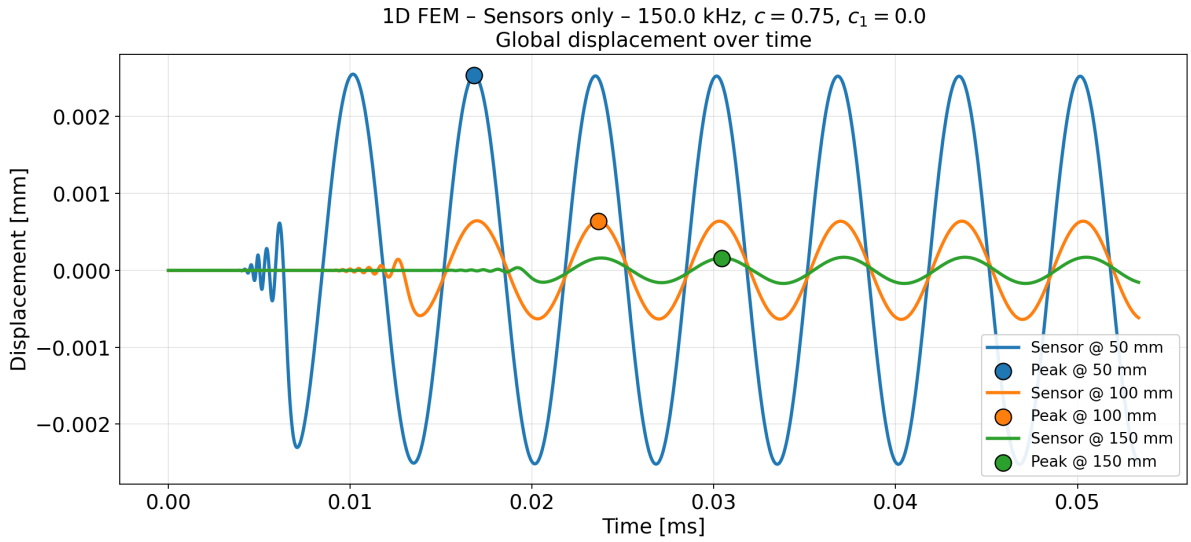

Figure 4.8: *1D FEM viscous model - displacement time histories recorded at the three sensor locations (x_s = 50 mm, 100 mm, and 150 mm) for the viscous model ($c \neq 0$, $c_1 = 0$) at frequency f = 150 kHz. Simulation parameters: $c = 0.75$ g/(mm · ms), $c_1 = 0$ g · mm/ms, $\rho = 1.780 \times 10^{-3}$ g/mm^3, $k_1 = 100 \times 10^3$ g · mm/ms^2, $L = 200$ mm. The peak displacements at the sensor locations occur at $t_s \approx 0.0168$ ms with $u_s \approx 2.53 \times 10^{-3}$ mm for $x_s = 50$ mm, $t_s \approx 0.0236$ ms with $u_s \approx 6.42 \times 10^{-4}$ mm for $x_s = 100$ mm, and $t_s \approx 0.0304$ ms with $u_s \approx 1.61 \times 10^{-4}$ mm for $x_s = 150$ mm. The progressive delay in the onset of the signals reflects the finite wave propagation speed, while the systematic decrease in amplitude with increasing distance from the actuator highlights the effect of viscous dissipation along the bar. Due to the strong attenuation introduced by the viscous mechanism, no boundary reflection effects are observable within the time window considered.*

wave arrival, characterized by small-amplitude oscillations around zero that gradually increase in magnitude, each signal progressively evolves toward a quasi-stationary harmonic regime. short transient phase with small oscillations around zero that gradually increase in magnitude, is caused by the abrupt initialization of the harmonic boundary condition. A boundary condition of the form $1 - \cos(\omega t)$ removes the initial transient by enforcing zero displacement at $t = 0$, but introduces a non-zero mean value, resulting in an artificial rigid offset in the response. The harmonic condition $-A_0 \cos(\omega t)$ is therefore retained. The associated start-up oscillations are confined to a short transient and are filtered out during post-processing, so that they do not influence the evaluation of phase velocity and attenuation.

In addition, the Figure 4.8 highlights a progressive reduction of the signal amplitude with increasing sensor distance from the actuator. This behavior is a direct manifestation of the dissipative mechanisms acting during propagation, which attenuate the wave as it travels along the specimen. To quantitatively characterize the attenuation of the propagating wave, the peak amplitudes of the displacement signals recorded at the sensor locations are extracted once the quasi-stationary regime is reached. For each sensor position x_s, a representative positive peak $|u_{\text{peak}}(x_s)|$ is selected from the stable portion of the signal and used to describe the spatial decay of the wave amplitude, accordingly equation (4.7).

Figure 4.9 shows the spatial decay of the peak displacement amplitudes extracted from the FEM simulations for the viscous model. In the figure, the discrete markers correspond to the FEM peak amplitudes measured at the sensor locations, while two continuous curves are reported: (i) the analytical prediction obtained using the attenuation coefficient α derived from the complex wavenumber, and (ii) an exponential fit of the form (4.7) directly applied to the FEM data.

However, the close agreement between the analytically predicted attenuation curve and the

fitted FEM decay confirms the consistency between the numerical results and the underlying analytical model. Although a fully systematic convergence and peak-detection procedure is still not discussed at this stage of this study, however, the spatial and temporal resolutions employed in the present sensor position analysis and the selected reference peak are deemed adequate for the analyzes presented herein. Moreover, the comparison highlights the markedly different attenuation mechanisms associated with the viscous and strain-gradient formulations, as reflected by the distinct values of the attenuation coefficient.

The selection of the sensor position x_s must follow a set of physical and numerical criteria to ensure a reliable extraction of the time of flight and amplitude decay.

First, the sensor must be sufficiently far from the excitation boundary so that the travelling wave completes at least two/three wavelengths before being recorded. This condition ensures that the wavefield has fully developed and that near-field effects do not contaminate the measurement. According to Table 4.1, and considering that the largest wavelength is approximately 50 mm, the sensor position must be placed in our simulation at a distance greater than 100 mm from the excitation boundary.

Second, the sensor must be placed at a distance where dissipative mechanisms are observable, while still preserving a measurable portion of the wave amplitude. If the sensor is located too far from the excitation boundary, the wave may be excessively attenuated before reaching it, preventing any meaningful identification of its arrival time or amplitude decay. Consistently with the attenuation values already reported in Table 4.1, the selected dissipative coefficients produce a substantial amplitude reduction along the propagation path. In particular, at $x_s = 150$ mm the signal is in many cases almost completely damped, especially for the viscous model but also at high frequencies for the strain-gradient model. This confirms that sensor locations placed too close to the far boundary of the specimen must be excluded, since the wavefield becomes too weak to be reliably measured. Moreover, with reference to Figure 4.9, it can be clearly observed that the discrepancy between the attenuation coefficient identified from the FEM data and the corresponding analytical prediction increases with the distance of the sensor from the actuator. This behavior is expected, as the cumulative effect of numerical dissipation, phase errors, and peak-selection uncertainty becomes more pronounced at larger propagation distances, where the signal amplitude is significantly reduced. Conversely, positions near the excitation boundary do not allow enough propagation distance to capture dispersive or dissipative trends.

Third, reflections from the right boundary must be avoided. Unlike the analytical mode, where the bar is infinite and no reflections occur, the finite computational domain of the FEM model may generate reflected waves that superimpose on the incident wave, corrupting the evaluation of attenuation and phase velocity. For instance, refering to Figure 4.10 boundary reflection effects are clearly visible within the observed time window for a sensor located near the right boundary of the sample. In particular, for the sensor positioned at $x_s = 190$ mm the influence of reflected waves becomes apparent at approximately the second wavefront. The presence of boundary reflections is identified by a clear increase in the measured displacement amplitude, which contrasts with the expected monotonic decay due to dissipation. This amplitude growth is caused by the superposition of the reflected waves onto the incident wavefield, effectively injecting additional energy at the sensor location. As a consequence, beyond these time instants the recorded signals are no longer suitable for a reliable estimation of attenuation or phase velocity. Since this risk increases as the sensor position approaches the free end of the bar, sensor locations closer to the specimen boundary must be excluded.

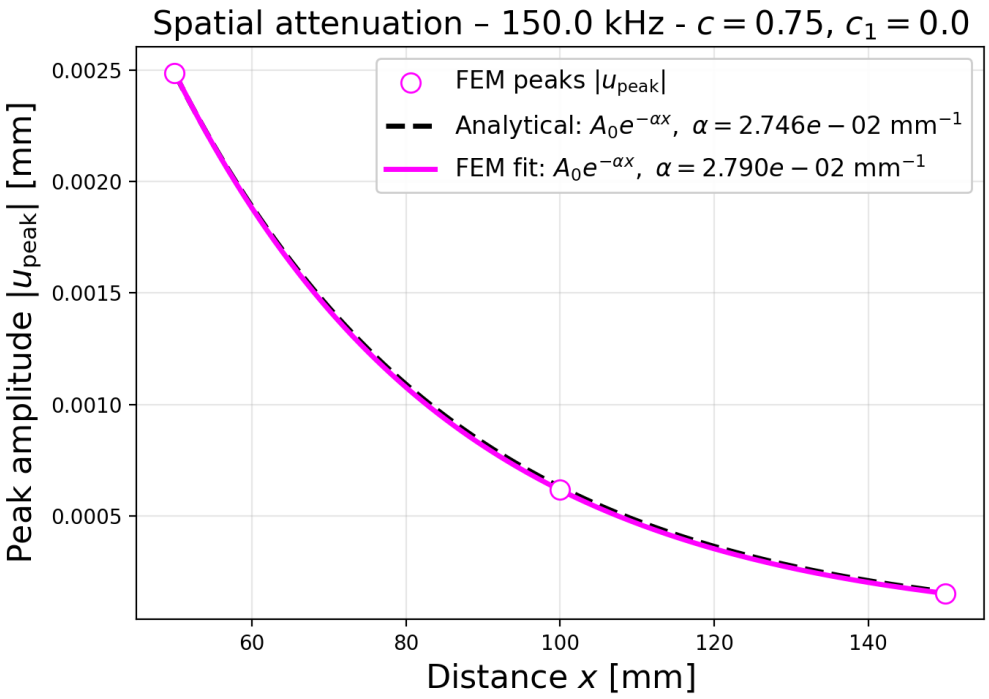

Figure 4.9: *Spatial attenuation of the displacement peak amplitude for the viscous model ($c \neq 0$, $c_1 = 0$) at frequency $f = 150$ kHz along the axial coordinate x of the bar. Simulation parameters: $c = 0.75$ g/(mm · ms), $c_1 = 0$ g · mm/ms, $\rho = 1.780 \times 10^{-3}$ g/mm^3, $k_1 = 100 \times 10^3$ g · mm/ms^2, $L = 200$ mm. The FEM peak amplitudes, represented by the circular markers, are located at $(x_s, |u_{peak}|) = (50$ mm, 2.53×10^{-3} mm), (100 mm, 6.42×10^{-4} mm), and (150 mm, 1.61×10^{-4} mm), corresponding to peak arrival times $t_s \approx 0.0168$, 0.0236, and 0.0304 ms, respectively from Figure 4.8. The dashed black curve represents the analytical attenuation law (4.7), with $\alpha_{ANA} = 2.746 \times 10^{-2}$ mm^{-1}. The solid magenta curve corresponds to the exponential fit of the FEM data, yielding $\alpha_{FEM} \approx 2.75 \times 10^{-2}$ mm^{-1}.*

	Sensor position		
Criterion	**50 mm**	**100 mm**	**150 mm**
Sufficient distance for wavefield development	×	✓	✓
Measurable dissipation with sufficient signal amplitude	×	✓	×
Low risk of boundary reflection influence	✓	✓	×

Table 4.2: *Qualitative assessment of the sensor positions with respect to the three selection criteria: (i) sufficient propagation distance for wavefield development, (ii) measurable dissipative effects without excessive attenuation, and (iii) negligible boundary reflection contamination.*

A qualitative summary of the sensor selection criteria is reported in Table 4.2. Considering these three reasons, we choose for our simulation the sensor position at $x_s = 100$ mm, which provides a suitable compromise between sufficient propagation distance, detectable dissipative effects, and minimal risk of reflection artifacts.

4.5 Peak-detection strategy

Once the global time histories of the displacement at a given excitation frequency are available from both the FEM and the analytical simulations, it is necessary to identify the displacement

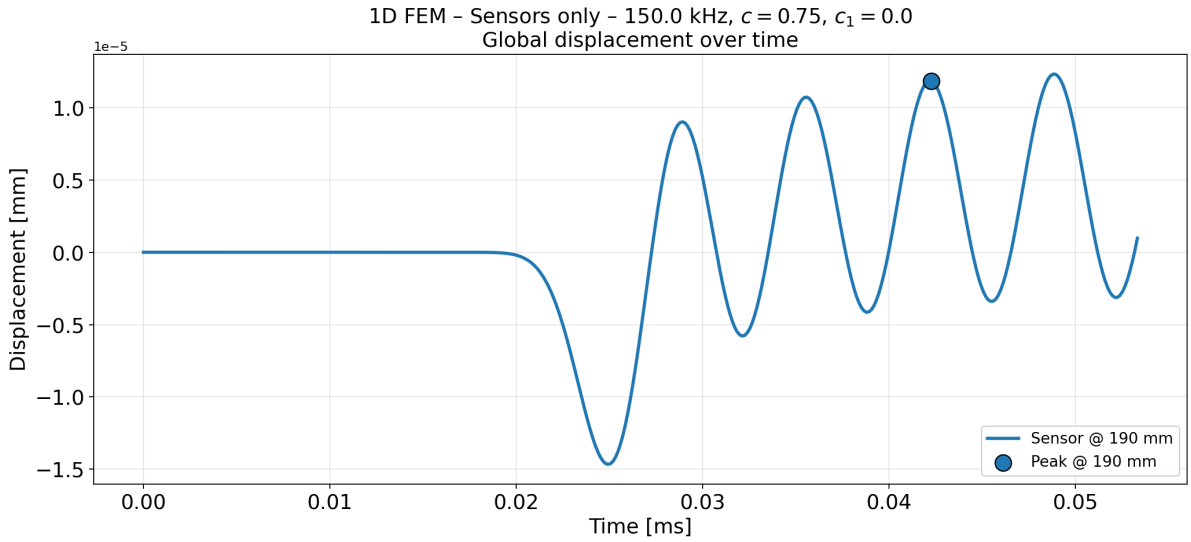

Figure 4.10: *1D FEM viscous model - displacement time history recorded at a sensor located close to the right boundary ($x_s = 190$ mm) for the viscous material model ($c \neq 0$, $c_1 = 0$) at frequency $f = 150$ kHz. Simulation parameters: $c = 0.75$ g/(mm · ms), $c_1 = 0$ g · mm/ms, $\rho = 1.780 \times 10^{-3}$ g/mm^3, $k_1 = 100 \times 10^3$ g · mm/ms^2, specimen length $L = 200$ mm. Four displacement peaks are observed within the selected time window at approximately $t_{s,1} \approx 0.029$ ms with $u_{s,1} \approx 0.90 \times 10^{-5}$ mm, $t_{s,2} \approx 0.035$ ms with $u_{s,2} \approx 1.05 \times 10^{-5}$ mm, $t_{s,3} \approx 0.042$ ms with $u_{s,3} \approx 1.15 \times 10^{-5}$ mm and $t_{s,4} \approx 0.048$ ms with $u_{s,4} \approx 1.20 \times 10^{-5}$ mm. After the first wave onset, the signal exhibits an artificial increase in amplitude, implying a nonphysical growth of mechanical energy in a dissipative system. This effect does not reflect the material response but results from wave superposition due to reflections at the right boundary of the finite computational domain.*

peak corresponding to the instant at which the propagating wave reaches the observation point. This step is crucial for the evaluation of both the time of flight (TOF) and the amplitude attenuation.

For this reason, it is worth discussing in detail the adopted peak-detection strategy. Unlike the purely elastic case, dispersive and dissipative media exhibit a more complex wave response. In such media, the recorded displacement signals may present multiple oscillations, progressive amplitude decay, and small numerical fluctuations induced by the discretization in space and time. As a consequence, simple peak-picking approaches-such as selecting the first local maximum or the absolute maximum-may lead to ambiguous or inconsistent results, especially when comparing simulations performed with different mesh resolutions or time-step sizes.

For this reason, a dedicated post-processing procedure has been developed to identify the physically meaningful wave peaks at both the actuator and sensor locations. The adopted strategy consists of the following steps.

4.5.1 Positive-peak filtering

First, only positive local maxima of the displacement signal are considered. This choice avoids ambiguities associated with phase inversion and ensures consistency between actuator and sensor signals. An equivalent procedure could be formulated by selecting only negative local minima; therefore, this criterion represents a conventional choice and does not affect the physical interpretation of the results. A peak is retained only if its amplitude exceeds a prescribed fraction of the maximum signal amplitude, according to

$$u(t_p) \geq \text{frac} \cdot u_{\max}, \tag{4.20}$$

where t_p are the instants of time of the selected peak candidates and frac $\in (0, 1)$ is a user-defined threshold. This filtering step effectively removes low-amplitude oscillations and numerical noise. where t_p denotes the time instants of the selected peak candidates and frac $\in (0, 1)$ is a user-defined threshold. In the present simulations, a relatively high threshold is adopted, with frac ≈ 0.5. Figure 4.11 illustrates the time history of the sensor displacement $u_s(t)$ at $x_s = 100$ mm for the viscous model. Only positive local maxima exceeding a user-defined threshold frac $u_{\max}$ are retained as candidate peaks. Figure 4.11 also highlights the final peak selected for the estimation of phase velocity and attenuation, based on the selection criteria described in the following sections. This representation facilitates a direct comparison between the present results and those discussed subsequently. In the end, Table 4.3 summarizes the time instants and the amplitudes of all candidate peaks above.

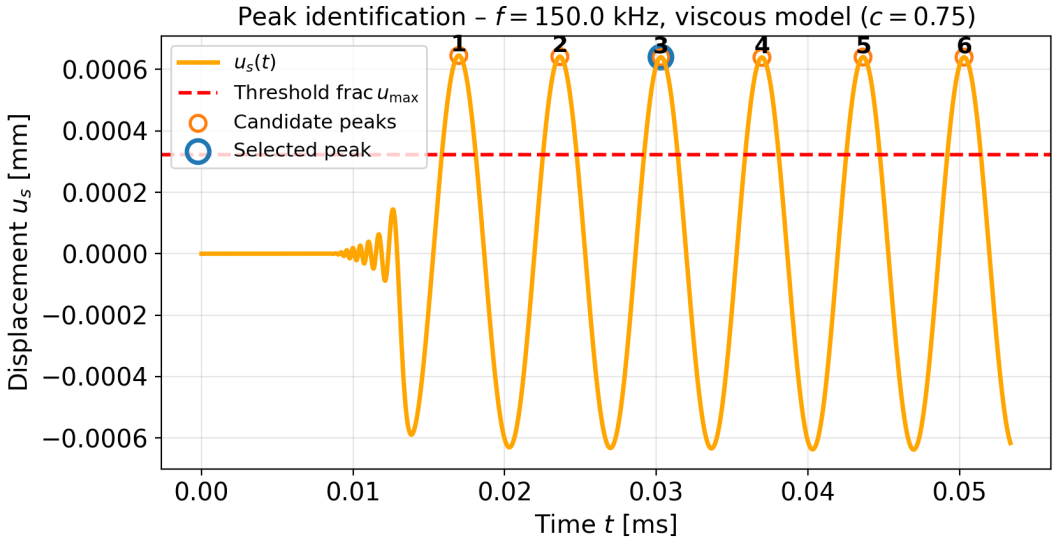

Figure 4.11: *Peak identification in the time domain for the viscous model ($c \neq 0$, $c_1 = 0$) at frequency $f = 150$ kHz. Simulation parameters: $c = 0.75$ g/(mm · ms), $c_1 = 0$ g · mm/ms, $\rho = 1.780 \times 10^{-3}$ g/mm^3, $k_1 = 100 \times 10^3$ g·mm/ms^2, $L = 200$ mm, $x_s = 100$ mm. Candidate positive peaks exceeding the threshold* frac $u_{\max}$ *are marked with circles, while the selected reference peak is highlighted in blue. Peak indices correspond to the ordered list reported in Table 4.3.*

Peak ID	t_{peak} [ms]	u_{peak} [mm]
1	0.016973	6.45×10^{-4}
2	0.023640	6.42×10^{-4}
3	0.030306	6.40×10^{-4}
4	0.036973	6.39×10^{-4}
5	0.043642	6.40×10^{-4}
6	0.050308	6.40×10^{-4}

Table 4.3: *Candidate displacement peaks above the selection threshold for the viscous model ($c = 0.75$ g/(mm · ms), $c_1 = 0$), recorded at the sensor location $x_s = 100$ mm for frequency $f = 150$ kHz. The peak IDs correspond to the peaks highlighted in Fig. 4.11.*

4.5.2 Statistical peak selection

The remaining candidate peaks typically form a cluster corresponding to successive oscillations of the same propagating wave packet. To identify the most representative peak, a robust statistical procedure is applied, following well-established principles of robust estimation and statistical signal processing[92;93].

The amplitudes of the candidate peaks are assumed to follow an approximately Gaussian distribution, as commonly observed in narrow-band wave propagation problems affected by numerical noise and weak scattering[94].

Let $\{u_i\}_{i=1}^{N}$ denote the set of N candidate peak amplitudes identified above the selection threshold. An initial estimate of the central amplitude is obtained from the median:

$$\mu_0 = \text{median}(u_i), \tag{4.21}$$

which is significantly less sensitive to extreme values than the arithmetic mean, especially in the presence of outliers[92;93].

The dispersion of the peak amplitudes is initially quantified using the median absolute deviation (MAD):

$$\text{MAD} = \text{median}(|u_i - \mu_0|)\,, \tag{4.22}$$

a robust estimator of scale widely used in statistical signal analysis[95].

To obtain a statistically consistent estimate of the standard deviation under the assumption of Gaussianity, the MAD is rescaled as

$$\sigma_0 = 1.4826\,\text{MAD}, \tag{4.23}$$

where the numerical factor arises from the inverse of the 75th percentile of the standard normal distribution[92;96].

Starting from the robust initial estimates (μ_0, σ_0), the mean amplitude is refined through a Gaussian-weighted fixed-point iteration. At iteration k, a statistical weight is associated with each candidate peak,

$$w_i^{(k)} = \exp\left(-\frac{(u_i - \mu^{(k)})^2}{2\sigma_0^2}\right), \tag{4.24}$$

which corresponds to the Gaussian likelihood of observing amplitude u_i up to a normalization constant[94].

The updated estimate of the mean amplitude is then computed as

$$\mu^{(k+1)} = \frac{\sum_{i=1}^{N} w_i^{(k)} u_i}{\sum_{i=1}^{N} w_i^{(k)}}, \tag{4.25}$$

and convergence is typically achieved in a small number of iterations due to the strong down-weighting of statistically inconsistent peaks.

Once convergence is reached, the dispersion of the statistically representative peak cluster is evaluated through the weighted standard deviation

$$\sigma = \sqrt{\frac{\sum_{i=1}^{N} w_i (u_i - \mu)^2}{\sum_{i=1}^{N} w_i}}, \tag{4.26}$$

which quantifies the intrinsic variability of the physically meaningful peaks while remaining insensitive to isolated extreme values[92].

Finally, the relative probability of each candidate peak is defined as the Gaussian likelihood associated with its amplitude u_i. Under the assumption of an approximately normal distribution of peak amplitudes, the probability density function is given by[94;97]

$$p(u_i) = \frac{1}{\sqrt{2\pi}\,\sigma} \exp\left(-\frac{(u_i - \mu)^2}{2\sigma^2}\right). \tag{4.27}$$

For comparison purposes, the normalization constant is omitted and only the exponential term is retained, yielding a relative probability that provides a weight proportional to the statistical compatibility of each peak with the estimated mean amplitude μ, then we can state:

$$p(u_i) \approx \exp\left(-\frac{(u_i - \mu)^2}{2\sigma^2}\right). \tag{4.28}$$

In Tables 4.4 we summarize the value of probability density for each candidate peak for the viscous model, respectively for the strain-gradient model, calculated according equation (4.28). For the viscous model, candidate peaks are tightly clustered around the mean amplitude, resulting in comparable likelihoods.

Peak ID	$p(u_i)$
1	≈ 0
2	0.013
3	0.982
4	0.282
5	0.943
6	0.982

Table 4.4: *Relative Gaussian likelihoods associated with the candidate displacement peaks for the viscous model ($c = 0.75$ g/(mm $\cdot$ ms), $c_1 = 0$), recorded at the sensor location $x_s = 100$ mm for frequency $f = 150$ kHz. The probability density is evaluated according equation (4.28). Estimated parameters: $\mu = 6.40 \times 10^{-4}$ mm, $\sigma = 6.11 \times 10^{-7}$ mm.*

The final reference peak is selected as the candidate whose amplitude is closest to μ, equivalently corresponding to the maximum value of the Gaussian likelihood. In Figures 4.12 and 4.13, the candidate peaks are redistributed according to their probability density, and both the estimated mean value and the selected peak closest to this mean are highlighted. The Gaussian distribution is shown to emphasize the statistically most probable peaks with respect to less probable ones. The Figure 4.13 represents a zoomed view of the Gaussian bell compared to the global representation shown in the previous Figure 4.12.
This procedure ensures that the chosen peak corresponds to the most probable physical event rather than to an isolated extreme value.
Once the reference displacement peak has been identified at the sensor location, it is necessary to determine the corresponding peak at the actuator. Indeed, multiple oscillation fronts are generated by the harmonic excitation, and different peaks correspond to successive wave packets traveling along the bar. Selecting inconsistent peaks at the actuator and sensor locations would lead to an erroneous estimation of both the time of flight and the associated phase velocity and attenuation.
For ensuring physical consistency, the actuator peak is therefore selected by enforcing a wavefront correspondence criterion: the actuator peak must correspond to the same oscillation index (or wavefront order) as the reference sensor peak. In practice, once the n-th reference peak is selected in the sensor signal at the time-amplitude coordinates (t_s, u_s), the n-th peak of the actuator signal is selected at the corresponding coordinates $(t_{\text{act}}, u_{\text{act}})$. This guarantees that the two peaks are associated with the same propagating wavefront, allowing a consistent definition of the time of flight as well as reliable estimates of phase velocity and attenuation. The Figure 4.14 illustrates, for viscous model, at a fixed frequency of 150 kHz, the correspondence between the actuator and sensor wavefronts associated with the selected reference peak, highlighting the consistent identification of the same propagating wave packet at the actuator and sensor

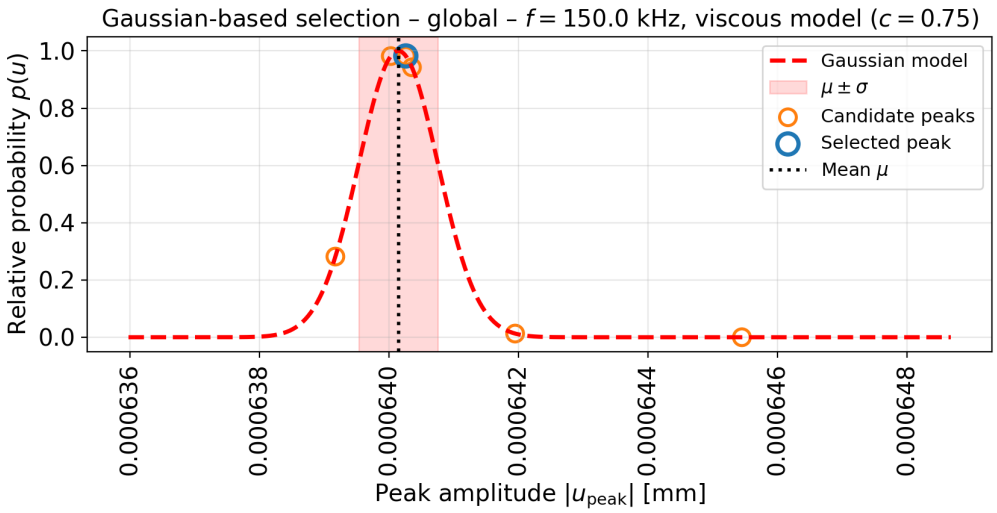

Figure 4.12: *Global view of the Gaussian-based peak selection for the viscous model ($c = 0.75$ g/(mm · ms), $c_1 = 0$), recorded at the sensor location $x_s = 100$ mm for frequency $f = 150$ kHz. Candidate peaks are redistributed according to their Gaussian likelihood. The estimated mean amplitude and dispersion are $\mu = 6.40 \times 10^{-4}$ mm and $\sigma = 6.11 \times 10^{-7}$ mm, respectively. Peaks with amplitudes far from μ exhibit negligible probability density and therefore do not influence the identification of the reference peak. The strong localization of the Gaussian distribution reflects the limited dispersion of peak amplitudes in the viscous case.*

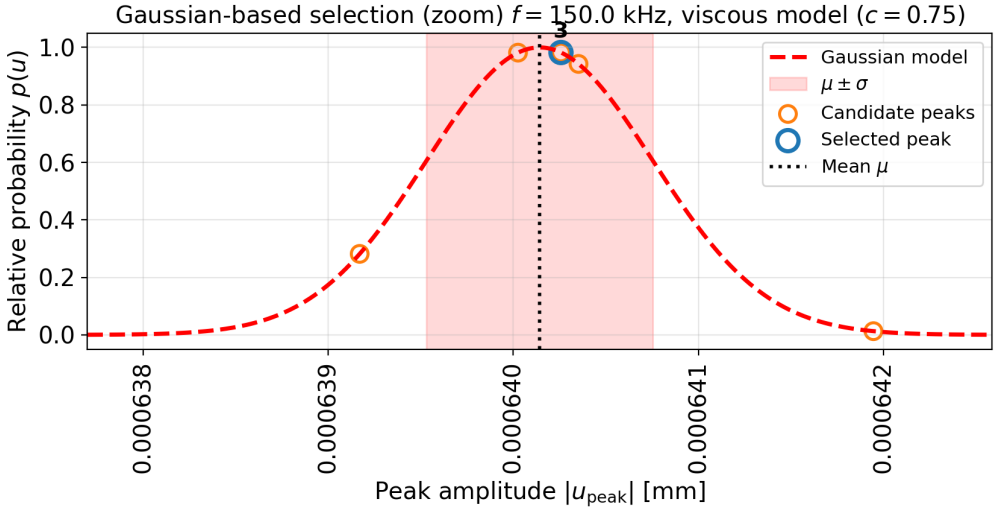

Figure 4.13: *Zoomed view of Fig. 4.12, focusing on the region of maximum probability density. The dashed red curve represents the Gaussian likelihood given by Eq. (4.28), while the shaded band highlights the interval $\mu \pm \sigma$. The selected reference peak (Peak ID 3) corresponds to the candidate with maximum statistical compatibility with the estimated mean amplitude.*

locations.

4.5.3 Time-of-flight and attenuation

Once a reference peak has been identified at the actuator and at each sensor location, the time of flight is computed as

$$\text{TOF} = t_s - t_{\text{act}}, \tag{4.29}$$

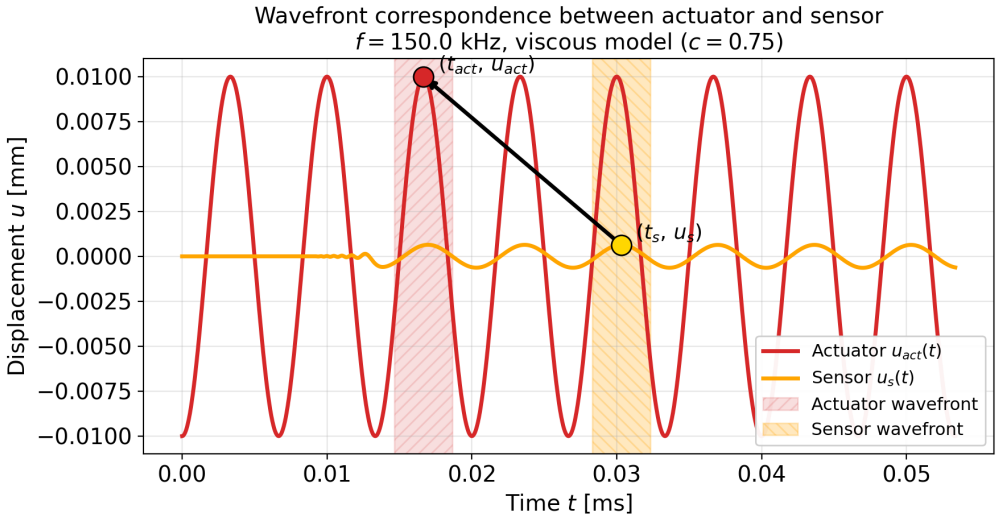

Figure 4.14: *Wavefront correspondence between actuator and sensor signals for the viscous model ($c = 0.75$ g/(mm · ms), $c_1 = 0$) at frequency $f = 150$ kHz. The actuator displacement $u_{\mathrm{act}}(t)$ and the sensor displacement $u_s(t)$ recorded at $x_s = 100$ mm are shown. The reference wavefront is identified by selecting the same oscillation order for both signals, ensuring that the actuator and sensor peaks belong to the same propagating wave packet. The shaded bands highlight the time intervals associated with the selected wavefronts for the actuator and the sensor, respectively. The black arrow emphasizes the correspondence between the two peaks. In our simulation the selected actuator peak occurs at $(t_{\mathrm{act}}, u_{\mathrm{act}}) = (0.01697\ \mathrm{ms}, 9.99 \times 10^{-3}\ \mathrm{mm})$, while the corresponding sensor peak is located at $(t_s, u_s) = (0.03031\ \mathrm{ms}, 6.40 \times 10^{-4}\ \mathrm{mm})$.*

where t_{act} and t_s denote the peak times at the actuator and sensor, respectively. The FEM phase velocity is computed from the time of flight between actuator and sensor as

$$v_p^{\mathrm{FEM}} = \frac{x_s}{\mathrm{TOF}}, \tag{4.30}$$

where x_s is the sensor position and TOF is measured time delay according equation (4.29). Similarly, the attenuation coefficient is evaluated from the logarithmic decay of the peak amplitudes between the actuator and the sensor according to

$$\alpha = \frac{1}{x_s - x_{\mathrm{act}}} \ln\left(\frac{u_{\mathrm{act}}}{u_s}\right), \tag{4.31}$$

where u_{act} and u_s are the displacement amplitudes of the selected peaks at the actuator and sensor locations, respectively, and $x_s - x_{\mathrm{act}}$ is the propagation distance. The statistical spread of the candidate peak amplitudes provides a natural estimate of the relative uncertainty associated with the attenuation measurement. The amplitude decay itself is obtained by integrating α along the propagation distance, leading to the exponential law (4.7).

4.6 Convergence analysis

The simulation strategy and the post-processing pipeline summarized in Figures 4.1–4.2 have been fully implemented within the `Fenics-Firedrake`[98] finite element framework, combined with the `Irksome` library for high-order implicit time integration.

The one-dimensional wave-propagation problem is solved using a standard continuous Galerkin finite element discretization in space[99], while time integration is performed by implicit Runge–Kutta (IRK) schemes, including the Backward Euler method[82;100]. The spatial discretization

employs linear one-dimensional elements, resulting in a first-order Continuous Galerkin approximation of the displacement field.
Once, for each simulation, the numerical solver produces the complete time histories of the displacement field at the actuator location and at a set of virtual sensor positions along the bar, these signals are stored without any filtering or peak selection, thereby preserving the full numerical waveform generated by the FEM solver. The post-processing stage, described in detail in the previous subsections, is then applied to the raw time histories in order to identify the physically meaningful displacement peaks at both the actuator and sensor locations. From these peaks, the time of flight is computed and subsequently used to estimate the phase velocity and the attenuation of the propagating wave. The analytical solution of the one-dimensional dissipative bar provides an exact reference against which the numerical results are compared.
In order to ensure that the numerical solution is verified by the analytical response, an h-convergence analysis is performed. Since the analytical model represents the exact reference solution, the objective of the convergence study is to demonstrate the monotonous convergence in time and space. We do the analysis by decreasing the time step and element size. When the numerical error becomes negligibly small, the FEM model is considered sufficiently accurate and the corresponding discretization parameters can be adopted for the subsequent two-dimensional simulations. Temporal convergence is assessed by refining the time step Δt, which in the numerical model is defined as

$$\Delta t = \frac{t_{\text{pulse}}}{N_{\text{ti}}}, \tag{4.32}$$

where t_{pulse} denotes the excitation pulse duration (i.e., the reciprocal of the excitation frequency) and $N_{\text{ti}} \in \mathbb{N}$ is an integer refinement parameter controlling the temporal discretization. Increasing N_{ti} reduces the time step, leading to a more accurate temporal integration at the expense of increased computational cost. Temporal convergence is achieved when the error is less than a chosen tolerance value.
Spatial convergence concerns the finite element mesh used to discretize the one-dimensional computational domain $\Omega = [0, L]$, which is partitioned into N_{el} elements of characteristic size

$$m = \frac{L}{N_{\text{el}}}. \tag{4.33}$$

To accurately capture wave propagation phenomena, the mesh must adequately resolve the wavelength λ. A common guideline in computational wave mechanics [101;102] states that at least ten elements per wavelength are required to limit numerical dispersion, leading to the condition

$$m \leq \frac{\lambda}{10}. \tag{4.34}$$

In the present simulations, the smallest wavelength is approximately 10 mm, implying that the spatial discretization must employ an element size not exceeding 1 mm in order to satisfy the adopted resolution criterion. In the FEM, unknowns are approximated by values at nodes in space created by the discretization. The space discretization is utilized by the Galerkin procedure where the unknown and test functions are chosen from the same Hilbertian Sobolev space. We use continuous elements with linear element formulation

$$u(x,t) \approx \sum_{i=1}^{n} N_i(x)\, u_i(t), \tag{4.35}$$

where $N_i(x)$ are the element shape functions and $u_i(t)$ are the nodal displacement values. By progressively refining the number of elements N_{el}, numerical dispersion is reduced and the FEM solution monotonously converges to the analytical reference response, at the cost of increased computational effort. Similarly to the temporal analysis, spatial convergence is confirmed when the error is below a given threshold value.

4.7 1D FEM viscous model calibration: results

4.7.1 Time-domain convergence at fixed frequency

The convergence properties of the one-dimensional FEM model are assessed by direct comparison with the analytical solution of the dissipative model. Figures 4.15 and 4.16 and Tables 4.5–4.11 summarize the numerical results obtained at the sensor location $x_s = 100$ mm, for frequency range between 150 kHz and 1,000 kHz and constitutive parameters $c = 0.75$, and $c_1 = 0$.
Specifically, Figs. 4.15 and 4.16 show the FEM and analytical displacement time histories at the sensor position for increasing levels of temporal and spatial refinement. For coarse discretizations, a visible phase lag and amplitude mismatch are observed. As the time step Δt is reduced and the mesh is refined, the FEM waveform converges monotonically the analytical reference, becoming almost indistinguishable in both phase and amplitude. This qualitative observation confirms the strength of the FEM by using Lagrange elements with a compact support as the element formulation. Therefore, it is possible to estimate the numerical error of the chosen mesh size and time step. In the following, we provide more rigorous and quantitative about how to exploit this monotonous convergence behaviour, focusing specifically on phase velocity accuracy and amplitude decay.

4.7.2 Frequency-dependent convergence analysis

In addition to the time- and space-convergence analyses discussed above, the accuracy of the one-dimensional FEM dissipative model is further investigated by varing frequency. The simulator is run over a range of excitation frequencies for multiple combinations of spatial and temporal discretization parameters, with the number of finite elements N_{el} varying between 100 and 800 and the temporal subdivision factor N_{ti} ranging from 100 up to 12,800.
For each simulation, the phase velocity and the amplitude decay are extracted at the sensor location $x_s = 100$ mm and compared against the corresponding analytical predictions. This procedure allows the frequency-dependent numerical errors in both phase velocity and attenuation to be quantified as functions of the spatial and temporal resolution. The errors for the FEM data are calculated as:

$$\varepsilon_{v_p} = \frac{\left| v_p^{\mathrm{FEM}} - v_p^{\mathrm{ANA}} \right|}{v_p^{\mathrm{ANA}}}, \tag{4.36}$$

for phase velocity, and

$$\varepsilon_A = \frac{\left| \left(A(x_s)/A_0\right)^{\mathrm{FEM}} - \left(A(x_s)/A_0\right)^{\mathrm{ANA}} \right|}{\left(A(x_s)/A_0\right)^{\mathrm{ANA}}} \tag{4.37}$$

for amplitude decay. To provide a compact quantitative measure of the overall agreement between the numerical and analytical solutions across the investigated frequency band, a global Root-Mean-Square Error (RMSE) indicator is introduced. For each excitation frequency f, the RMSE is computed as the norm of the relative errors in phase velocity and amplitude decay,

$$\mathrm{RMSE}(f) = \sqrt{\frac{\left(\varepsilon_{v_p}(f)\right)^2 + \left(\varepsilon_A(f)\right)^2}{2}}, \tag{4.38}$$

where $\varepsilon_{v_p}(f)$ and $\varepsilon_A(f)$ denote the percentage errors associated with the phase velocity and the normalized amplitude decay according equation (4.36) and (4.37) at each frequency f, respectively.

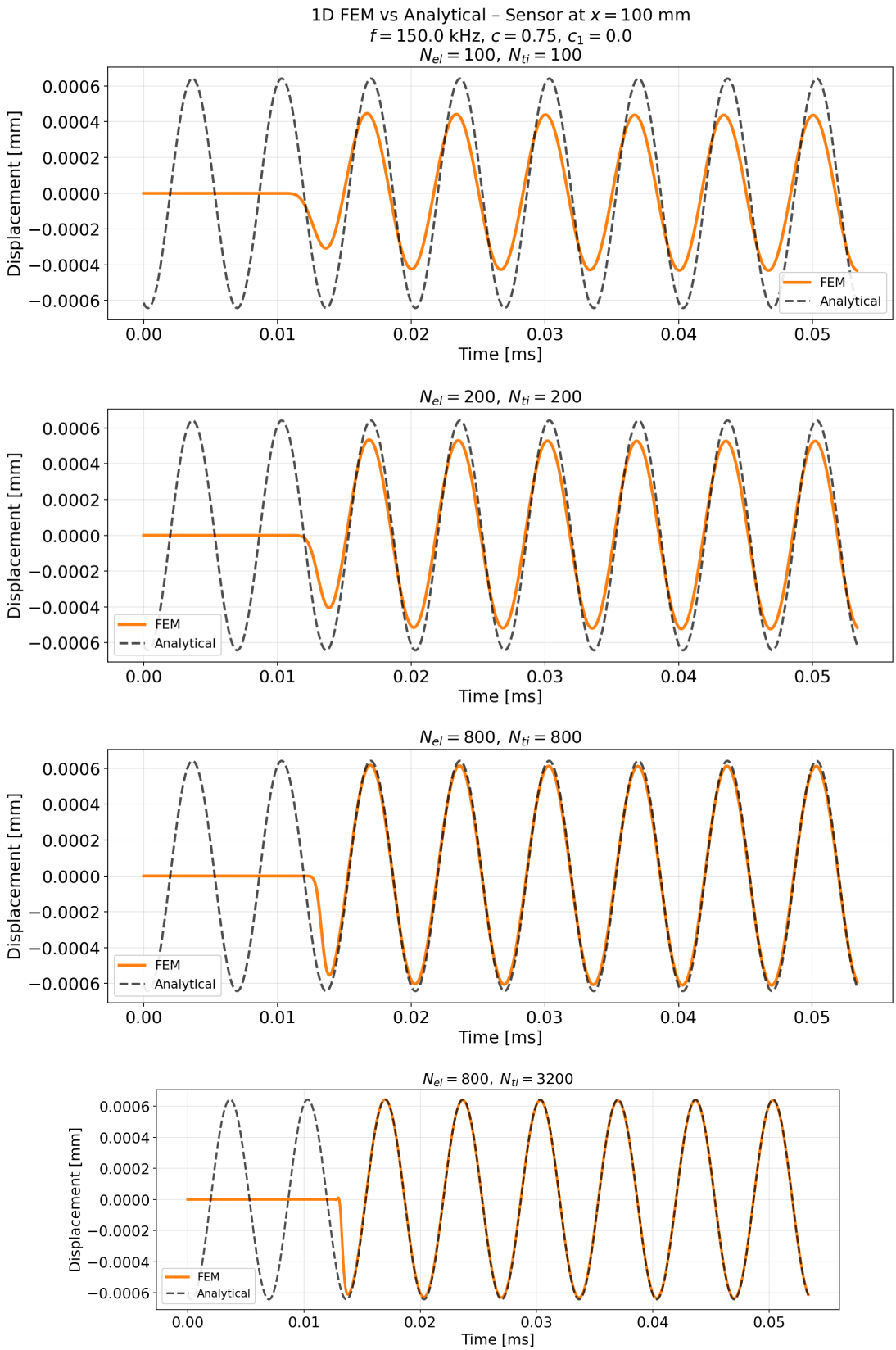

Figure 4.15: *FEM and analytical displacement time histories at the sensor location* $x_s = 100$ mm *for increasing spatial and temporal discretizations at* $f = 150$ kHz *and* $c = 0.75$. *From top to bottom:* $(N_{el}, N_{ti}) = (100, 100)$, $(200, 200)$, $(800, 800)$, *and* $(800, 3200)$. *Coarse discretizations exhibit noticeable phase lag and amplitude errors, whereas refined discretizations lead to an almost indistinguishable agreement between FEM and analytical solutions, demonstrating convergence in both phase and amplitude.*

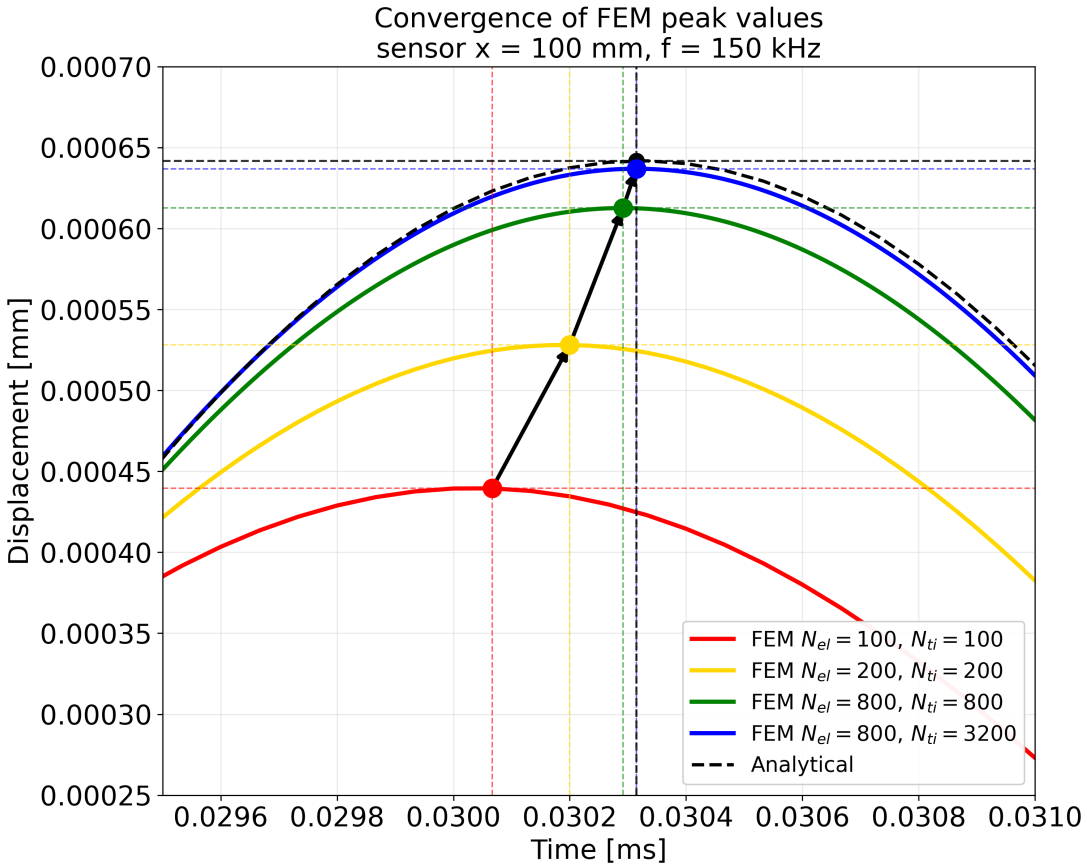

Figure 4.16: *Zoomed comparison of the displacement time histories shown in Figure 4.15, restricted to a narrow temporal window around the main peak at the sensor location* $x_s = 100$ mm *for* $f = 150$ kHz. *The FEM solutions corresponding to* $(N_{el}, N_{ti}) = (100, 100)$, $(200, 200)$, $(800, 800)$, *and* $(800, 3200)$ *are superimposed and compared with the analytical solution (dashed black curve). Markers denote the selected peak values, while dashed vertical and horizontal lines highlight the associated arrival times and amplitudes. The arrows indicate the monotonous convergence of the FEM peak response towards the analytical peak as the spatial and temporal discretization is refined. The analytical peak displacement is approximately* $u_{ana} = 6.45 \times 10^{-4}$ mm. *The FEM peak values are approximately* $u_{100,100} = 4.40 \times 10^{-4}$ mm, $u_{200,200} = 5.30 \times 10^{-4}$ mm, $u_{800,800} = 6.15 \times 10^{-4}$ mm, *and* $u_{800,3200} = 6.38 \times 10^{-4}$ mm. *These correspond to relative errors of about* 31.8%, 17.8%, 4.7%, *and* 1.1%, *respectively, providing a quantitative confirmation of the convergence observed in the full time histories.*

Moreover, a global error indicator is then obtained by averaging the frequency-dependent RMSE values over the entire frequency set $\{f_i\}_{i=1}^{N_f}$,

$$\mathrm{RMSE}_{\mathrm{global}} = \sqrt{\frac{1}{N_f} \sum_{i=1}^{N_f} [\mathrm{RMSE}(f_i)]^2}, \tag{4.39}$$

where N_f is the total number of frequencies investigated in the simulation. This indicator simultaneously accounts for numerical dispersion effects, through the phase-velocity error, and numerical dissipation effects, through the amplitude error, providing a clear and compact criterion for model calibration. As previously shown in Figure 4.16, the analytical and FEM solutions coincide in the asymptotic limit of vanishing mesh size and time step. However, in view of the intended extension of the model to two-dimensional simulations, a practical compromise between numerical accuracy and computational cost must be identified. In this context,

an error level below 1% is considered acceptable for the present viscous case.
Tables 4.5–4.11 report some representative subsets of these results for selected discretization cases, illustrating the improvement in accuracy obtained with increasing spatial and temporal refinement.

f	v_p			$A(x_s)/A_0$			RMSE
[kHz]	FEM	ANA	ε_{v_p} [±%]	FEM	ANA	ε_A [±%]	[±%]
150	7,425.743	7,322.732	± 1.407	4.379×10^{-2}	6.418×10^{-2}	± 31.77	± 22.48
250	7,552.870	7,429.940	± 1.655	3.416×10^{-2}	6.165×10^{-2}	± 44.59	± 31.55
375	7,621.951	7,465.767	± 2.092	2.691×10^{-2}	6.083×10^{-2}	± 55.77	± 39.46
500	7,716.049	7,478.595	± 3.175	2.232×10^{-2}	6.054×10^{-2}	± 63.14	± 44.70
750	8,896.797	7,487.853	± 18.82	1.722×10^{-2}	6.033×10^{-2}	± 71.46	± 52.25
1,000	8,976.661	7,491.112	± 19.83	1.451×10^{-2}	6.026×10^{-2}	± 75.93	± 55.49

Table 4.5: *Frequency-domain comparison between FEM and analytical solutions for the viscous one-dimensional model at the sensor location $x_s = 100$ mm, using a coarse discretization ($N_{el} = 100$, $N_{ti} = 100$). The phase-velocity error increases moderately with frequency, while the attenuation error grows dramatically as frequency increases. As a result, the RMSE is increasingly dominated by numerical dissipation at high frequencies, which is consistent with the expected behaviour when the wavelength λ approaches the mesh size. The corresponding global convergence indicator is* $\mathrm{RMSE}_{\mathrm{global}} = \pm 42.56\%$.

f	v_p			$A(x_s)/A_0$			RMSE
[kHz]	FEM	ANA	ε_{v_p} [±%]	FEM	ANA	ε_A [±%]	[±%]
150	7,371.007	7,322.732	± 0.659	5.270×10^{-2}	6.418×10^{-2}	± 17.90	± 12.66
250	7,473.842	7,429.940	± 0.591	4.496×10^{-2}	6.165×10^{-2}	± 27.08	± 19.15
375	7,515.030	7,465.767	± 0.660	3.858×10^{-2}	6.083×10^{-2}	± 36.58	± 25.87
500	7,547.170	7,478.595	± 0.917	3.369×10^{-2}	6.054×10^{-2}	± 44.35	± 31.37
750	7,618.080	7,487.853	± 1.739	2.674×10^{-2}	6.033×10^{-2}	± 55.67	± 39.39
1,000	7,707.129	7,491.112	± 2.884	2.223×10^{-2}	6.026×10^{-2}	± 63.11	± 44.67

Table 4.6: *Frequency-domain comparison between FEM and analytical solutions for the viscous one-dimensional model at the sensor location $x_s = 100$ mm, using an intermediate discretization ($N_{el} = 200$, $N_{ti} = 200$). The phase-velocity error increases moderately with frequency, indicating controlled numerical dispersion. In contrast, the amplitude-decay error grows significantly as frequency increases, revealing the progressive dominance of numerical dissipation when the wavelength approaches the spatial discretization scale. As a consequence, the RMSE is increasingly governed by attenuation errors at high frequencies, in agreement with classical dispersion–dissipation theory for wave propagation problems. The corresponding global convergence indicator is* $\mathrm{RMSE}_{\mathrm{global}} = \pm 29.85\%$.

Overall, the results demonstrate that, over the entire investigated frequency range, the finite element (FEM) solutions converge towards the corresponding analytical predictions, as the numerical errors decrease with increasing spatial and temporal discretization. At the same time, the numerical errors are observed to increase with frequency, indicating that discretization settings that are adequate at low frequencies (e.g. $f = 150$ kHz) become insufficient as higher-frequency wave components are considered.
This behaviour is consistent with well-established findings in the literature, which report that high-frequency waves are particularly sensitive to numerical dispersion and amplitude errors,

f	v_p			$A(x_s)/A_0$			RMSE
[kHz]	FEM	ANA	ε_{v_p} [±%]	FEM	ANA	ε_A [±%]	[±%]
150	7,343.941	7,322.732	± 0.290	5.819×10^{-2}	6.418×10^{-2}	± 9.33	± 6.60
250	7,451.565	7,429.940	± 0.291	5.242×10^{-2}	6.165×10^{-2}	± 14.97	± 10.59
375	7,485.030	7,465.767	± 0.258	4.797×10^{-2}	6.083×10^{-2}	± 21.15	± 14.95
500	7,499.063	7,478.595	± 0.274	4.426×10^{-2}	6.054×10^{-2}	± 26.89	± 19.01
750	7,524.454	7,487.853	± 0.489	3.832×10^{-2}	6.033×10^{-2}	± 36.47	± 25.79
1,000	7,548.594	7,491.112	± 0.767	3.357×10^{-2}	6.026×10^{-2}	± 44.29	± 31.32

Table 4.7: *Frequency-domain comparison between FEM and analytical solutions for the one-dimensional dissipative model at the sensor location $x_s = 100$ mm, using an intermediate discretization ($N_{el} = 400$, $N_{ti} = 400$). The phase-velocity error remains below 1% over the entire frequency range, while the attenuation error increases monotonically with frequency. As a consequence, the RMSE is progressively dominated by amplitude discrepancies at higher frequencies. The corresponding global convergence indicator is* $\mathrm{RMSE}_{\mathrm{global}} = \pm 19.95\%$.

f	v_p			$A(x_s)/A_0$			RMSE
[kHz]	FEM	ANA	ε_{v_p} [±%]	FEM	ANA	ε_A [±%]	[±%]
150	7,334.963	7,322.732	± 0.167	6.124×10^{-2}	6.418×10^{-2}	± 4.58	± 3.24
250	7,437.709	7,429.940	± 0.105	5.683×10^{-2}	6.165×10^{-2}	± 7.83	± 5.54
375	7,473.842	7,465.767	± 0.108	5.394×10^{-2}	6.083×10^{-2}	± 11.33	± 8.01
500	7,486.431	7,478.595	± 0.105	5.154×10^{-2}	6.054×10^{-2}	± 14.86	± 10.51
750	7,498.125	7,487.853	± 0.137	4.757×10^{-2}	6.033×10^{-2}	± 21.15	± 14.95
1,000	7,506.803	7,491.112	± 0.209	4.410×10^{-2}	6.026×10^{-2}	± 26.82	± 18.96

Table 4.8: *Frequency-domain comparison between FEM and analytical solutions for the viscous one-dimensional model at the sensor location $x_s = 100$ mm, using a refined discretization ($N_{el} = 800$, $N_{ti} = 800$). The phase-velocity error remains below 0.25% over the entire frequency range, indicating a strong reduction of numerical dispersion. Conversely, the amplitude-decay error increases with frequency, reflecting the progressive influence of numerical dissipation as the wavelength approaches the mesh size. The resulting RMSE is therefore increasingly governed by attenuation errors at high frequencies. The corresponding global convergence indicator is* $\mathrm{RMSE}_{\mathrm{global}} = \pm 11.54\%$.

thereby imposing increasingly stringent requirements on both spatial and temporal discretizations[103;104]. The convergence analysis further reveals that the attenuation coefficient converges in a slower rate than the phase velocity. We emphasize that the displacement shows the expected monotonous convergence; however, attenuation and phase velocity are computed in a postprocessing step from the displacement solution. Therefore, we report a convergence herein different than the FEM convergence. Fortunately, a clear trend is visible that the errors of phase velocity and attenuation decrease by increasing the solution accuracy. Yet the attenuation error remains particularly high, even though the displacement accuracy is below 1%. This behaviour is particularly evident at the highest excitation frequencies considered, where attenuation errors remain non-negligible even when the phase-velocity estimates have already converged.
For this reason, special attention is devoted to the analysis of attenuation accuracy at 1,000 kHz. Then, from inspection of Tables 4.5 - 4.11 it becomes fairly intuitive to identify the combination $(N_{el}, N_{ti}) = (800, 12800)$ as a suitable choice to ensure negligible errors, remaining below the 1% threshold even for the most demanding conditions for the viscous model.
However, while such conclusions can be readily inferred from a qualitative inspection of the

f	v_p			$A(x_s)/A_0$			RMSE
[kHz]	FEM	ANA	ε_{v_p} [±%]	FEM	ANA	ε_A [±%]	[±%]
150	7,324.889	7,322.732	± 0.029	6.366×10^{-2}	6.418×10^{-2}	± 0.81	± 0.57
250	7,432.872	7,429.940	± 0.039	6.052×10^{-2}	6.165×10^{-2}	± 1.84	± 1.30
375	7,469.190	7,465.767	± 0.046	5.920×10^{-2}	6.083×10^{-2}	± 2.68	± 1.90
500	7,482.930	7,478.595	± 0.058	5.836×10^{-2}	6.054×10^{-2}	± 3.61	± 2.55
750	7,496.252	7,487.853	± 0.112	5.723×10^{-2}	6.033×10^{-2}	± 5.13	± 3.63
1,000	7,505.218	7,491.112	± 0.188	5.638×10^{-2}	6.026×10^{-2}	± 6.43	± 4.55

Table 4.9: *Frequency-domain comparison between FEM and analytical solutions for the viscous one-dimensional model at the sensor location $x_s = 100$ mm, obtained using the final selected discretization ($N_{el} = 800$, $N_{ti} = 3200$). The corresponding global root–mean–square error is $\mathrm{RMSE}_{\mathrm{global}} = \pm 2.77\%$. The phase-velocity error further decreases with respect to the discretization with $N_{ti} = 800$, although only marginally, indicating that temporal convergence has essentially been achieved. In contrast, for the attenuation coefficient, errors of up to 6% are still observed at high frequencies, highlighting the strong sensitivity of attenuation estimates and the need for even finer temporal and/or spatial discretizations in order to reach a level of error negligibility comparable to that achieved for the phase velocity.*

f	v_p			$A(x_s)/A_0$			RMSE
[kHz]	FEM	ANA	ε_{v_p} [%]	FEM	ANA	ε_A [%]	[%]
150	7,323.213	7,322.732	±0.007	6.408×10^{-2}	6.418×10^{-2}	±0.155	±0.110
250	7,431.836	7,429.940	±0.026	6.116×10^{-2}	6.165×10^{-2}	±0.809	±0.572
375	7,468.260	7,465.767	±0.033	6.012×10^{-2}	6.083×10^{-2}	±1.161	±0.821
500	7,482.405	7,478.595	±0.051	5.957×10^{-2}	6.054×10^{-2}	±1.597	±1.130
750	7,495.901	7,487.853	±0.107	5.902×10^{-2}	6.033×10^{-2}	±2.165	±1.533
1,000	7,504.954	7,491.112	±0.185	5.874×10^{-2}	6.026×10^{-2}	±2.518	±1.785

Table 4.10: *Frequency-domain comparison between FEM and analytical solutions for the viscous one-dimensional model at the sensor location $x_s = 100$ mm, obtained using the final selected discretization ($N_{el} = 800$, $N_{ti} = 6{,}400$). The corresponding global root–mean–square error is $\mathrm{RMSE}_{\mathrm{global}} = \pm 1.14\%$. Across the investigated frequency range, the FEM phase-velocity estimates exhibit relative errors well below 0.2%, indicating that numerical dispersion is effectively controlled. In contrast, attenuation errors increase with frequency, reaching values of about 2.5% at 1,000 kHz, which confirms the higher sensitivity of attenuation to temporal discretization.*

tabulated data and graphical results, a more systematic and quantitative criterion is required in order to identify combinations of spatial and temporal discretization parameters that guarantee a prescribed level of accuracy.

To this end, all computed simulations are collected into a three-dimensional representation, as shown in Fig. 4.17, where the numerical error is expressed as a function of both the number of spatial elements N_{el} and the number of time steps N_{ti}. Within this framework, the discretization parameters span a two-dimensional plane (N_{el}, N_{ti}), while the corresponding error magnitude defines a surface embedded in the three-dimensional space.

For each excitation frequency, the discrete error values obtained from the numerical simulations are interpolated over the (N_{el}, N_{ti}) plane to obtain a continuous approximation of the error surface. In practice, given a set of discrete samples $\{(N_{el}^k, N_{ti}^k, \varepsilon^k)\}$, the error at an arbitrary

f	v_p			$A(x_s)/A_0$			RMSE
[kHz]	FEM	ANA	ε_{v_p} [±%]	FEM	ANA	ε_A [±%]	[±%]
150	7,322.375	7,322.732	± 0.005	6.429×10^{-2}	6.418×10^{-2}	± 0.173	± 0.123
250	7,431.318	7,429.940	± 0.019	6.148×10^{-2}	6.165×10^{-2}	± 0.287	± 0.203
375	7,468.028	7,465.767	± 0.030	6.059×10^{-2}	6.083×10^{-2}	± 0.390	± 0.277
500	7,482.230	7,478.595	± 0.049	6.019×10^{-2}	6.054×10^{-2}	± 0.576	± 0.409
750	7,495.667	7,487.853	± 0.104	5.994×10^{-2}	6.033×10^{-2}	± 0.645	± 0.462
1,000	7,504.866	7,491.112	± 0.184	5.995×10^{-2}	6.026×10^{-2}	± 0.500	± 0.377

Table 4.11: *Frequency-domain comparison between FEM and analytical solutions for the viscous one-dimensional model at the sensor location $x_s = 100$ mm, obtained using the final selected discretization ($N_{el} = 800$, $N_{ti} = 12{,}800$). Both phase-velocity and amplitude-decay errors remain below 1% over the entire frequency range. The corresponding global root–mean–square error is* $\mathrm{RMSE}_{\mathrm{global}} = \pm 0.33\%$.

point (N_{el}, N_{ti}) is approximated by a piecewise linear interpolation of the form

$$\varepsilon(N_{el}, N_{ti}) \;\approx\; \sum_k w_k(N_{el}, N_{ti})\, \varepsilon^k, \tag{4.40}$$

where the weights w_k are determined by linear interpolation over the triangulation of the (N_{el}, N_{ti}) plane and the subscript k denotes the index of a discrete simulation case, corresponding to a specific combination of excitation frequency and spatial-temporal discretization parameters (N_{el}, N_{ti}). This procedure yields a continuous error surface that provides a global view of the combined influence of spatial and temporal refinement on the numerical accuracy.
Within this three-dimensional error landscape, admissible discretizations can be identified geometrically by introducing the threshold error plane corresponding to $\varepsilon = 1\%$. The intersection between the interpolated error surface and the threshold plane defines a curve in the (N_{el}, N_{ti}) plane, which represents the boundary separating acceptable and unacceptable discretization choices for each frequency.
Discretization pairs yielding acceptable accuracy are those contained within the wedge-shaped region bounded by the RMSE = 1% threshold curve, as illustrated in the bottom panel of the Figure 4.17 . Configurations inside this region satisfy the refinement requirements in both space and time, whereas points outside the wedge do not meet the accuracy criterion and must be discarded. This construction therefore provides an objective and frequency-dependent criterion for selecting suitable combinations of N_{el} and N_{ti}, replacing purely qualitative assessments with a geometrically well-defined admissible region.
In principle, for each excitation frequency, a specific combination of spatial and temporal discretization parameters could be identified in order to reduce the numerical error below a prescribed acceptability threshold.
Discretization pairs yielding acceptable accuracy are those contained within the wedge-shaped region bounded by the RMSE = 1% threshold curve, as illustrated in the bottom panel of Figure 4.17. Configurations located inside this region satisfy the refinement requirements in both space and time, whereas points lying outside the wedge–particularly on its left-hand side–do not meet the prescribed accuracy criterion and must therefore be discarded. This construction provides an objective and frequency-dependent criterion for selecting suitable combinations of N_{el} and N_{ti}, replacing purely qualitative assessments with a geometrically well-defined admissible region.
In principle, for each excitation frequency, a specific combination of spatial and temporal discretization parameters could be identified in order to reduce the numerical error below a prescribed acceptability threshold. In order to formalize this selection procedure, the RMSE = 1%

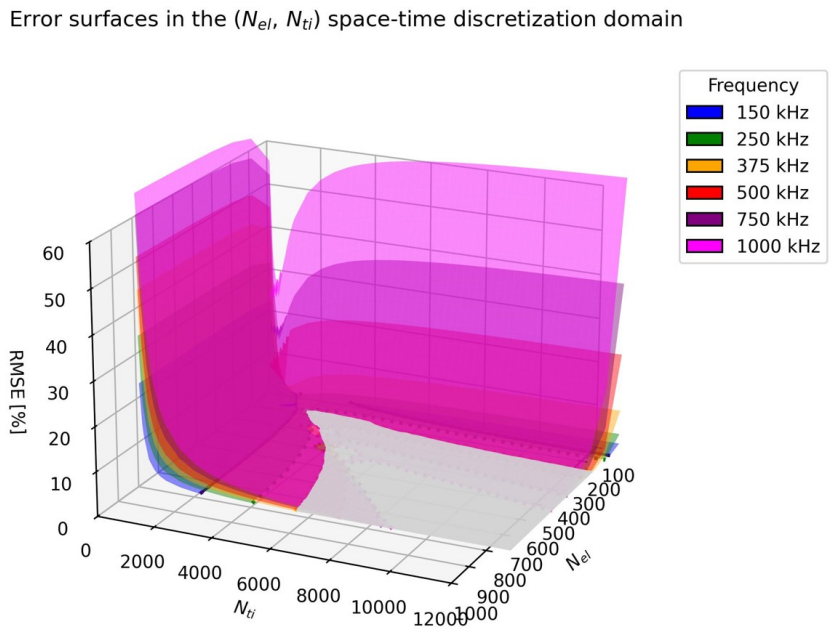

((a))

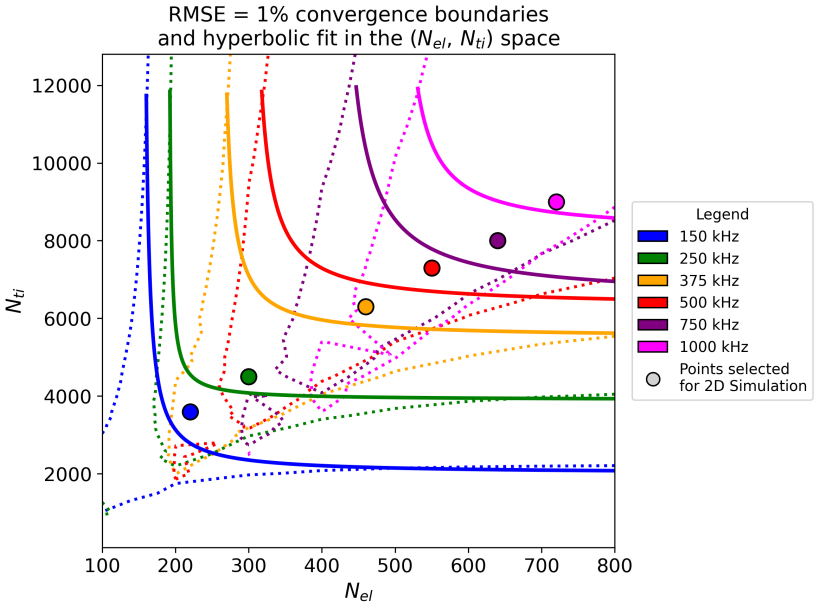

((b))

Figure 4.17: *Error analysis in the (N_{el}, N_{ti}) space–time discretization domain for different excitation frequencies. (**a**) Three-dimensional surfaces of the root-mean-square error (RMSE) as a function of the number of spatial elements N_{el} and temporal subdivisions N_{ti}, shown for excitation frequencies ranging from 150 to 1,000 kHz. Each colored surface represents a fixed frequency and illustrates the coupled influence of spatial and temporal resolution on numerical accuracy. A sharp error decay is observed when both discretizations are refined, with increasingly restrictive requirements at higher frequencies. (**b**) Two-dimensional projection of the RMSE= 1% convergence boundary in the (N_{el}, N_{ti}) plane. Dashed curves denote the extracted iso-error contours for each frequency, while solid curves represent the corresponding hyperbolic fits, highlighting the inverse trade-off between spatial and temporal resolution required to achieve a prescribed accuracy. Filled markers indicate the (N_{el}, N_{ti}) pairs selected for subsequent two-dimensional simulations. Together, the two representations provide a quantitative and geometric interpretation of convergence trends and resolution constraints across frequencies.*

convergence boundaries obtained from the numerical data are approximated by frequency-dependent hyperbolic fits of the form

$$N_{ti} = N_{ti}^{(0)} + \frac{A}{N_{el} - N_{el}^{(0)}}, \tag{4.41}$$

where the parameters $N_{el}^{(0)}$, $N_{ti}^{(0)}$, and A are determined independently for each excitation frequency.

N_{el}	N_{ti}					
	150 kHz	250 kHz	375 kHz	500 kHz	750 kHz	1,000 kHz
200	3,138	5,879				
300	2,353	4,080	7,109			
400	2,209	3,994	5,960	7,293		
500	2,148	3,964	5,768	6,796	8,544	
600	2,115	3,948	5,689	6,631	7,439	9,350
700	2,094	3,939	5,646	6,548	7,110	8,775
800	2,079	3,932	5,619	6,499	6,951	8,583

Table 4.12: *Minimum temporal discretization N_{ti} required to satisfy the* RMSE = 1% *accuracy threshold as a function of the spatial discretization N_{el} and excitation frequency. The reported values correspond to points lying on the hyperbolic convergence boundaries and therefore represent the lower admissible limit of the space–time discretization.*

f [kHz]	N_{el}	N_{ti}
150	220	3,600
250	300	4,500
375	460	6,300
500	550	7,300
750	640	8,000
1,000	720	9,000

Table 4.13: *Discretization pairs effectively selected for the two-dimensional simulations. The values reported in the table are rounded discretization parameters representative of points located inside the admissible region defined by the RMSE = 1% convergence boundaries and correspond to the scatter markers shown in the bottom panel of Figure 4.17.*

The resulting hyperbolic relations defining the convergence boundaries are:

$$\begin{aligned}
150 \text{ kHz:} \quad & N_{ti} = 2000.0 + \frac{5.121 \times 10^4}{N_{el} - 155.0}, \\
250 \text{ kHz:} \quad & N_{ti} = 3900.0 + \frac{1.979 \times 10^4}{N_{el} - 190.0}, \\
375 \text{ kHz:} \quad & N_{ti} = 5500.0 + \frac{6.435 \times 10^4}{N_{el} - 260.0}, \\
500 \text{ kHz:} \quad & N_{ti} = 6300.0 + \frac{9.925 \times 10^4}{N_{el} - 300.0}, \\
750 \text{ kHz:} \quad & N_{ti} = 6500.0 + \frac{1.737 \times 10^5}{N_{el} - 415.0}, \\
1,000 \text{ kHz:} \quad & N_{ti} = 8200.0 + \frac{1.150 \times 10^5}{N_{el} - 500.0}.
\end{aligned}$$

These expressions explicitly define the minimum temporal resolution required for a given spatial discretization in order to guarantee that the numerical error remains below the 1% threshold. Based on these convergence boundaries, representative discretization pairs are selected for subsequent two-dimensional simulations. Table 4.12 reports the *minimum* temporal discretization levels lying on the RMSE= 1% hyperbolic boundaries for each spatial resolution and frequency, defining the admissible limit of the convergence wedge.

The discretization points effectively employed in the simulations are chosen slightly inside the admissible wedge-shaped region defined by the RMSE = 1% convergence boundaries (see the scatter points in the bottom panel of Figure 4.17 and Table 4.13). The discretization parameters reported in the table are rounded values, selected to represent practical points within the admissible region rather than exact values obtained from the fitted curves. This conservative choice guarantees that the numerical error remains safely below the prescribed threshold, while avoiding unnecessary over–refinement in either space or time.

These discretization choices reflect a balanced compromise between spatial and temporal resolution and are fully consistent with the frequency-dependent convergence limits identified through the hyperbolic fitting procedure.

5 2D FEM first-gradient dissipative model: plane and circular waves

After analyzing the scalar wave propagation problem in a one-dimensional domain, the model is extended to the two-dimensional case in order to investigate the influence of geometric effects and transverse dynamics on the wave response, as for the reality.

5.1 Extension of the FEM model from 1D to 2D

5.1.1 Sample geometry

The two-dimensional computational domain is obtained by introducing a transverse direction y, with a fixed height $H = 20\,\text{mm}$, while the longitudinal dimension along the propagation direction x is kept identical to the one-dimensional configuration, with total length $L = 200\,\text{mm}$. This extension naturally allows for transverse deformations; consequently, a non-zero Poisson's ratio ($\nu = 0.3$) is adopted, whereas in the one–dimensional formulation transverse strains are suppressed and the Poisson effect is inherently absent.

5.1.2 2D spatial discretization

The spatial discretization of the two-dimensional domain is performed independently along the longitudinal and transverse directions. The domain $\Omega = [0, L] \times [0, H]$ is partitioned using a structured finite element mesh characterized by two independent discretization parameters, namely m_x and m_y, which denote the number of elements along the x and y directions, respectively.
The corresponding characteristic mesh sizes along the directions x and y are defined as:

$$\Delta x = \frac{L}{m_x}, \qquad \Delta y = \frac{H}{m_y}. \tag{5.1}$$

This anisotropic discretization allows the numerical resolution in the propagation direction to be controlled independently from that in the transverse direction. In all simulations, the discretization Δx and Δy are selected consistently with the one-dimensional reference model with Δ_x=Δ_y.

5.1.3 Boundary conditions in 2D configuration

In the one-dimensional model, the bar is free to deform exclusively along the longitudinal direction x, thus enforcing a condition of uniaxial strain. For reproducing an analogous kinematic condition in the two-dimensional setting, roller-type boundary conditions are imposed on the lower and upper faces of the domain,

$$u_y(x, 0, t) = 0, \qquad u_y(x, H, t) = 0, \tag{5.2}$$

while the longitudinal displacement component u_x remains unconstrained. These conditions suppress transverse motion while allowing longitudinal deformation, thereby promoting a predominantly one-dimensional wave propagation pattern.
At the input boundary $x = 0$, a time-dependent displacement is prescribed to model the actuator, in the same form of that used for the monodimensional simulation. Two excitation configurations are considered. In the plane-wave case, the imposed displacement is applied uniformly over the entire input boundary, thus approximating a one-dimensional plane wave. Alternatively, a circular-wave excitation is employed, in which the imposed displacement is spatially localized over a limited portion of the boundary, as implemented in the numerical code through a confined excitation function.

All remaining boundaries are left traction-free. Moreover, we specify that a plane strain assumption is adopted in this simulation, consistently with the representation of a thick specimen where out-of-plane deformations are neglected. Therefore, no independent essential boundary conditions are imposed on the first spatial derivatives. The boundary conditions prescribed in the numerical model involve only displacement components, while the terms containing spatial gradients arise naturally from the weak variational formulation as shown in the next subsection 5.1.4. Apart from these geometric and boundary-condition-related modifications, all other aspects of the formulation - including material parameters, governing equations, time integration scheme, and numerical discretization strategy - are kept identical to those adopted in the one-dimensional model.

5.1.4 Weak form for vector displacement

For the implementation of the 2D FEM procedure, first, let $\Omega \subset \mathbb{R}^2$ denote the computational domain corresponding to the specimen geometry introduced in Section 5.1.3, defined as a rectangular region of length L and height H. The boundary of the domain is denoted by $\partial\Omega$, which can be decomposed into portions where boundary conditions are prescribed. Then, we recall the one-dimensional weak form derived in Section 2.2.1 (Eq. 2.32)

$$F(u, \delta u) = \int_\Omega \Big(\rho\, \ddot{u}\, \delta u + c\, \dot{u}\, \delta u + k_1\, u'\, \delta u' + c_1\, \dot{u}'\, \delta u' \Big)\, \mathrm{d}x = 0. \tag{5.3}$$

In the two-dimensional formulation the displacement becomes a vector field $\mathbf{u} = (u_x, u_y)$ and the test function $\mathbf{v} = (v_x, v_y)$ is vector-valued as well. The strain tensor is defined as

$$\boldsymbol{\varepsilon}(\mathbf{u}) = \frac{1}{2} \left(\nabla \mathbf{u} + \nabla \mathbf{u}^T \right), \tag{5.4}$$

where $\nabla \mathbf{u}$ denotes the spatial gradient of the displacement vector, while the spatial gradient of the vector-valued test function $\nabla \mathbf{v}$ is defined accordingly. In Cartesian coordinates they read

$$\nabla \mathbf{u} = \begin{bmatrix} \dfrac{\partial u_x}{\partial x} & \dfrac{\partial u_x}{\partial y} \\ \dfrac{\partial u_y}{\partial x} & \dfrac{\partial u_y}{\partial y} \end{bmatrix}, \qquad \nabla \mathbf{v} = \begin{bmatrix} \dfrac{\partial v_x}{\partial x} & \dfrac{\partial v_x}{\partial y} \\ \dfrac{\partial v_y}{\partial x} & \dfrac{\partial v_y}{\partial y} \end{bmatrix}. \tag{5.5}$$

The appearance of $\nabla \mathbf{u}$ and $\nabla \mathbf{v}$ in the weak formulation is a direct consequence of multidimensional kinematics and does not introduce any additional modeling assumption. Applying (5.5) and the test function $\mathbf{v}$ into (5.3), the weak form used in the numerical implementation is

$$\int_\Omega \Big(\rho\, \ddot{\mathbf{u}} \cdot \mathbf{v} + c\, \dot{\mathbf{u}} \cdot \mathbf{v} + k_1\, \nabla \mathbf{u} : \nabla \mathbf{v} + c_1\, \nabla \dot{\mathbf{u}} : \nabla \mathbf{v} \Big)\, \mathrm{d}\Omega = 0. \tag{5.6}$$

The spatial discretization is performed by finite elements, whereas the time integration is carried out by means of the implicit Backward Euler scheme implemented in the IRKSOME framework within Firedrake[105–107]. The parameter c_1 is set to zero in the simulation as in 1D case.

5.1.5 Influence of geometric reflections on peak identification

As discussed in Section 4.5, the identification of phase velocity and attenuation from the numerical signals relies on a statistical peak-detection procedure applied to the time-domain response. Rather than defining a stable interval *a priori*, local maxima of the displacement signal are first detected over a sufficiently long time window after the initial transient. Among these local maxima, a representative peak amplitude is identified as the most recurrent value, using a combination of temporal averaging and standard-deviation filtering to discard sporadic or non-representative peaks.

This statistical procedure effectively selects the oscillatory regime in which the signal becomes stable. In other words, identifying the most recurrent peak corresponds to detecting a regime in which successive cycles have comparable amplitudes and phase spacing. Once this regime is identified, the corresponding peak amplitude and peak timing are used to extract attenuation and phase velocity. This strategy proved to be robust and accurate in the one-dimensional setting and in two-dimensional simulations for plane waves. For circular waves, the same approach remains valid provided that the wavelength is sufficiently large compared to the characteristic geometrical dimensions of the specimen.
The qualitative origin of the inconsistencies observed in the peak identification for circular waves in the short-wavelength regime is clarified by inspecting the spatial evolution of the wavefield at representative time instants. Figures 5.1-5.13 illustrate the displacement field for circular and plane wave excitations at increasing frequencies and selected time snapshots. For any excitation frequency, in the case of plane-wave propagation the wavefront does not undergo lateral reflections and remains perpendicular to the specimen top and bottom boundaries. As a result, no significant reflection phenomena arise, and the wavefield preserves a stable planar geometry throughout the domain, as illustrated in Figures 5.1-5.3.
At low frequencies, corresponding to wavelengths significantly larger than the specimen height ($\lambda \gg H$), circular waves propagate with a well-defined and smooth wavefront. Starting from a circular geometry at the source, the wavefront progressively expands and locally approaches a quasi-planar configuration as it propagates away from the actuator, as shown in Figures 5.4-5.8. Owing to the large wavelength, the effective angle of incidence between the increasingly planar wavefront and the lateral boundaries tends toward 90°, similarly to the plane-wave case. As a result, lateral reflections are strongly reduced.
In this regime, the influence of the lateral boundaries is weak and the wave propagates almost as if the domain were unbounded. As a consequence, the signal recorded at the sensor is dominated by a single propagating wave and successive peaks appear regularly in time. This leads to a stable oscillatory response, allowing the peak-identification procedure to provide consistent estimates of both phase velocity and attenuation.

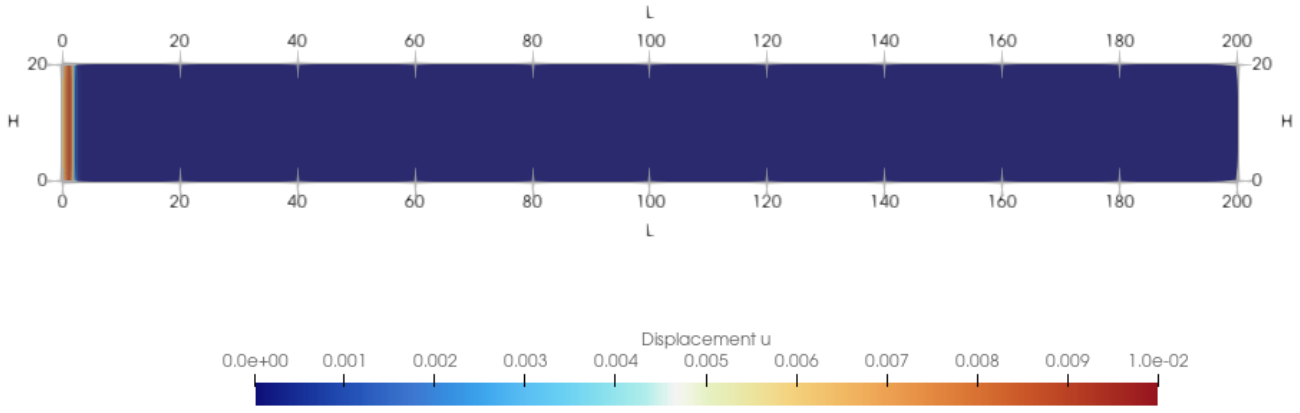

Figure 5.1: *Displacement field for plane wave propagation at* $f = 750$ kHz*, shown at time* $t = 0.0002$ ms*. The wavefront is planar and parallel to the excitation boundary, which is distributed over the entire input face of the specimen, with negligible influence from the lateral boundaries.*

As the excitation frequency increases and the wavelength becomes comparable to or smaller than the specimen height ($\lambda < H$), the wavefield undergoes a marked qualitative change. The circular wavefront progressively interacts with the lateral boundaries, giving rise to multiple reflected and diffracted components that re-enter the observation region. As shown in Figures 5.9-5.13, these interactions generate complex interference patterns and pronounced spatial amplitude

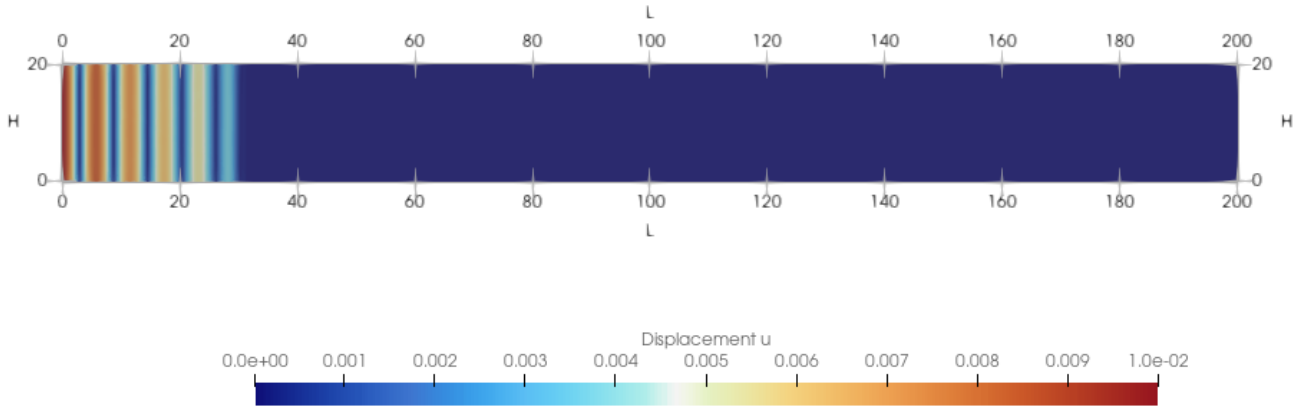

Figure 5.2: *Displacement field for plane wave propagation at* $f = 750$ kHz*, shown at time* $t = 0.003$ ms*. After the initial transient, the wave propagates through the specimen with a regular periodic pattern. The wavefront remains approximately planar and no significant lateral reflections are observed.*

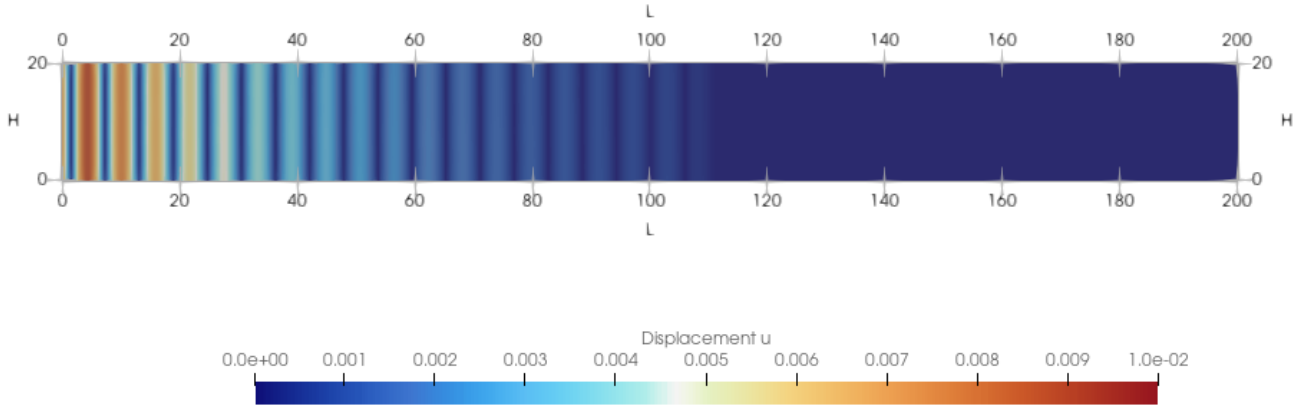

Figure 5.3: *Displacement field for plane wave propagation at* $f = 750$ kHz*, shown at time* $t = 0.0125$ ms*. The wavefront reaches the sensor position in the middle of the sample. Even at high frequency, the wavefront propagation is regular and no significant lateral reflections are observed.*

modulations.
In this regime, the wavefront no longer propagates as a single, smoothly expanding surface. Instead, reflections from the lateral boundaries act as secondary sources, locally regenerating wave energy and producing distinct focal regions where the displacement amplitude is temporarily amplified. These regenerated wave components propagate back into the interior of the domain and overlap with the direct wavefront, leading to a progressive distortion of the spatial structure of successive wave cycles. As a result, the apparent wavefront becomes fragmented and its local curvature and phase vary significantly across the observation region.
This superposition of direct and boundary-induced wave components does not disrupt the periodicity of the signal, but it alters the relative timing and spatial coherence of the propagating fronts. Consequently, peaks detected at a fixed sensor location may originate from different portions of the composite wavefield across successive cycles, rather than from a single, well-defined propagating mode.
This observation is further supported by inspection of the time–domain sensor responses re-

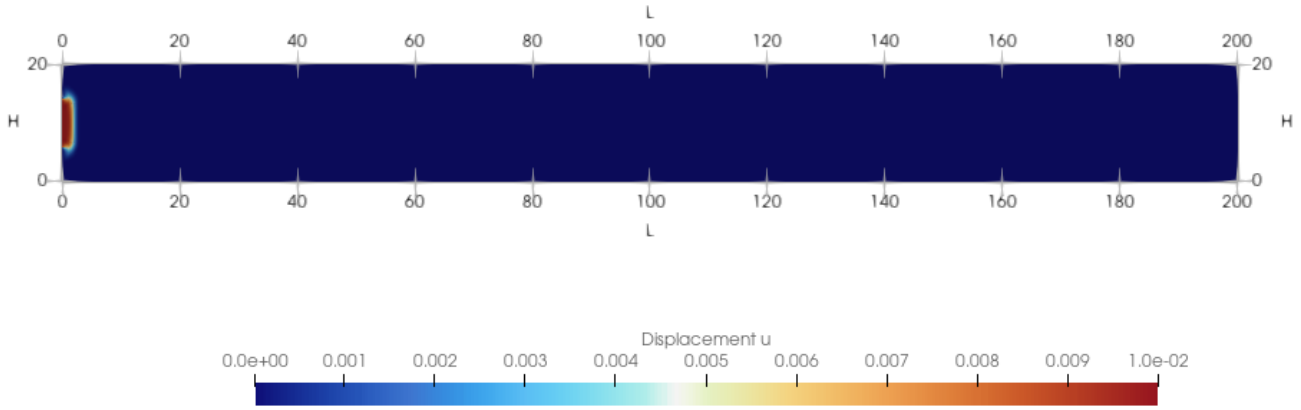

Figure 5.4: *Displacement field for circular wave propagation at* $f = 150$ kHz*, shown at time* $t = 0.0002$ ms*. The wavefront originates with a circular geometry and expands smoothly within the domain.*

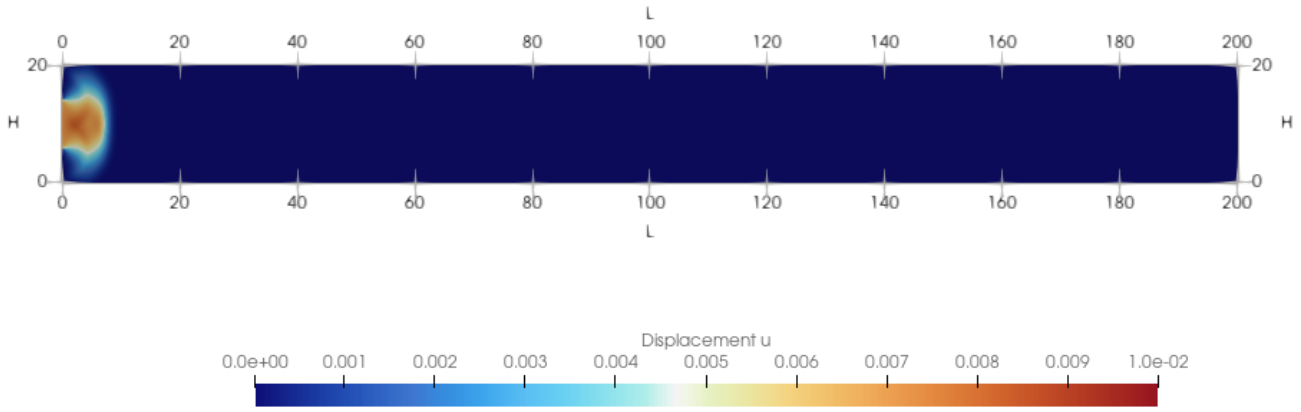

Figure 5.5: *Displacement field for circular wave propagation at* $f = 150$ kHz*, shown at time* $t = 0.0008$ms*. As the wavefront expands, it progressively assumes a locally quasi-planar shape, and the incidence angle with the lateral boundaries approaches* $90°$*, strongly reducing reflections.*

ported in Figures 5.14 - 5.19 , where the plane–wave response is compared with the circular–wave signal recorded at a fixed sensor location. While the overall oscillatory behaviour remains comparable, a systematic frequency–dependent time shift between corresponding peaks becomes distinguishable starting from 500 kHz. To characterise this effect in a simple and robust manner, a peak–to–peak time–shift analysis is performed. For each frequency, corresponding peaks of the plane and circular signals are paired by nearest–neighbour matching in time. Only peaks whose amplitude exceeds 10% of the maximum circular–wave peak are retained in order to eliminate noises echo, and the first two peaks are excluded to avoid residual transient effects.
For each frequency, the mean time shift μ and the associated deviation standard σ_μ (computed from the third peak onward) are evaluated. The resulting values are summarised in Table 5.1.
We observe that the mean absolute peak–to–peak time shift remains of the order of a few microseconds up to 375 kHz, while it increases by more than one order of magnitude starting from 500 kHz.
Importantly, this behaviour is not associated with a loss of regular oscillations nor with numerical artefacts. Both plane and circular signals remain periodic and well resolved. The observed time shift reflects a genuine geometrical propagation effect, which becomes relevant when $\lambda < H$,

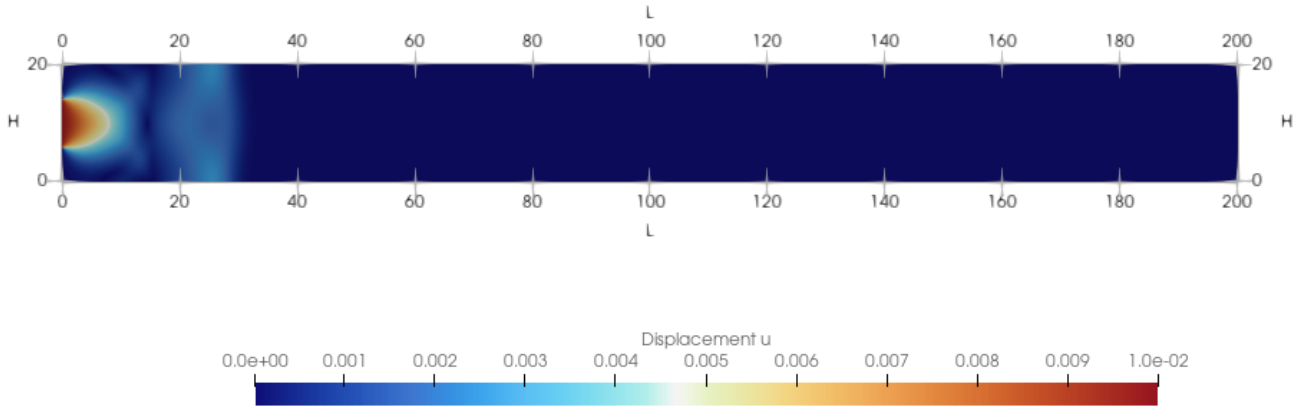

Figure 5.6: *Displacement field for circular wave propagation at $f = 150$ kHz, shown at time $t = 0.003$ ms. The wavefield is dominated by a single, smooth propagating wavefront, with minimal lateral reflections and high spatial coherence. Then, due to the large wavelength ($\lambda \gg H$), boundary interactions remain negligible.*

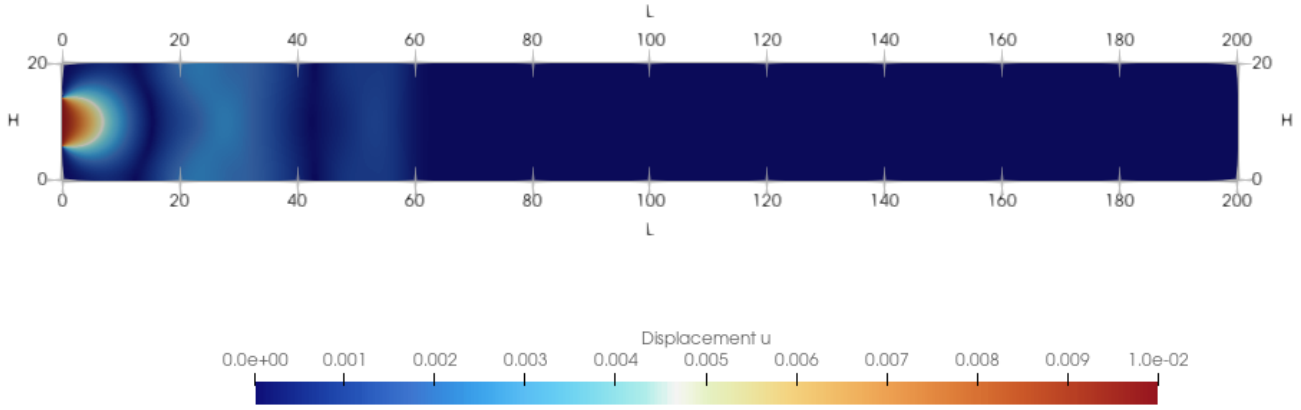

Figure 5.7: *Displacement field for circular wave propagation at $f = 150$ kHz, shown at time $t = 0.006$ ms. After the initial transient, the wave propagates with a regular periodic pattern, and successive wavefronts remain well aligned in space and time.*

Frequency [kHz]	$\langle \lvert\mu\rvert \rangle$ [ms]	$\sigma_{\lvert\mu\rvert}$ [ms]
150	6.1×10^{-6}	6.8×10^{-6}
250	6.8×10^{-6}	3.0×10^{-5}
375	8.5×10^{-6}	2.1×10^{-6}
500	7.1×10^{-5}	6.5×10^{-5}
750	2.0×10^{-4}	7.0×10^{-6}
1,000	7.2×10^{-5}	1.2×10^{-5}

Table 5.1: *Peak–to–peak time–shift statistics between circular and plane waves. The mean value $\langle \lvert\mu\rvert \rangle$ and the standard deviation $\sigma_{\lvert\mu\rvert}$ are computed on the absolute time shifts, excluding the first two peaks and considering only peaks with amplitude larger than 10% of the maximum circular–wave peak.*

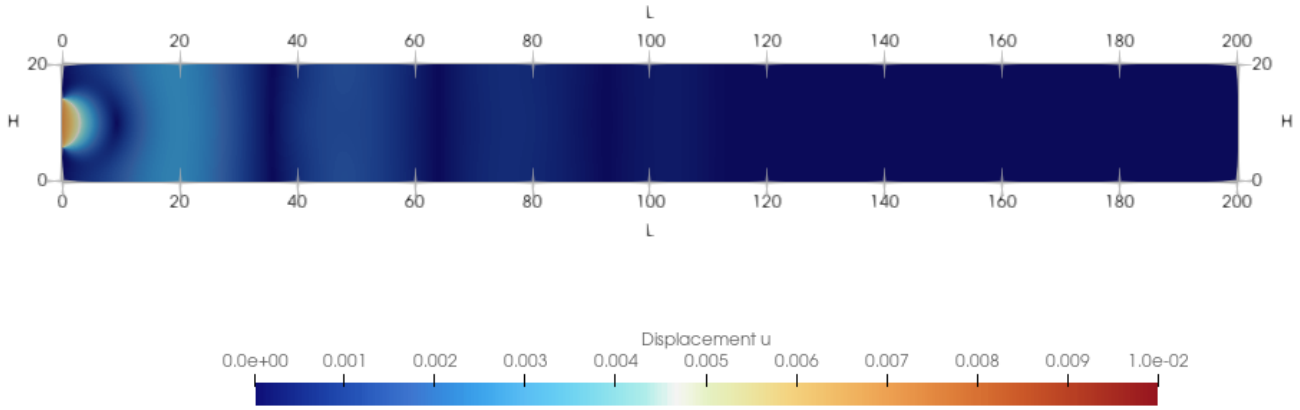

Figure 5.8: *Displacement field for circular wave propagation at* $f = 150$ kHz*, shown at time* $t = 0.0125$ ms*. The wavefront reaches the sensor position. The propagation remains smooth and only weakly affected by geometric effects, allowing a consistent identification of phase velocity and attenuation from the detected peaks.*

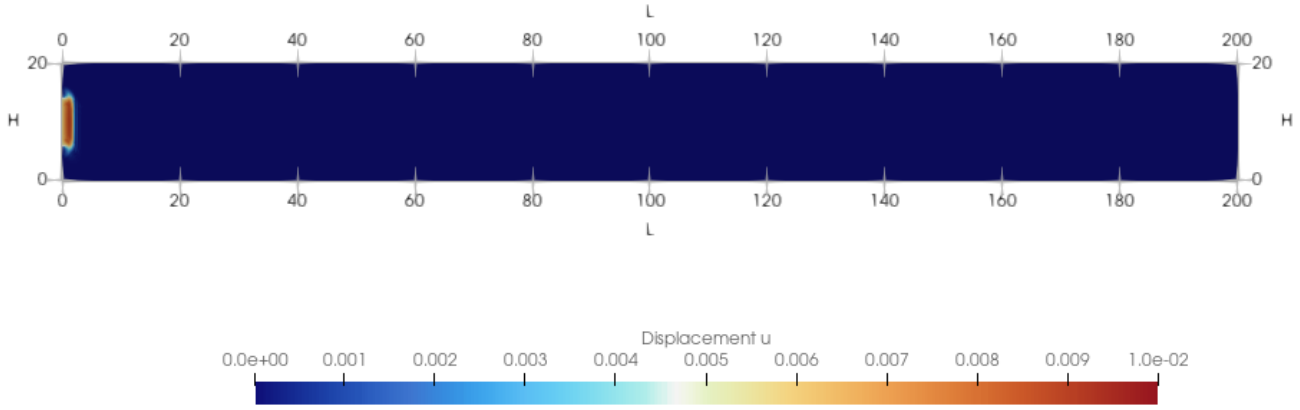

Figure 5.9: *Displacement field for circular wave propagation at* $f = 750$ kHz*, shown at time* $t = 0.0002$ ms*. At this early stage, the primary circular wavefront is clearly identifiable.*

as multiple propagation paths contribute with different effective travel times. Moreover, when the wavelength becomes comparable to the specimen height, the propagation regime may involve guided wave effects, with coupling between longitudinal and transverse deformations. In the present model, transverse displacements along the boundaries are constrained to zero (unixial strain as for 1D simulation), thereby reducing the influence of Poisson coupling and limiting the development of fully coupled waveguide modes.
However, from a physical viewpoint, this transition does not imply that dispersive information is lost in the circular–wave response when $\lambda < H$. In this regime, the only component that remains unambiguously associated with a single propagating mode is the first arriving wavefront. Its arrival time and phase are governed by the intrinsic dispersive properties of the medium, before significant interaction with boundaries and lateral reflections takes place. Consequently, by restricting the analysis to the first onset, at least for the high range frequency where $\lambda < H$, a consistent and physically meaningful dispersive behaviour is recovered for circular waves, with a marked reduction of scatter in the extracted quantities.

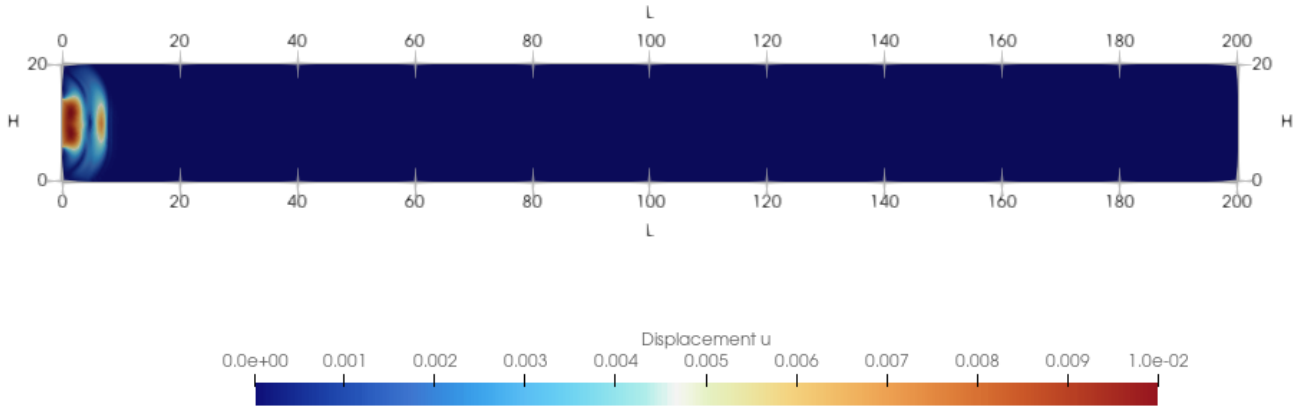

Figure 5.10: *Displacement field for circular wave propagation at* $f = 750$ kHz*, shown at time* $t = 0.0008$ ms*. Reflections from the lateral boundaries become clearly visible and begin to re-enter the propagation domain.*

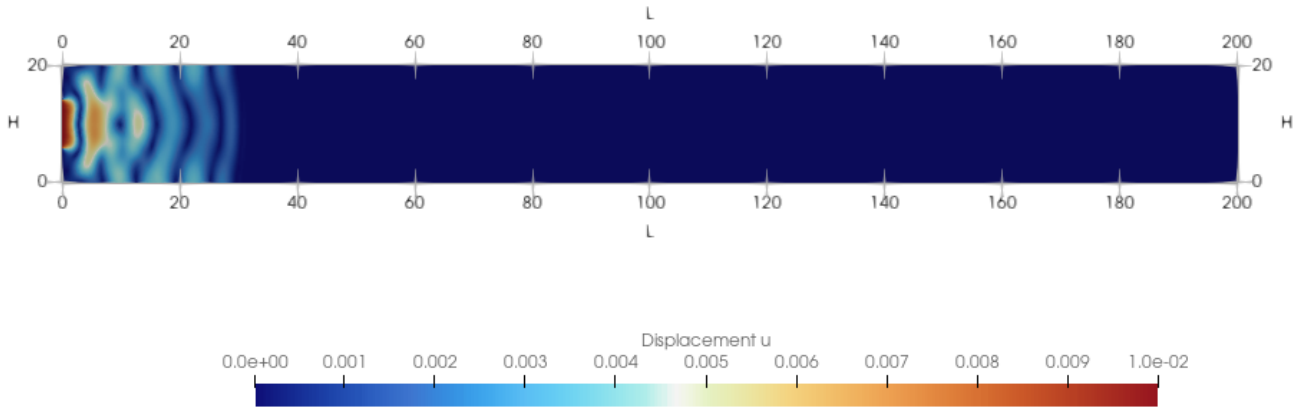

Figure 5.11: *Displacement field for circular wave propagation at* $f = 750$ kHz*, shown at time* $t = 0.003$ kHz*. Boundary reflections act as secondary sources, leading to localized regeneration of the displacement field and complex interference patterns.*

5.2 2D FEM viscous model results

The phase velocity is systematically evaluated from the numerical data using the same definitions adopted throughout this work, namely Eqs. (4.29) and (4.30). Accordingly, phase velocity is extracted from the detected peaks for plane waves and for circular waves in the long-wavelength regime ($\lambda > H$), where the oscillatory response remains regular. Conversely, for circular waves with $\lambda < H$, reliable estimates are obtained by restricting the analysis to the onset wavefront, thereby avoiding contamination from geometric reflections.
As shown in the plane-circular wave comparisons Figures 5.14-5.19, the attenuation of plane waves between the actuator and the sensor remains approximately constant, with an average decay of about 90%, while the additional geometrical attenuation associated with circular propagation is of the order of 5% across the investigated frequency range. For both wave types, the attenuation coefficient is consistently evaluated according to Eq. (4.31).
Figures 5.20 and 5.21 report the frequency dependence of phase velocity and attenuation coefficient obtained from 2D FEM simulations for plane and circular wave propagation. A clear dispersive behavior is observed for both wave types, with phase velocity and attenuation increasing monotonically with frequency and approaching an asymptotic value at high frequencies.

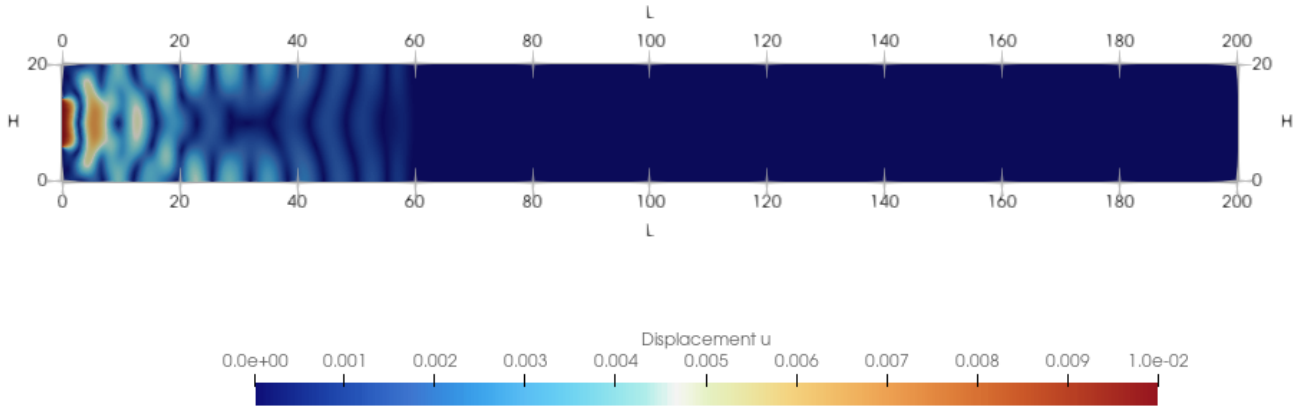

Figure 5.12: *Displacement field for circular wave propagation at* $f = 750$ kHz*, shown at time* $t = 0.006$ ms*. The superposition of direct and reflected wave components fragments the wavefront, producing strong spatial modulation of amplitude and phase.*

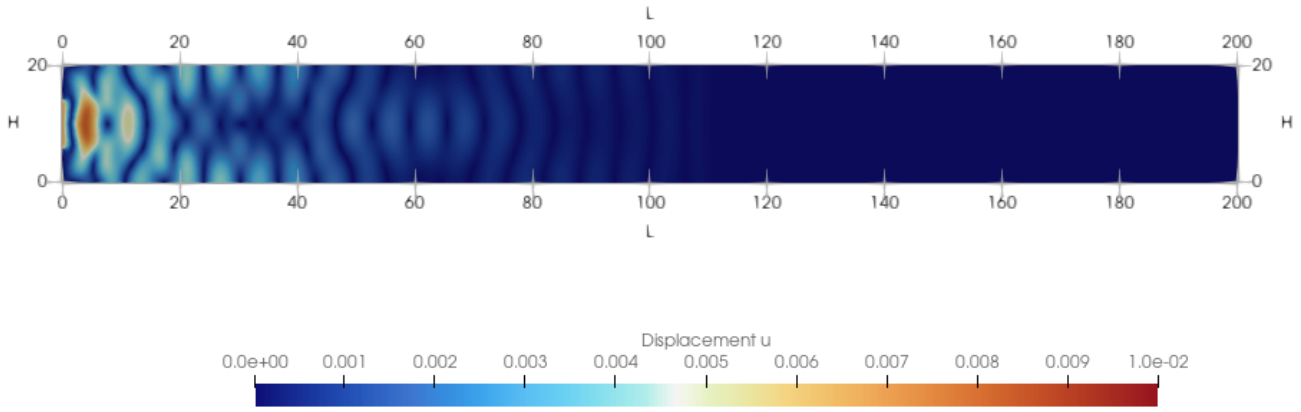

Figure 5.13: *Displacement field for circular wave propagation at* $f = 750$ kHz*, shown at time* $t = 0.0125$ ms*. Although the response remains oscillatory, successive peaks at the sensor no longer correspond to a single propagating wavefront. Interactions between the expanding wavefront and the lateral boundaries generate additional reflected components, which makes the identification of representative peaks less reliable.*

Circular waves systematically exhibit slightly higher apparent phase velocities (within 1%, and therefore negligible within the accuracy limits of the present model), and, most notably, larger attenuation coefficients than plane waves. This behavior is consistently associated with the additional geometrical contribution inherent to circular wave propagation.
To characterize the frequency dependence of the numerical results, the dispersion and attenuation data obtained from 2D FEM simulations are further approximated by means of a nonlinear least–squares procedure. The adopted expressions are introduced solely to provide a compact and smooth representation of the observed trends and to enable a quantitative comparison between plane and circular wave propagation. The phase velocity is fitted using the expression

$$v_p(\omega) = A\cos\left(-\frac{1}{2}B\arctan\left(\frac{c/\rho}{\omega}\right)\right), \tag{5.7}$$

where c is the viscous coefficient, A represents the asymptotic phase velocity, and B controls the transition rate between low– and high–frequency regimes. The attenuation coefficient is

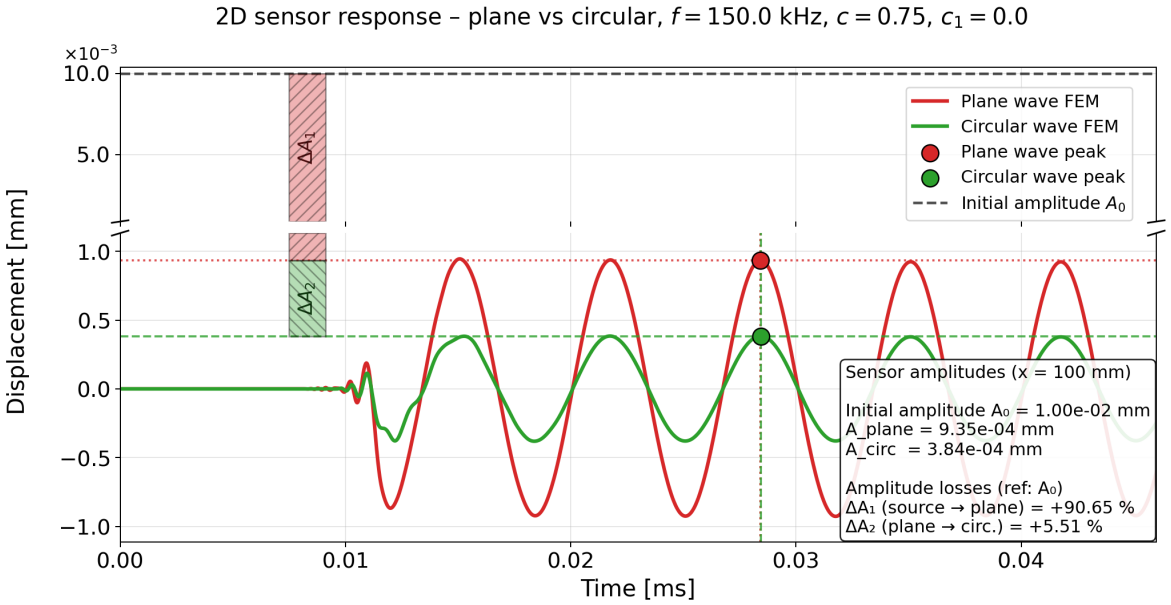

Figure 5.14: *Plane and circular wave responses at* $f = 150$ kHz. *At the sensor location, the peak displacements are* $u(A_{plane}) \approx 9.35 \times 10^{-4}$mm *and* $u(A_{circ}) \approx 3.84 \times 10^{-4}$mm. *The amplitude decay from the source to the plane wave and the additional geometrical attenuation from plane to circular propagation are computed according to Eqs.* (4.7) *and* (4.31) *and equal respectively to 90.6% and 5.5%. The two signals remain well aligned in time, with negligible peak–to–peak delay and phase lag.*

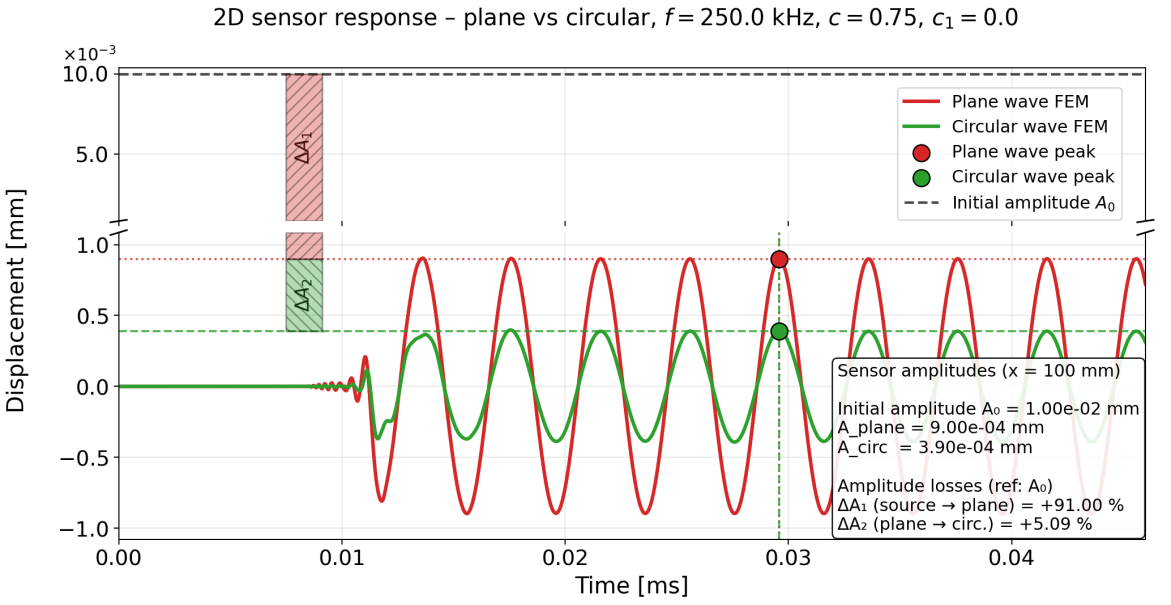

Figure 5.15: *Plane and circular wave responses at* $f = 250$ kHz. *At the sensor location, the peak displacements are* $u(A_{plane}) \approx 9.00 \times 10^{-4}$mm *and* $u(A_{circ}) \approx 3.90 \times 10^{-4}$mm. *The amplitude decay from the source to the plane wave and the additional geometrical attenuation from plane to circular propagation are computed according to Eqs.* (4.7) *and* (4.31) *and equal respectively to 91.0% and 5.1%. The two signals remain well aligned in time, with negligible peak–to–peak delay and phase lag.*

instead fitted using

$$\alpha(\omega) = A \sin\left(-\frac{1}{2} B \arctan\left(\frac{c/\rho}{\omega}\right)\right), \tag{5.8}$$

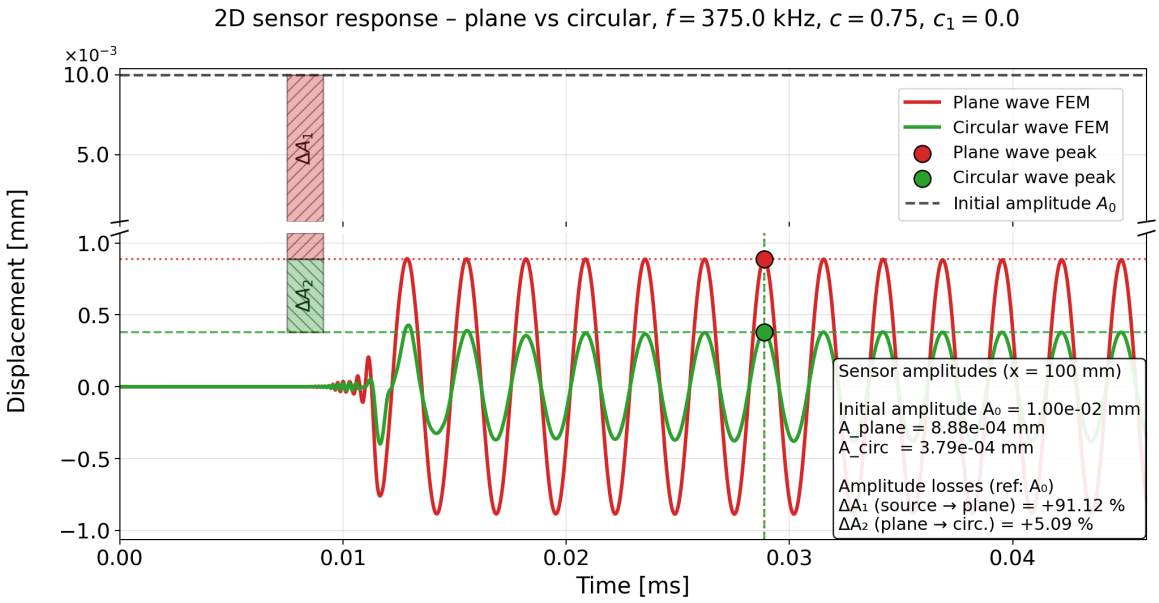

Figure 5.16: *Plane and circular wave responses at* $f = 375$kHz. *At the sensor location, the peak displacements are* $u(A_{plane}) \approx 8.88 \times 10^{-4}$mm *and* $u(A_{circ}) \approx 3.79 \times 10^{-4}$mm. *The amplitude decay from the source to the plane wave and the additional geometrical attenuation from plane to circular propagation are computed according to Eqs.* (4.7) *and* (4.31) *and equal respectively to 91.1% and 5.1%. The two signals remain well aligned in time, with negligible peak–to–peak delay and phase lag.*

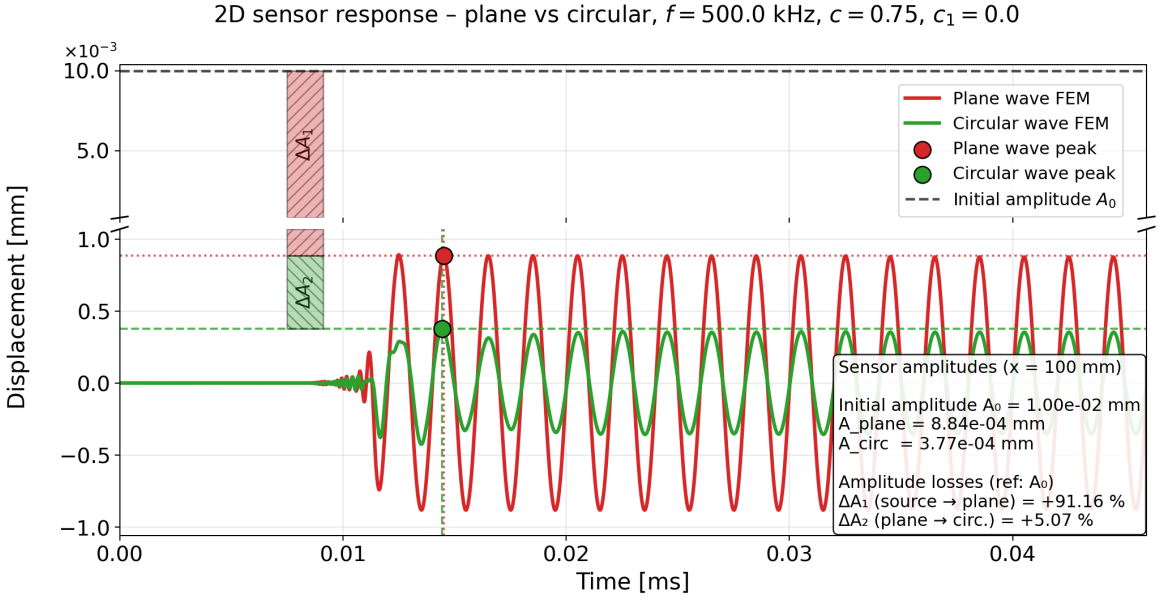

Figure 5.17: *Plane and circular wave responses at* $f = 500$kHz. *At the sensor location, the peak displacements are* $u(A_{plane}) \approx 8.84 \times 10^{-4}$mm *and* $u(A_{circ}) \approx 3.77 \times 10^{-4}$mm. *The amplitude decay from the source to the plane wave and the additional geometrical attenuation from plane to circular propagation are computed according to Eqs.* (4.7) *and* (4.31) *and equal respectively to 91.2% and 5.1%. At this frequency, the two signals remain nearly phase–aligned, although a small but measurable peak–to–peak time shift is observed.*

which follows directly from the imaginary part of the complex wavenumber.
The fitting parameters are obtained by minimizing the normalized residuals between the an-

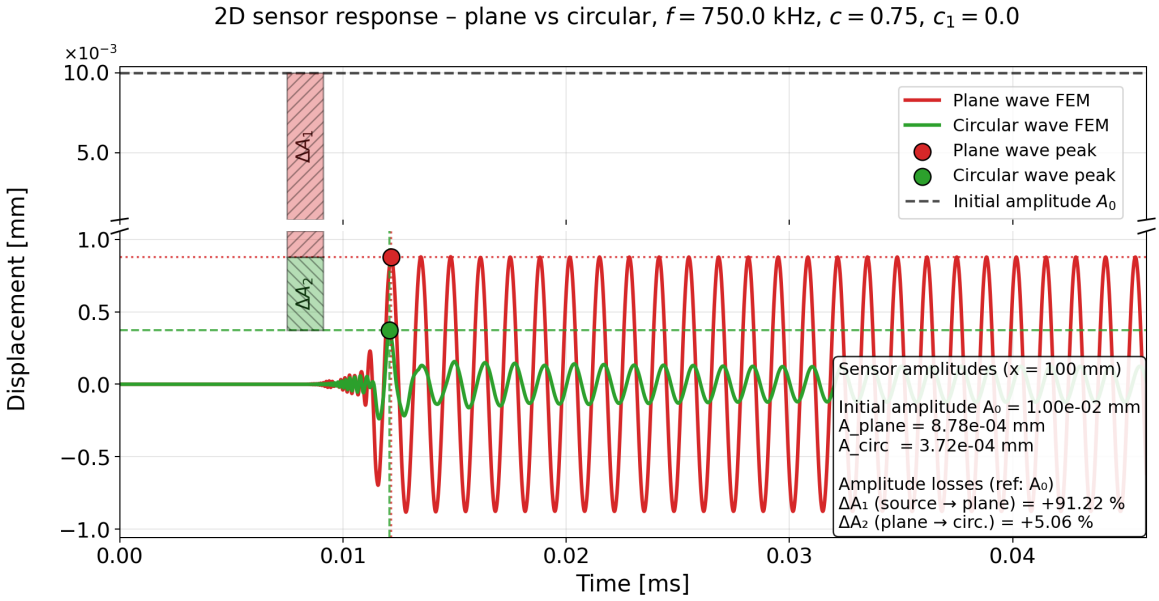

Figure 5.18: *Plane and circular wave responses at* $f = 750$kHz. *At the sensor location, the peak displacements are* $u(A_{plane}) \approx 8.84 \times 10^{-4}$mm *and* $u(A_{circ}) \approx 3.72 \times 10^{-4}$mm. *The amplitude decay from the source to the plane wave and the additional geometrical attenuation from plane to circular propagation are computed according to Eqs.* (4.7) *and* (4.31) *and equal respectively to 91.2% and 5.1%. At this frequency, the two signals are evidently no more phase–aligned, and a peak–to–peak time shift is distinguishable.*

alytical expressions and the FEM data using a bounded least–squares algorithm. Plane and circular waves are fitted independently, allowing the identification of distinct effective parameters associated with the different propagation geometries.
Table 5.2 reports the phase velocity and attenuation values directly extracted from the 2D FEM simulations for plane and circular wave propagation. The tabulated data provide a quantitative reference for the trends discussed in Figures 5.20 and 5.21. For completeness, the fit parameters A, B, and c obtained from the least–squares approximation of the numerical trends are reported in the table captions. These results emphasize that, in order to faithfully reproduce real wave propagation conditions, it is essential to account for the inherently circular (or spherical) nature of waves generated by localized sources, as this directly affects the observed phase velocity and attenuation.

5.3 Proposal framework for phase velocity-attenuation-modulus correlation

In order to facilitate the practical use of the numerical results, a set of tables is constructed to correlate phase velocity and attenuation with the underlying material properties. Specifically, Tables 5.3 and 5.4 provide the dependence of the phase velocity v_p and attenuation coefficient α on the Young 's modulus E and the viscous parameter c, for selected excitation frequencies. The data are generated from 2D FEM simulations and organized in a form suitable for direct consultation and interpolation. The tabulated results reproduce the expected physical trends associated with wave propagation in viscoelastic media. For a fixed excitation frequency, both the phase velocity v_p and the attenuation coefficient α increase monotonically with the Young's modulus E, reflecting the stiffening of the material and the corresponding increase in wave speed and energy dissipation. At fixed E and excitation frequency, increasing the viscous parameter c leads to a systematic increase in attenuation, while only marginally affecting the phase velocity. It is worth noting that the underlying model does predict distinct phase velocities for different

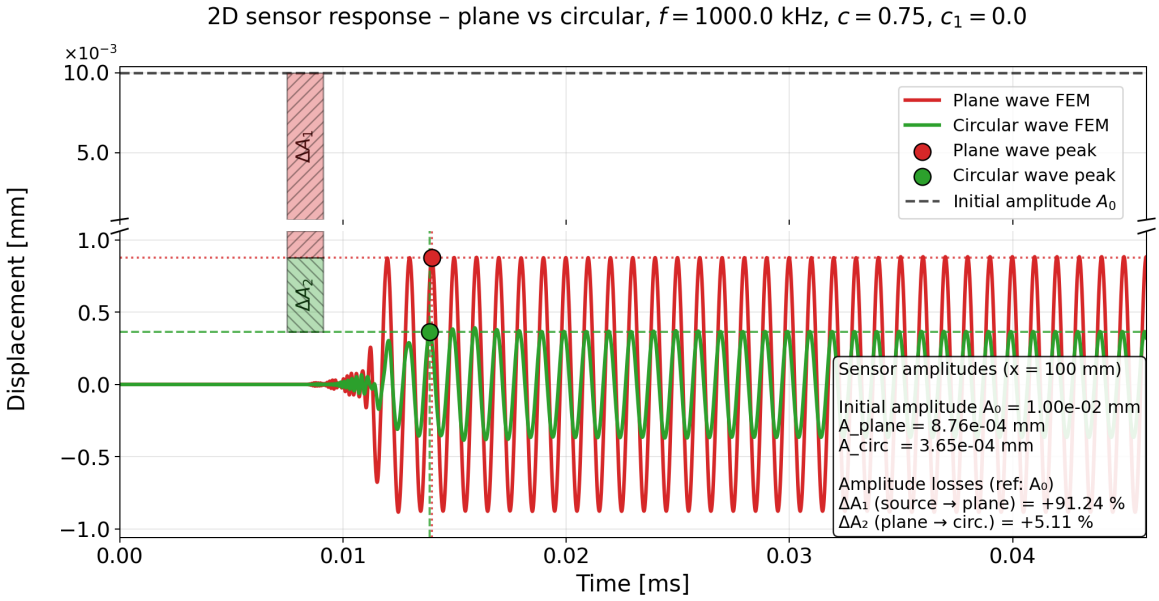

Figure 5.19: *Plane and circular wave responses at* $f = 1,000$kHz. *At the sensor location, the peak displacements are* $u(A_{plane}) \approx 8.76 \times 10^{-4}$mm *and* $u(A_{circ}) \approx 3.65 \times 10^{-4}$mm. *The amplitude decay from the source to the plane wave and the additional geometrical attenuation from plane to circular propagation are computed according to Eqs.* (4.7) *and* (4.31) *and amount respectively to* 91.2% *and* 5.1%. *At this frequency, the two signals are no longer perfectly phase–aligned, and a peak–to–peak time shift can be identified, similarly to the* 500kHz *simulation. The partial reduction of the time shift observed with respect to the* 750kHz *case is attributed to the combined effect of increased material dissipation and the superposition of reflected wave components at the sensor location.*

Frequency [kHz]	v_p^{plane} [mm/ms]	v_p^{circular} [mm/ms]	α^{plane} [1/mm]	α^{circular} [1/mm]
150	8,502.60	8,498.58	0.02370	0.03260
250	8,627.30	8,632.60	0.02408	0.03263
375	8,667.82	8,671.95	0.02422	0.03273
500	8,682.21	8,730.60	0.02426	0.03277
750	8,697.04	8,758.36	0.02433	0.03293
1000	8,706.67	8,776.12	0.02434	0.03309

Table 5.2: *Phase velocity and attenuation values extracted from 2D FEM simulations for plane and circular wave propagation. The frequency–dependent trends reported in the table are described using a phenomenological least–squares approximation, yielding approximate parameters* $A_{plane} \approx 8{,}708$ *mm/ms,* $B_{plane} \approx 0.85$, $c_{plane} \approx 0.94$, *and* $A_{circular} \approx 8{,}789$ *mm/ms,* $B_{circular} \approx 0.48$, $c_{circular} \approx 2.99$.

values of c. However, within the frequency range investigated in this study, the phase velocity is already in its asymptotic regime. As a consequence, the variations of v_p associated with changes in c remain below the numerical error threshold adopted in the present analysis and can therefore be neglected.

Finally, comparison between Tables 5.3 and 5.4 highlights that increasing the excitation frequency results in higher phase velocities and significantly larger attenuation levels, in agreement with the frequency-dependent nature of viscous dissipation. These trends confirm the internal

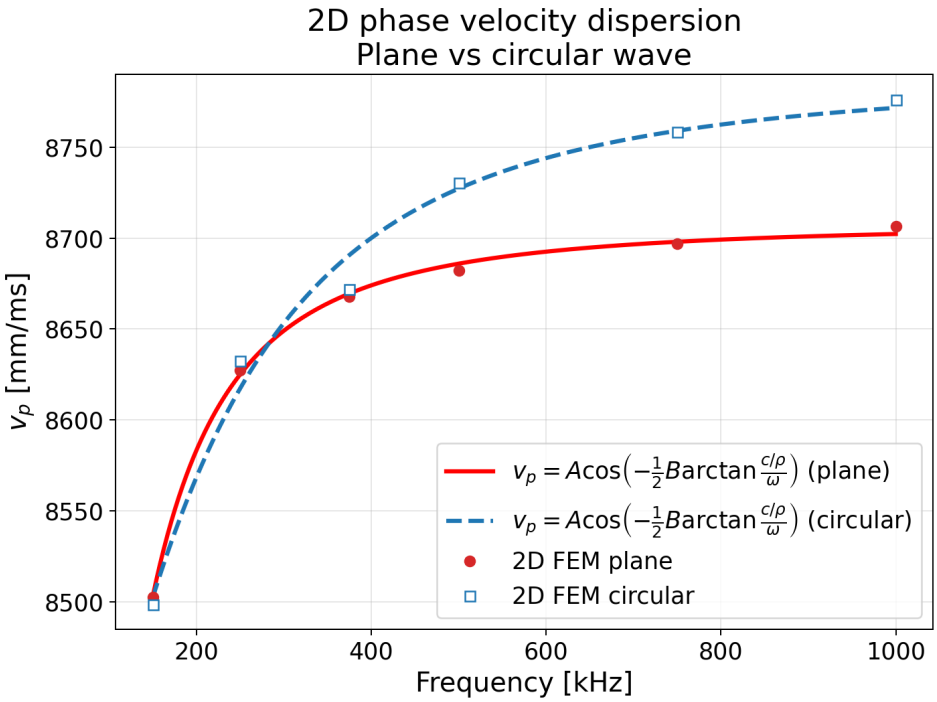

Figure 5.20: *Phase velocity as a function of frequency obtained from 2D FEM simulations for plane and circular wave propagation. The corresponding FEM data points and the parameters of the phenomenological least–squares approximation are reported in Table 5.2.*

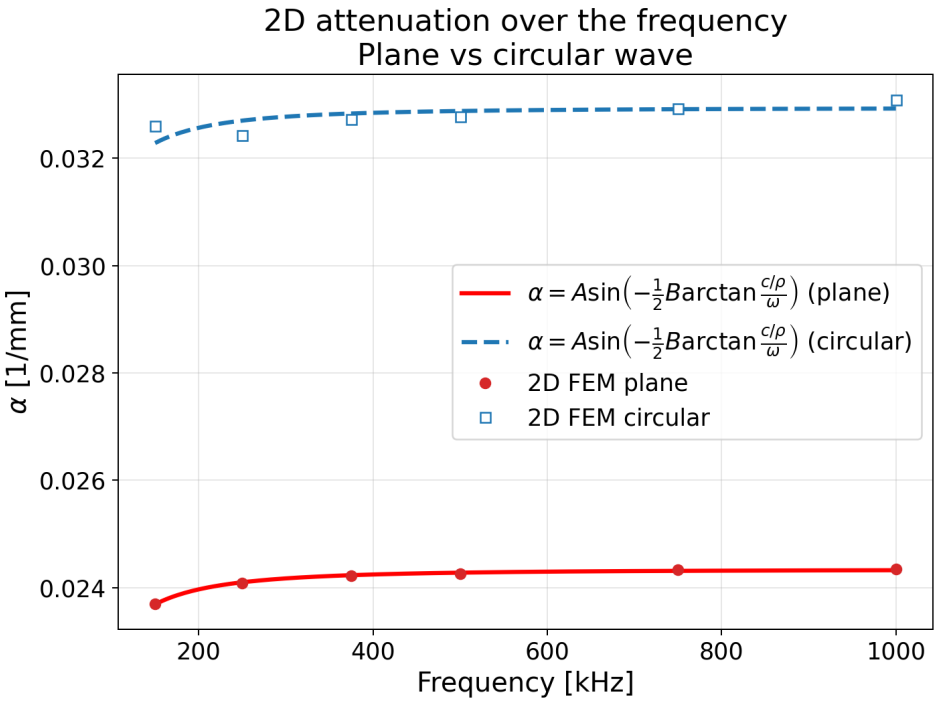

Figure 5.21: *Attenuation coefficient as a function of frequency obtained from 2D FEM simulations for plane and circular waves. The FEM attenuation values and the parameters of the phenomenological least–squares description are reported in Table 5.2.*

consistency of the FEM-based reference tables and support their use as a reliable framework

for material parameter identification.

E [GPa]	v_p [mm/ms]	$f = 250$ kHz			
		$\alpha\,[\mathrm{mm}^{-1}]$			
		$c\,[\mathrm{g}/(\mathrm{mm}\cdot\mathrm{ms})]$			
		0.2	0.4	0.6	0.8
50	6.1×10^3	1.7×10^{-2}	2.5×10^{-2}	3.5×10^{-2}	4.5×10^{-2}
75	7.5×10^3	1.6×10^{-2}	2.3×10^{-2}	3.0×10^{-2}	3.8×10^{-2}
100	8.7×10^3	1.4×10^{-2}	2.1×10^{-2}	2.8×10^{-2}	3.4×10^{-2}
125	9.7×10^3	1.1×10^{-2}	1.8×10^{-2}	2.5×10^{-2}	3.1×10^{-2}
150	1.0×10^4	1.0×10^{-2}	1.7×10^{-2}	2.4×10^{-2}	2.9×10^{-2}

Table 5.3: *FEM-based reference table for circular-wave propagation at $f = 250$ kHz. The phase velocity v_p is reported as a single representative value for each elastic modulus E, since at this frequency and for the considered viscous coefficients the system operates in the asymptotic regime of the dispersion curve $v_p(\omega)$. Consequently, the phase velocity becomes practically independent of the viscous parameter c, and possible differences would only reflect numerical errors. For this reason, v_p is not differentiated with respect to c, whereas the attenuation coefficient $\alpha(E, c)$ is explicitly reported for several values of the viscous parameter c in order to highlight the effect of viscous dissipation. All results are obtained assuming constant material properties, with density $\rho = 1.78 \times 10^{-3}$ g/mm^3, Poisson's ratio $\nu = 0.30$, and an input-face height $H = 20$ mm.*

E [GPa]	v_p [mm/ms]	$f = 500$ kHz			
		$\alpha\,[\mathrm{mm}^{-1}]$			
		$c\,[\mathrm{g}/(\mathrm{mm}\cdot\mathrm{ms})]$			
		0.2	0.4	0.6	0.8
50	6.3×10^3	1.8×10^{-2}	2.6×10^{-2}	3.6×10^{-2}	4.6×10^{-2}
75	7.7×10^3	1.7×10^{-2}	2.4×10^{-2}	3.1×10^{-2}	3.9×10^{-2}
100	8.9×10^3	1.6×10^{-2}	2.2×10^{-2}	2.9×10^{-2}	3.5×10^{-2}
125	9.9×10^3	1.2×10^{-2}	1.9×10^{-2}	2.6×10^{-2}	3.2×10^{-2}
150	1.1×10^4	1.1×10^{-2}	1.8×10^{-2}	2.5×10^{-2}	3.1×10^{-2}

Table 5.4: *FEM-based reference table for circular-wave propagation at $f = 500$ kHz. The phase velocity v_p is reported as a single representative value for each elastic modulus E, since at this frequency and for the considered viscous coefficients the system operates in the asymptotic regime of the dispersion curve $v_p(\omega)$. Consequently, the phase velocity becomes practically independent of the viscous parameter c, and possible differences would only reflect numerical errors. For this reason, v_p is not differentiated with respect to c, whereas the attenuation coefficient $\alpha(E, c)$ is explicitly reported for several values of the viscous parameter c in order to highlight the effect of viscous dissipation. All results are obtained assuming constant material properties, with density $\rho = 1.78 \times 10^{-3}$ g/mm^3, Poisson's ratio $\nu = 0.30$, and an input-face height $H = 20$ mm.*

The identification of the material parameters is based on a two-step procedure combining direct table lookup and numerical fitting.
Given an experimental measurement of phase velocity v_p^{meas} and attenuation α^{meas} at a fixed frequency, the FEM-based reference tables are first queried. If a pair (E, c) exists such that

both $v_p(E)$ and $\alpha(E,c)$ match the measured values within the experimental tolerance, the corresponding parameters are directly assigned. For parameter values not explicitly tabulated, the FEM responses $v_p(E)$ and $\alpha(E,c)$ are evaluated by bilinear interpolation over the discrete (E,c) grid defined by the reference tables.
Then, the material parameters are identified by interpolating the FEM-based data and minimizing the combined mismatch between measured and numerical quantities. Specifically, the parameters (E,c) are obtained as

$$\min_{E,c} \left[\left(v_p(E) - v_p^{\text{meas}}\right)^2 + \left(\alpha(E,c) - \alpha^{\text{meas}}\right)^2 \right], \tag{5.9}$$

where $v_p(E)$ and $\alpha(E,c)$ are evaluated on the interpolated FEM response surfaces.

5.4 Extension of the FEM-based identification framework to other materials

The identification framework developed in the previous sections was formulated and validated for a viscoelastic medium representative of steel, with the aim of establishing a clear and controlled relationship between phase velocity, attenuation, and material parameters. In this section, the same methodology is extended to a concrete sample in order to assess the robustness and repeatability of the proposed identification procedure.
The extension is carried out by following the same logical and numerical workflow adopted for the homogeneous case, starting from the one-dimensional configuration and calibration and progressively advancing to the two-dimensional FEM formulation and outputs. First, the mass density is set to $\rho = 2.3 \times 10^{-3}$ g/mm^3, while the Young's modulus is fixed to $E = 30 \times 10^3$ MPa. For the two-dimensional simulations, a Poisson's ratio $\nu = 0.20$ is adopted, whereas this parameter is irrelevant in the one-dimensional configuration.
The geometric setup is kept identical to that employed in the previous sections in order to ensure a consistent comparison. The computational domain has a total length $L = 200$ mm, while the transverse height is set to $H = 20$ mm and is therefore only relevant for the two-dimensional formulation. For the concrete case, the analysis is restricted to a selected set of excitation frequencies, namely $f = 120$, 150, 200, 250, and 375 kHz. The numerical and analytical responses are evaluated at a single sensor located at mid-span of the specimen, i.e. at $x = 100$ mm, consistently with the analysis strategy adopted for the metallic sample (see Table 5.5).

f [kHz]	v_p [mm/ms]	λ [mm]	$A(x)/A_0$ $x = 100$ mm
120	3,479.795	28.998	0.3029%
150	3,523.464	23.490	0.2816%
200	3,560.179	17.801	0.2649%
250	3,578.098	14.312	0.2571%
375	3,596.428	9.590	0.2494%

Table 5.5: *Analytical phase velocity v_p, wavelength λ and normalized amplitude $A(x)/A_0$ evaluated at the sensor location $x = 100$ mm for the viscoelastic concrete model. Results are reported for selected excitation frequencies in the range* 120–375 kHz. *Material properties are $\rho = 2.3\times10^{-3}$ g/mm^3, $E = 30\times10^3$ MPa, $c = 1$ g/(mm·ms), and specimen length $L = 200$ mm.*

To assess the numerical requirements of the 1D concrete model, we repeat the same quantitative convergence analysis based on RMSE error surfaces previously introduced for the steel-like case. In particular, the 1D solver is executed for a large set of space-time discretizations, spanning

multiple values of the number of finite elements N_{el} and temporal subdivisions N_{ti}. For each pair (N_{el}, N_{ti}) and for each excitation frequency, phase velocity and normalized amplitude at the sensor are extracted and compared against the analytical reference values reported in Table 5.5. The relative errors are then combined into a single indicator through the frequency-dependent RMSE definition already introduced in Eq. (4.38). This produces, for each frequency, a discrete set of error samples $(N_{el}^k, N_{ti}^k, \mathrm{RMSE}^k)$.

These discrete RMSE values are interpolated over the (N_{el}, N_{ti}) plane to obtain continuous error surfaces in the three-dimensional space $(N_{el}, N_{ti}, \mathrm{RMSE})$, as shown in the top panel of Fig. 5.22. Within this framework, the admissible discretizations are identified by introducing the target accuracy level RMSE = 1% and computing the corresponding intersection curves between each error surface and the horizontal threshold plane. The resulting iso-error contours are projected onto the (N_{el}, N_{ti}) plane (bottom panel of Fig. 5.22), thus defining, for each frequency, the boundary separating acceptable and unacceptable discretization pairs.

In order to obtain a compact analytical representation of these convergence boundaries, the extracted RMSE = 1% contours are approximated by frequency-dependent hyperbolic fits of the form (4.41). For the concrete case, the fitted convergence boundaries are:

$$
\begin{aligned}
120\ \text{kHz:} \quad & N_{ti} = 2100.0 + \frac{6.500 \times 10^4}{N_{el} - 370.0}, \\
150\ \text{kHz:} \quad & N_{ti} = 3000.0 + \frac{1.139 \times 10^5}{N_{el} - 390.0}, \\
200\ \text{kHz:} \quad & N_{ti} = 4300.0 + \frac{9.662 \times 10^4}{N_{el} - 420.0}, \\
250\ \text{kHz:} \quad & N_{ti} = 5200.0 + \frac{2.107 \times 10^5}{N_{el} - 480.0}, \\
375\ \text{kHz:} \quad & N_{ti} = 5800.0 + \frac{4.156 \times 10^5}{N_{el} - 650.0}.
\end{aligned}
$$

Table 5.6 reports the minimum admissible combinations of spatial and temporal discretization parameters (N_{el}, N_{ti}) for each excitation frequency, such that the numerical convergence error remains below the prescribed threshold of 1%, corresponding to the fitted convergence equations above.

Table 5.7 instead summarizes the specific (N_{el}, N_{ti}) pairs selected for the subsequent two-dimensional FEM simulations. These discretization choices are deliberately taken slightly inside the admissible region defined by the convergence boundaries, ensuring a conservative margin with respect to the 1% error threshold while avoiding unnecessary over-refinement.

It is worth emphasizing, by comparison with the analogous relations obtained for the metallic material in the subsection 4.7.2, that the convergence laws derived in this section are inherently dependent on the material properties. As a consequence, the space–time convergence analysis and the associated error-threshold identification procedure must be repeated for each material under investigation, rather than being regarded as universal.

Once the admissible space-time discretizations have been identified, the two-dimensional FEM simulations are performed for different combinations of the Young's modulus E and the viscous parameter c. The numerical results are then post-processed to extract phase velocity and attenuation according to a frequency-dependent strategy, consistently with the underlying wave propagation regime.

When the wavelength λ is much larger than the specimen height H, the propagating field can be regarded as quasi-one-dimensional. In this case, phase velocity and attenuation are evaluated using a peak-based approach, based on the comparison between the peak amplitudes measured at the actuator and at the sensor location after the initial transient.

Conversely, when the wavelength becomes comparable to the specimen height, i.e. when $\lambda =$

N_{el}	N_{ti}				
	120 kHz	150 kHz	200 kHz	250 kHz	375 kHz
400	4,267				
500	2,600	4,036	5,508		
600	2,383	3,543	4,837	6,956	
700	2,297	3,368	4,646	6,158	14,112
800	2,252	3,278	4,555	5,859	8,571

Table 5.6: *Minimum temporal discretization N_{ti} required to satisfy the* RMSE $= 1\%$ *accuracy threshold for the concrete material, as a function of the spatial discretization N_{el} and excitation frequency. The reported values are obtained from the frequency-dependent hyperbolic convergence laws fitted to the interpolated RMSE error surfaces and represent the lower admissible boundary of the space–time discretization domain.*

f [kHz]	N_{el}	N_{ti}
120	450	3,000
150	500	4,200
200	550	5,200
250	630	6,800
375	760	9,700

Table 5.7: *Spatial and temporal discretization pairs selected for the one-dimensional FEM simulations of the concrete specimen. All points are chosen inside the admissible region defined by the* RMSE $= 1\%$ *convergence boundaries obtained from the interpolated error surfaces, ensuring that both phase velocity and attenuation errors remain below the prescribed accuracy threshold for each excitation frequency.*

		$f = 150$ kHz		
		α [mm^{-1}]		
E [GPa]	v_p [mm/ms]	c [g/(mm · ms)]		
		0.1	0.5	1.0
15.0	2.7×10^3	3.2×10^{-2}	4.9×10^{-2}	8.7×10^{-2}
20.0	3.1×10^3	2.4×10^{-2}	4.3×10^{-2}	7.7×10^{-2}
25.0	3.5×10^3	2.2×10^{-2}	4.0×10^{-2}	6.9×10^{-2}
30.0	3.8×10^3	1.6×10^{-2}	3.7×10^{-2}	6.4×10^{-2}
35.0	4.1×10^3	1.5×10^{-2}	3.5×10^{-2}	6.0×10^{-2}

Table 5.8: *FEM-based reference table for circular-wave propagation in concrete at $f =$* 150 kHz*. The phase velocity v_p is reported as a single representative value for each elastic modulus E, since at this frequency and for the considered viscous coefficients the system operates in the asymptotic regime of the dispersion curve $v_p(\omega)$. Consequently, the phase velocity becomes practically independent of the viscous parameter c, and possible differences would only reflect numerical errors. For this reason, v_p is not differentiated with respect to c, whereas the attenuation coefficient $\alpha(E, c)$ is explicitly reported for several values of the viscous parameter c in order to highlight the effect of viscous dissipation. All results are obtained assuming constant material properties, with density $\rho = 2.3 \times 10^{-3}$ g/mm^3, Poisson's ratio $\nu = 0.20$, and an input-face height $H = 20$ mm.*

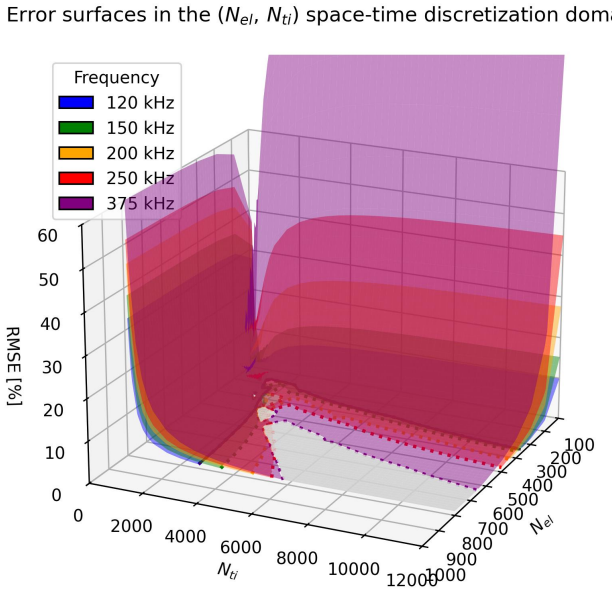

((a))

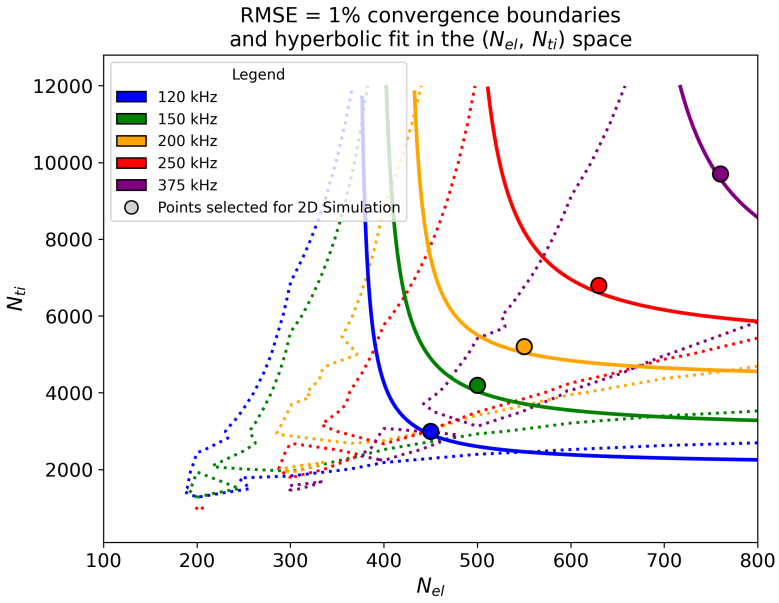

((b))

Figure 5.22: *Error analysis in the (N_{el}, N_{ti}) space–time discretization domain for the viscoelastic concrete model. (**a**) Three-dimensional RMSE surfaces obtained from one-dimensional simulations as a function of the number of spatial elements N_{el} and temporal subdivisions N_{ti}, for excitation frequencies f = 120, 150, 200, 250, and 375 kHz. Each colored surface corresponds to a fixed frequency and highlights the coupled influence of spatial and temporal resolution on numerical accuracy. A pronounced error decay is observed as both discretizations are refined, with increasingly restrictive requirements at higher frequencies. (**b**) Two-dimensional projection of the RMSE= 1% convergence boundaries in the (N_{el}, N_{ti}) plane. Dashed curves denote the iso-error contours extracted from the numerical data, while solid curves represent the corresponding hyperbolic fits used to parameterize the convergence limits. Filled markers indicate the discretization pairs selected for subsequent two-dimensional simulations.*

E [GPa]	v_p [mm/ms]	$f = 250$ kHz		
		$\alpha\,[\mathrm{mm}^{-1}]$		
		$c\,[\mathrm{g}/(\mathrm{mm}\cdot\mathrm{ms})]$		
		0.1	0.5	1.0
15.0	2.8×10^3	3.4×10^{-2}	5.0×10^{-2}	8.8×10^{-2}
20.0	3.2×10^3	2.8×10^{-2}	4.4×10^{-2}	7.8×10^{-2}
25.0	3.6×10^3	2.5×10^{-2}	4.1×10^{-2}	7.2×10^{-2}
30.0	3.9×10^3	1.7×10^{-2}	3.9×10^{-2}	6.8×10^{-2}
35.0	4.2×10^3	1.6×10^{-2}	3.8×10^{-2}	6.3×10^{-2}

Table 5.9: *FEM-based reference table for circular-wave propagation in concrete at $f =$ 250 kHz. The phase velocity v_p is reported as a single representative value for each elastic modulus E, since at this frequency and for the considered viscous coefficients the system operates in the asymptotic regime of the dispersion curve $v_p(\omega)$. Consequently, the phase velocity becomes practically independent of the viscous parameter c, and possible differences would only reflect numerical errors. For this reason, v_p is not differentiated with respect to c, whereas the attenuation coefficient $\alpha(E, c)$ is explicitly reported for several values of the viscous parameter c in order to highlight the effect of viscous dissipation. All results are obtained assuming constant material properties, with density $\rho = 2.3 \times 10^{-3}$ g/mm^3, Poisson's ratio $\nu = 0.20$, and an input-face height $H = 20$ mm.*

$\mathcal{O}(H)$, geometrical effects and multimodal contributions become non-negligible, and the peak-based identification procedure becomes less reliable. In this regime, the material properties are extracted from the analysis of the first identifiable wavefront directly from the time-domain signal, in order to isolate the primary propagation mechanism and avoid contamination from reflections and higher-order modes.

For the concrete specimen considered in this study, the transition between the two regimes occurs at approximately $f = 200$ kHz. Frequencies below this threshold are therefore analyzed using the peak-based approach, whereas higher frequencies are processed using first-arrival wavefront analysis. The phase velocity and attenuation values extracted from the two-dimensional simulations are subsequently organized into FEM-based reference Tables 5.8 and 5.9, following the same structure adopted in the previous subsections. These tables provide a direct correspondence between the material parameters (E, c) and the observable quantities (v_p, α), and constitute the basis for the identification procedure discussed earlier.

6 Conclusions and future projects

This work has presented a unified analytical-numerical framework aimed at redefining the role of ultrasonic testing from a qualitative or supportive technique to a fully quantitative method for the direct identification of material properties, with particular emphasis on the Young's modulus.

A first key outcome of the study concerns the intrinsic limitations of classical one-dimensional analytical models for ultrasonic wave propagation. Although such models are well established and rigorously validated in the literature, including recent developments for construction materials and viscoelastic media[71;72], they inherently describe plane-wave propagation. As a consequence, they are unable to capture the geometrical spreading effects associated with circular or localized wavefronts generated by realistic ultrasonic sources. Classical wave propagation theory has long established that cylindrical and spherical waves exhibit an intrinsic amplitude decay due to geometrical spreading, even in the absence of material dissipation[3]. The present results confirm that these effects are not negligible in practical testing configurations and must be explicitly accounted for.

A second major limitation addressed by this work relates to current normative guidelines to ultrasonic testing. Existing standards generally do not permit the direct identification of material parameters from ultrasonic measurements. Instead, they rely on empirical correlations derived from destructive tests-such as core drilling in existing structures-which are subsequently used to calibrate velocity-modulus relationships for specific materials and contexts. Ultrasonic measurements are therefore employed primarily to densify or extend experimentally calibrated datasets, rather than as an independent and primary characterization tool. This empirical paradigm is well documented in classical ultrasonic testing practice for concrete and construction materials[108].

In contrast, the methodology proposed in this paper provides an alternative and fully physics-based route for material identification. By coupling validated one-dimensional analytical solutions[71;72] with carefully calibrated finite element models, and by extending the formulation to two-dimensional domains capable of reproducing circular wave propagation, it becomes possible to directly link measurable ultrasonic quantities-namely phase velocity and attenuation-to intrinsic material parameters. The two-dimensional FEM framework plays a crucial role in this process, as it naturally captures the additional attenuation and subtle phase-velocity variations induced by geometrical spreading and boundary interactions, which would otherwise bias the identification if plane-wave models were employed.

The results clearly show that attenuation associated with circular wave propagation is systematically higher than that predicted by plane-wave assumptions, while phase velocity exhibits smaller but still measurable deviations. This behavior is further amplified in heterogeneous materials, where scattering mechanisms contribute to an effective energy diffusion process that cannot be captured by simplified one-dimensional formulations[109]. These findings highlight the necessity of adopting two-dimensional (or higher-dimensional) models when ultrasonic measurements are performed using localized sources, as is the case in most practical inspections. Neglecting these effects would lead to an underestimation of attenuation and, consequently, to biased estimates of material properties.

From a broader perspective, the framework developed in this study lays the foundation for a new generation of FEM-based reference charts. These charts provide, as a function of inspection frequency and observable ultrasonic quantities, direct predictions of the Young's modulus-arguably the most relevant mechanical parameter for structural assessment-together with additional constitutive parameters. The reliability of this approach relies on a careful control of numerical dispersion and stability, which are known to be critical aspects in finite element simulations of wave propagation problems[110]. By systematically addressing these numerical issues through convergence analyses and calibrated discretization strategies, the proposed framework enables

ultrasonic testing to be exploited to its full potential.
Future developments will focus on extending the present framework beyond first-gradient viscoelasticity[80;81;111;112]. In this research, we have established a coherent analytical-numerical methodology that integrates theoretical modeling, convergence-controlled finite element simulations, and parameter identification strategies. The next step will consist in systematically reproducing and broadening this approach to encompass a wider range of constitutive behaviors and propagation regimes, maintaining the same level of numerical rigor and physical consistency.
Analytical models incorporating strain-gradient effects, microstructural length scales[113], and micro-inertia are already available in the literature and will be generalized to higher-dimensional configurations[45;114–116]. In particular, the formulations developed in this thesis are already structurally adaptable to three-dimensional settings, enabling the transition from circular wave propagation (2D) to fully spherical waves (3D). This extension is essential to reproduce realistic experimental conditions, where localized ultrasonic sources generate three-dimensional wavefields.
In a 3D framework, additional geometric dispersion effects and signal "contamination" phenomena are expected to emerge, due to reflections, refractions, and multiple propagation paths within the solid domain, similarly to what has been observed in the two-dimensional analyses. However, the full three-dimensional implementation is necessary to faithfully reproduce real inspection scenarios and to quantify these effects in a physically consistent manner.
At present, the principal limitation of the proposed framework lies in its computational cost. High-resolution simulations with strict space-time convergence control require significant numerical resources. Future work will therefore address this challenge either through the use of more advanced hardware and high-performance computing architectures, or through the optimization of the computational workflow and numerical implementation, without compromising the accuracy and stability achieved in the present study.
Ultimately, the long-term objective remains the construction of comprehensive, frequency-dependent identification maps capable of predicting the Young's modulus and other intrinsic parameters for a broad class of materials, thereby providing a robust scientific foundation for the evolution and standardization of ultrasonic testing as a primary, physics-based characterization method. It is hoped that the methodology developed herein will support the transition of ultrasonic testing from an empirical diagnostic tool to a predictive, physics-based standard for the reliable determination of intrinsic material properties.

References

[1] P. O. Akadiri and P. O. Olomolaiye. Development of sustainable assessment criteria for building materials selection. *Engineering, Construction and Architectural Management*, 2012.

[2] B. Ramesh, L. Cao, and R. Baskerville. Agile requirements engineering practices and challenges: An empirical study. *Information Systems Journal*, 20(5):449–480, 2010.

[3] J. D. Achenbach. *Wave Propagation in Elastic Solids*. North-Holland, Amsterdam, 1973.

[4] H. A. Lauwerier and W. T. Koiter. *Applied Mathematics and Mechanics*. North-Holland, 1973.

[5] D. M. Boore. Finite difference methods for seismic wave propagation in heterogeneous materials. *Methods in Computational Physics*, 11:1–37, 1972.

[6] A. Tomassi, F. Trippetta, R. de Franco, and R. Ruggieri. From petrophysical properties to forward-seismic modeling of facies heterogeneity in the carbonate realm (majella massif, central italy). *Journal of Petroleum Science and Engineering*, 211:110242, 2022.

[7] A. Tomassi, F. Trippetta, R. de Franco, and R. Ruggieri. How petrophysical properties influence the seismic signature of carbonate fault damage zone: Insights from forward-seismic modelling. *Journal of Structural Geology*, page 104802, 2023.

[8] A. Tomassi, S. Milli, and D. Tentori. Synthetic seismic forward modeling of a high-frequency depositional sequence: The example of the tiber depositional sequence (central italy). *Marine and Petroleum Geology*, 160:106624, 2024.

[9] M. di Marzo, A. Tomassi, and L. Placidi. A methodology for structural damage detection adding masses. *Research in Nondestructive Evaluation*, 35(3):172–196, 2024.

[10] F. Dell'Isola, I. Giorgio, and U. Andreaus. Elastic pantographic 2d lattices: a numerical analysis on static response and wave propagation. *Proceedings of the Estonian Academy of Sciences*, 64(3):219–225, 2015.

[11] Sara Quiligotti, Gerard A. Maugin, and Francesco dell'Isola. Wave motions in unbounded poroelastic solids infused with compressible fluids. *Zeitschrift für Angewandte Mathematik und Physik (ZAMP)*, 53(6):1113–1130, 2002.

[12] G. Rosi and N. Auffray. Anisotropic and dispersive wave propagation within strain-gradient framework. *Wave Motion*, 63:120–134, 2016.

[13] B. Mace and E. Marconi. Wave motion and dispersion phenomena: Veering, locking and strong coupling effects. *Journal of the Acoustical Society of America*, 131(2):1015–1028, 2012.

[14] A. Wolfenden. *Dynamic Elastic Modulus Measurements in Materials*. ASTM International, 1990.

[15] T. Naciri, P. Navi, and A. Ehrlacher. Harmonic wave propagation in viscoelastic heterogeneous materials part i: Dispersion and damping relations. *Mechanics of Materials*, 18(4):313–333, 1994.

[16] F. Hernando Quintanilla, Z. Fan, M. J. S. Lowe, and R. V. Craster. Guided waves' dispersion curves in anisotropic viscoelastic single- and multi-layered media. *Proceedings of the Royal Society A: Mathematical, Physical and Engineering Sciences*, 471(2183):20150268, 2015.

[17] C. Bagni, I. M. Gitman, and H. Askes. A micro-inertia gradient visco-elastic motivation for proportional damping. *Journal of Sound and Vibration*, 347:115–125, 2015.

[18] Y. M. Tsai and H. Kolsky. Surface wave propagation for linear viscoelastic solids. *Journal of the Mechanics and Physics of Solids*, 16(2):99–110, 1968.

[19] Kuanjie Ding, Zhongya Lin, Yehui Bie, and Yueguang Wei. The strain gradient viscoelasticity full field solutions for mode-i and mode-ii crack problems. *Engineering Fracture Mechanics*, 301:110016, 2024.

[20] E. C. Aifantis. The role of gradient in the mechanics of materials. *Journal of Elasticity*, 72(3):177–200, 2003.

[21] David J. Steigmann. The mechanics of second-gradient materials. *Journal of Elasticity*, 72(1):1–12, 2002.

[22] P. Germain. The mechanics of materials with second-order gradients. *Journal of the Mechanics and Physics of Solids*, 21(5):489–509, 1973.

[23] G. Rosi, I. Giorgio, and V. A. Eremeyev. Propagation of linear compression waves through plane interfacial layers and mass adsorption in second gradient fluids. *ZAMM – Journal of Applied Mathematics and Mechanics*, 2013.

[24] A. Madeo, I. Djeran-Maigre, G. Rosi, and C. Silvani. The effect of fluid streams in porous media on acoustic compression wave propagation, transmission, and reflection. *Continuum Mechanics and Thermodynamics*, 25(2):173–196, 2013.

[25] Victor A. Eremeyev and Holm Altenbach. Wave propagation in elastic solids with surface elasticity. *ZAMM – Zeitschrift für Angewandte Mathematik und Mechanik*, 92(6):426–434, 2012.

[26] Victor A. Eremeyev and Leonid P. Lebedev. Surface effects and wave propagation in microstructured elastic materials. *Mathematical Methods in the Applied Sciences*, 37(17):2710–2723, 2014.

[27] G. Rosi, V.-H. Nguyen, and S. Naili. Numerical investigations of ultrasound wave propagating in long bones using a poroelastic model. *Mathematics and Mechanics of Solids*, 21(1):119–133, 2015.

[28] Giuseppe Rosi, Ilaria Scala, Vu-Hieu Nguyen, and Salah Naili. Wave propagation in strain gradient poroelastic medium with microinertia: closed-form and finite element solutions. *Zeitschrift für angewandte Mathematik und Physik*, 68(3):58, 2017.

[29] Anna Castellano, Pilade Foti, Aguinaldo Fraddosio, Salvatore Marzano, and Mario Daniele Piccioni. Mechanical characterization of cfrp composites by ultrasonic immersion tests: experimental and numerical approaches. *Composites Part B: Engineering*, 66:299–310, 2014.

[30] Anna Castellano, Pilade Foti, Aguinaldo Fraddosio, Salvatore Marzano, and Mario Daniele Piccioni. Evaluation of damage anisotropy induced in gfrp composite materials by an innovative ultrasonic experimental approach. *Composite Structures*, 180:814–823, 2017.

[31] Aguinaldo Fraddosio, Anna Castellano, Pilade Foti, Salvatore Marzano, and Mario Daniele Piccioni. Linear and nonlinear ultrasonic techniques for monitoring stress-induced damages in concrete. *Materials*, 14(21):6562, 2021.

[32] E. Turco, E. Barchiesi, and F. dellâIsola. In-plane dynamic buckling of duoskelion beam-like structures: discrete modeling and numerical results. *Mathematics and Mechanics of Solids*, 27(7):1164–1185, 2022.

[33] M. Laudato, L. Manzari, E. Barchiesi, F. Di Cosmo, and P. Göransson. First experimental observation of the dynamical behavior of a pantographic metamaterial. *Mechanics Research Communications*, 94:125–127, 2018.

[34] Annamaria Pau and Dimitra Achillopoulou. Interaction of shear and rayleigh–lamb waves with notches and voids in plate waveguides. *Materials*, 10(7):1–14, 2017.

[35] D. Bucur. *Non-Destructive Testing of Materials by Ultrasonic Waves*. Springer, 2010.

[36] Annamaria Pau, Davide Capecchi, and Fabrizio Vestroni. Reciprocity principle for scattered fields from discontinuities in waveguides. *Ultrasonics*, 55:85–91, 2015.

[37] I. Giorgio, A. Della Corte, and F. Dell'Isola. Dynamics of 1d nonlinear pantographic continua. *Nonlinear Dynamics*, 88(1):21–31, 2017.

[38] B. Yang, M. Bacciocchi, N. Fantuzzi, R. Luciano, and F. Fabbrocino. Computational simulation and acoustic analysis of two-dimensional nano-waveguides considering second strain gradient effects. *Computers & Structures*, 296:107299, 2024.

[39] B. Yang, N. Fantuzzi, M. Bacciocchi, F. Fabbrocino, and M. Mousavi. Nonlinear wave propagation in graphene incorporating second strain gradient theory. *Thin-Walled Structures*, 198:111713, 2024.

[40] M. Laudato and E. Barchiesi. Non-linear dynamics of pantographic fabrics: Modelling and numerical study. In *Wave Dynamics, Mechanics and Physics of Microstructured Metamaterials*, pages 241–254. 2019.

[41] David Lurie. Viscoelastic effects in second-gradient materials: A theoretical framework. *Journal of Mechanics and Physics of Solids*, 102:37–50, 2017.

[42] Anil Misra. Longitudinal and transverse elastic waves in one-dimensional granular media. *International Journal of Solids and Structures*, 167:92–102, 2019.

[43] N. Nejadsadeghi and A. Misra. Role of higher-order inertia in modulating elastic wave dispersion in materials with granular microstructure. *International Journal of Mechanical Sciences*, 185:105867, 2020.

[44] Arkadi Berezovski, Ivan Giorgio, and Alessandro Della Corte. Interfaces in micromorphic materials: wave transmission and reflection with numerical simulations. *Mathematics and Mechanics of Solids*, 21(1):37–51, 2016.

[45] E. F. Grekova, A. V. Porubov, and F. Dell'Isola. Reduced linear constrained elastic and viscoelastic homogeneous cosserat media as acoustic metamaterials. *Symmetry*, 12(4):521, 2020.

[46] L. Placidi, G. Rosi, I. Giorgio, and A. Madeo. Reflection and transmission of plane waves at surfaces carrying material properties and embedded in second-gradient materials. *Mathematics and Mechanics of Solids*, 19(5):555–578, 2014.

[47] F. Fabbrocino and G. Carpentieri. Three-dimensional modeling of the wave dynamics of tensegrity lattices. *Composite Structures*, 173:9–16, 2017.

[48] J. Jafferis. Non-local effects and attenuation in wave propagation. *Journal of Applied Physics*, 89:283–299, 2015.

[49] V. K. Varadan, V. V. Varadan, and Y. Ma. Frequency-dependent elastic properties of rubberlike materials with a random distribution of voids. *Journal of the Acoustical Society of America*, 76(1):296–300, 1984.

[50] Max Gattin, Nicolas Bochud, Giuseppe Rosi, Philip A. Cotterill, William J. Parnell, and Salah Naili. Reflection and transmission of elastic waves from an immersed willis slab at oblique incidence. *International Journal of Solids and Structures*, 318:113394, 2025.

[51] Giuseppe Rosi, Vu-Hieu Nguyen, and Salah Naili. Reflection of acoustic wave at the interface of a fluid-loaded dipolar gradient elastic half-space. *Mechanics Research Communications*, 56:98–103, 2014.

[52] Giuseppe Rosi, Vu-Hieu Nguyen, and Salah Naili. Surface waves at the interface between an inviscid fluid and a dipolar gradient solid. *Wave Motion*, 53:51–65, 2015.

[53] Abo-el-nour Abd-alla, Ivan Giorgio, Luca Galantucci, Abdelmonam M. Hamdan, and Dionisio Del Vescovo. Wave reflection at a free interface in an anisotropic pyroelectric medium with nonclassical thermoelasticity. *Continuum Mechanics and Thermodynamics*, 28(1):67–84, 2016.

[54] Victor A. Eremeyev. Anti-plane surface waves in solids with surface structure. *Mechanics Research Communications*, 76:24–29, 2016.

[55] Victor A. Eremeyev and Sofia G. Mogilevskaya. Surface wave phenomena in elastic solids with gurtin–murdoch surface interfaces. *International Journal of Solids and Structures*, 132–133:20–31, 2018.

[56] Victor A. Eremeyev and Wojciech Pietraszkiewicz. Natural oscillations and wave processes in carbon nanotube arrays. *Physics Letters A*, 374(28):2851–2855, 2010.

[57] Victor A. Eremeyev. Acceleration waves in micropolar elastic media. *Journal of Applied Mathematics and Mechanics*, 69(1):15–24, 2005.

[58] Victor A. Eremeyev and Konstantin Naumenko. Wave dispersion relations in peridynamics and nonlocal elastic bars. *International Journal of Engineering Science*, 195:104579, 2025.

[59] Victor A. Eremeyev and Giuseppe Rosi. On rayleigh waves in elastic materials with surface stresses. *International Journal of Engineering Science*, 150:103261, 2020.

[60] Bijaya L. Sharma and Victor A. Eremeyev. Wave transmission across interfaces in lattice structures with surface effects. *Wave Motion*, 91:102–115, 2019.

[61] Bo Yang, Michele Bacciocchi, Nicholas Fantuzzi, Raimondo Luciano, and Francesco Fabbrocino. Wave propagation in periodic nano structures through second strain gradient elasticity. *International Journal of Mechanical Sciences*, 260:108639, 2023.

[62] Bo Yang, Nicholas Fantuzzi, Michele Bacciocchi, Francesco Fabbrocino, and Mahmoud Mousavi. Nonlinear wave propagation in graphene incorporating second strain gradient theory. *Thin-Walled Structures*, 198:111713, 2024.

[63] Raffaele Barretta, Annalisa Iuorio, Raimondo Luciano, and Marzia Sara Vaccaro. On wave propagation in nanobeams. *International Journal of Engineering Science*, 196:104014, 2024.

[64] Raffaele Barretta, Annalisa Iuorio, Raimondo Luciano, and Marzia Sara Vaccaro. Wave solutions in nonlocal integral beams. *Continuum Mechanics and Thermodynamics*, 36(6):1607–1627, 2024.

[65] Roberto Fedele and Raimondo Luciano. A recursive formula to compute lagrangian actions corresponding to an eulerian edge force in elastic materials with a sufficiently high grade. *Mathematics and Mechanics of Complex Systems*, 12(4):389–410, 2024.

[66] Roberto Fedele and David J. Steigmann. Lagrangian and eulerian formulations of second-grade elasticity via convected coordinates. *Mathematics and Mechanics of Complex Systems*, 13(3):377–389, 2025.

[67] G. Mancusi, F. Fabbrocino, L. Feo, and F. Fraternali. Size effect and dynamic properties of 2d lattice materials. *Composites Part B: Engineering*, 112:235–242, 2017.

[68] D. J. Steigmann and E. C. Aifantis. The mechanics of micromorphic continua: Theories and applications. *Mathematics and Mechanics of Solids*, 15(4):375–393, 2010.

[69] Anil Misra and Poria Poorsolhjouy. Granular micromechanics based micromorphic model predicts frequency band gaps. *Continuum Mechanics and Thermodynamics*, 28(1–2):245–268, 2015.

[70] Mahmoud Nejadsadeghi and Anil Misra. Role of higher-order inertia in modulating elastic wave dispersion in materials with granular microstructure. *Journal of the Mechanics and Physics of Solids*, 136:103772, 2020.

[71] Nicola De Fazio, Luca Placidi, Andrea Tomassi, and Aguinaldo Fraddosio. Different mechanical models for the study of ultrasonic wave dispersion for mechanical characterization of construction materials. *International Journal of Solids and Structures*, 315:113352, 2025.

[72] Nicola De Fazio, Luca Placidi, Francesco Fabbrocino, and Raimondo Luciano. Analysis of ultrasonic wave dispersion in presence of attenuation and second-gradient contributions. *CivilEng*, 6(3):37, 2025.

[73] Annamaria Pau, Samuele Sternini, and Francesco Lanza Di Scalea. Ultrasonic guided wave imaging of plates containing defects and inclusions. In *IEEE International Ultrasonics Symposium (IUS)*, 2020.

[74] Luca Placidi, Anil Misra, Abdou Kandalaft, and Nurettin Yilmaz. Analytical results for a linear hardening elasto-plastic spring investigated via a hemivariational formulation. *Constructive Mathematical Analysis*, 7(Special Issue: AT&A):50–75, 2024.

[75] Roberto Fedele. Viscoelastic wave propagation in rods described through internal variable formulations. *Meccanica*, 49(8):1863–1874, 2014.

[76] M. Mazzotti, A. Marzani, I. Bartoli, and E. Viola. Guided waves dispersion analysis for prestressed viscoelastic waveguides by means of the safe method. *International Journal of Solids and Structures*, 49(18):2359–2372, 2012.

[77] Bilen Emek Abali and Ömer Savas. Experimental validation for viscous flow simulations in an eccentric cylindrical cavity. *SN Applied Sciences*, 2(9):1500, 2020.

[78] R. Fedele, G. Maier, and B. Miller. Identification of elastic stiffness and local stresses in concrete dams by in situ tests and neural networks. *Structure and Infrastructure Engineering*, 1(3):165–180, 2005.

[79] B. Cagri Sarar, M. Erden Yildizdag, Francesco Fabbrocino, and B. Emek Abali. A comparative analysis for different finite element types in strain-gradient elasticity simulations performed on firedrake and fenics. *Mathematics and Mechanics of Complex Systems*, 13(3):237–252, 2025.

[80] F. D'Annibale. Piezoelectric control of the hopf bifurcation of ziegler's column with nonlinear damping. *Nonlinear Dynamics*, 86:2179–2192, 2016.

[81] G. Migliaccio and F. DâAnnibale. On the role of different nonlinear damping forms in the dynamic behavior of the generalized beckâs column. *Nonlinear Dyn*, 112:13733–13750, 2024.

[82] John C. Butcher. Implicit runge–kutta processes. *Mathematics of Computation*, 18(85):50–64, 1964.

[83] Ernst Hairer. The numerical solution of differential–algebraic systems by implicit runge–kutta methods. *Numerische Mathematik*, 36:431–449, 1981.

[84] A. Ciallella, I. Giorgio, S. R. Eugster, N. L. Rizzi, and F. Dell'Isola. Generalized beam model for the analysis of wave propagation with a symmetric pattern of deformation in planar pantographic sheets. *Wave Motion*, 113:102986, 2022.

[85] Francesco dell'Isola and Luca Placidi. Variational principles are a powerful tool also for formulating field theories, 2013. Technical report / institutional publication.

[86] L. Placidi, F. Di Girolamo, and R. Fedele. Variational study of a maxwell–rayleigh-type finite length model for the preliminary design of a tensegrity chain with a tunable band gap. *Mechanics Research Communications*, 136:104255, 2024.

[87] R. Hofmann. *Frequency dependent elastic and anelastic properties of clastic rocks*, volume 67. Colorado School of Mines, 2006.

[88] J. M. Carcione. *Wave Fields in Real Media: Wave Propagation in Anisotropic, Anelastic, Porous and Electromagnetic Media*. Elsevier, 2nd edition, 2007.

[89] Kang Lee, Victor Humphrey, Byoung-Nam Kim, and Suk Yoon. Frequency dependencies of phase velocity and attenuation coefficient in a water-saturated sandy sediment from 0.3 to 1.0 mhz. *The Journal of the Acoustical Society of America*, 121:2553–8, 06 2007.

[90] T.P. Philippidis and D. Aggelis. Experimental study of wave dispersion and attenuation in concrete. *Ultrasonics*, 43:584–95, 07 2005.

[91] Léon Brillouin. *Wave Propagation and Group Velocity*. Academic Press, New York, 1960.

[92] Peter J. Huber and Elvezio M. Ronchetti. *Robust Statistics*. Wiley, 2nd edition, 2009.

[93] Frank R. Hampel, Elvezio M. Ronchetti, Peter J. Rousseeuw, and Werner A. Stahel. *Robust Statistics: The Approach Based on Influence Functions*. Wiley, 1986.

[94] Steven M. Kay. *Fundamentals of Statistical Signal Processing: Estimation Theory*. Prentice Hall, 1993.

[95] Peter J. Rousseeuw and Annick M. Leroy. *Robust Regression and Outlier Detection*. Wiley, 1993.

[96] Rand R. Wilcox. *Introduction to Robust Estimation and Hypothesis Testing*. Academic Press, 4th edition, 2017.

[97] Athanasios Papoulis and S. Unnikrishna Pillai. *Probability, Random Variables, and Stochastic Processes*. McGraw–Hill, 4th edition, 2002.

[98] Robert C. Kirby et al. Irksome demo: Solving the mixed wave equation with explicit runge–kutta methods. `https://www.firedrakeproject.org/Irksome/demos/demo_RTwave_PEP.py.html`, 2020.

[99] Thomas J. R. Hughes. *The Finite Element Method: Linear Static and Dynamic Finite Element Analysis*. Dover Publications, Mineola, NY, 2000.

[100] Alfio Quarteroni, Riccardo Sacco, and Fausto Saleri. *Numerical Mathematics*. Springer, 2007.

[101] T. J. R. Hughes. *The Finite Element Method: Linear Static and Dynamic Finite Element Analysis*. Prentice-Hall, 1987.

[102] S. Marburg. Six boundary elements per wavelength: Is that enough? *Journal of Computational Acoustics, nr.01*, 10:25–51, 2002.

[103] F. Ihlenburg and I. Babuska. Finite element solution of the helmholtz equation with high wave number. part i: The h-version of the fem. *Computers Mathematics with Applications*, 30(9):9–37, 1995.

[104] G. Cohen. *Higher-Order Numerical Methods for Transient Wave Equations*. Scientific Computation. Springer, 2002.

[105] Florian Rathgeber, David A. Ham, Lawrence Mitchell, Michael Lange, Fabio Luporini, Andrew T. T. McRae, Gheorghe-Teodor Bercea, Graham R. Markall, and Paul H. J. Kelly. Firedrake: Automating the finite element method by composing abstractions. *ACM Transactions on Mathematical Software*, 43(3):24:1–24:27, 2016.

[106] Patrick E. Farrell, David A. Ham, Simon W. Funke, and Marie E. Rognes. Automated solution of time-dependent pdes using implicit runge–kutta methods. *SIAM Journal on Scientific Computing*, 42(2):C81–C104, 2020.

[107] Ernst Hairer and Gerhard Wanner. *Solving Ordinary Differential Equations II: Stiff and Differential-Algebraic Problems*. Springer, 1996.

[108] J. S. Popovics. Ultrasonic testing of concrete structures. *Materials Evaluation*, 56(9):1035–1042, 1998.

[109] Richard L. Weaver. Diffusion of ultrasound in polycrystals. *Journal of the Acoustical Society of America*, 88(2):1097–1103, 1990.

[110] Frank Ihlenburg. Finite element analysis of acoustic scattering. 1998.

[111] E. Turco, E. Barchiesi, and F. dellâIsola. A numerical investigation on impulse-induced nonlinear longitudinal waves in pantographic beams. *Mathematics and Mechanics of Solids*, 27(1):22–48, 2022.

[112] E. Barchiesi, M. Laudato, and F. Di Cosmo. Wave dispersion in non-linear pantographic beams. *Mechanics Research Communications*, 94:128–132, 2018.

[113] B. E. Abali, B. Vazic, and P. Newell. Influence of microstructure on size effect for metamaterials applied in composite structures. *Mechanics Research Communications*, 122:103877, 2022.

[114] B. E. Abali. Revealing the physical insight of a length-scale parameter in metamaterials by exploiting the variational formulation. *Continuum Mechanics and Thermodynamics*, 31(4):885–894, 2019.

[115] N. Challamel, Y. P. Zhang, C. M. Wang, G. Ruta, and F. Dell'Isola. Discrete and continuous models of linear elasticity: History and connections. *Continuum Mechanics and Thermodynamics*, 35(2):347–391, 2023.

[116] F. Fabbrocino and A. Amendola. Discrete-to-continuum approaches to the mechanics of pentamode bearings. *Composite Structures*, 167:219–226, 2017.